To the Graduate Council:

I am submitting herewith a dissertation written by Irakli Garishvili entitled "Open Heavy Flavor Measurement at Forward Angles in Cu+Cu collsions at $\sqrt{s_{NN}} = 200$ GeV". I have examined the final paper copy of this dissertation for form and content and recommend that it be accepted in partial fulfillment of the requirements for the degree of Doctor of Philosophy, with a major in Physics.

Kenneth F. Read, Major Professor

We have read this dissertation
and recommend its acceptance:

Soren P. Sorensen

Yuri Efremenko

Lawrence Townsend

Glenn Young

Accepted for the Council:

Carolyn R. Hodges
Vice Provost and Dean of the Graduate School

(Original signatures are on file with official student records)

Open Heavy Flavor Measurement at Forward Angles for Cu+Cu Collisions at Center of Mass *NN* Collision Energy 200 GeV

A Dissertation
Presented for the
Doctor of Philosophy
Degree
The University of Tennessee, Knoxville

Irakli Garishvili
December 2009

Dedicated to the memory of my Father,

Temuri Garishvili.

Acknowledgements

Without any doubt the years I've spent in Knoxville were the best years of my life, not only because I met my wife and got my Ph.D. here. I was extremely lucky to have been surrounded by many people who cared about me and taught me so much. Because of them I am a better scientist and a better person. I want to thank you all for everything.

First, I would like to thank my advisor Ken Read for all his help and direction during my Ph.D. I am very grateful to Ken for carefully correcting countless typos in my dissertation. From the beginning, when I saw him with the sign "Irakli" at Tyson McGee Airport, Soren Sorensen has always been there for me. As a department head, Soren is probably the busiest man around here, yet I have always felt his support in good or bad times. Words can not express how grateful I am to you, Soren. I would like to also thank Soren's wife, Diane, for always being so caring and kind to me and Maria.

More than five years I shared one office with my friend Donny Hornback. Although he continuously kicked my butt in tennis, he has been nothing but a great friend. I always knew who to go to when I needed most. He is the main reason I have been able to adapt so quickly to the new environment, so far away from home. Donny was also the architect of the "single muon matrix", the ETSM framework, which made this analysis possible. Thanks for everything you have done for me. I would also like to thank Dodie, Donny's wife, for being so king and friendly to me and my family.

I have been extremely lucky and honored to have worked with Vince Cianciolo at ORNL. He has been my true mentor and taught me so much. The busiest man alive, Vince, has been always available. It is no doubt that without his help and ideas I would not have graduated. Thank you so much Vince. I also wanted to say my special

thanks to Yuri Efremenko for teaching me so much about experimental physics. I definitely know a whole lot more about detectors, electronics, etc. Thanks also for serving on my committee. I would like to thank Professor Larry Townsend and Glenn Young for serving on my committee and for their extremely helpful suggestions and corrections. I also want to thank Glenn for his time and exciting discussions about the QGP. I am extremely grateful to Cheuk-Yin Wong spending so much time for answering my amateur questions every time I stopped by his office at ORNL.

A special thanks goes to Vasily Dzhordzhadze for introducing me to the physics of QGP and trusting me to succeed. Obviously if not for Vasily I would not even have come to Knoxville. I have learned a lot from DongJo Kim and David Silvermyr. I am very grateful to you guys for exposing me to your countless software tricks and being so patient with me. I also would like to thank my PHENIX colleagues for their great ideas and support, especially, Yongil Kwon, Hugo Pereira and Mike Leitch.

I am grateful to the former and current members of our UT-ORNL group, Jason Newby, Andy Glenn, Josh Hamblen, Akitomo Enokizono and Dwayne John for their friendship and help. I am also very thankful to Christine Natrass for corrections and useful suggestions to my thesis. I also wanted to thank Christine in advance for generously offering to brew my thesis beer.

I have been privileged and lucky to meet and bond with so many great people from all around the world. I want to thank all my friends for all those great times and memories. I know it will be very hard to leave Knoxville. But you will always be in my heart.

I know I have the best family in the world. I would like to thank my mom, Tiniko, for her countless sacrifices and conditionless love. I want to thank my brother Archil and my grandmas, Lena and Rusiko, for their love and support. I am extremely grateful to my uncle, Sasha, who has been my role model as a physicist. But most

importantly, he has been like father to me, no matter how far he was.

Last, but not least, I want to thank my wife Maria for her love and care. This would have been impossible without her support.

Abstract

The main purpose of Relativistic Heavy Ion Collider (RHIC) program is to study the Quark-Gluon Plasma (QGP), a deconfined state of matter believed to be created in ultra-relativistic heavy ion collisions. Heavy quarks, expected to be produced during the earlier stages of heavy ion collisions, serve as an important probe of the QGP.

The following dissertation presents measurements of single muons resulting from the semileptonic decay of heavy flavor quarks in the rapidity range of $1.4 < |\eta| < 1.9$ for Cu+Cu nuclei collisions at $\sqrt{s_{NN}} = 200$ GeV measured by the PHENIX experiment. Single muon spectra were measured for three different centrality classes (0 - 20 % , 20 - 40 %, 40 - 94 %) within the p_T range of 1.0 - 4.0 GeV/c.

To calculate single muon spectra, a full background estimate was statistically subtracted from inclusive spectra of muon candidate tracks reconstructed in the PHENIX muon arms. The background was predicted and estimated with a "Hadron Cocktail", a full-scale data-driven Monte Carlo simulation. The hadron cocktail approach was originally developed and implemented to measure single muon production for Run-5 p+p collisions. First, the relevant light hadrons are generated with a "realistic" input (ratios of different particle species and p_T spectra). The generated tracks are then propagated through the PHENIX detector geometry using GEANT. At the last step, introduced and implemented specifically for this analysis, the simulated tracks were embedded into real events and finally reconstructed with the PHENIX muon arms reconstruction software. This was done to realistically reproduce detector performance due to effects caused by colliding heavy ions. The hadron cocktail method provides a much better alternative to the previously attempted purely data-driven peacemeal approaches which suffer from very large systematic uncertainties.

Finally, using baseline single muon measurements for p+p collisions, nuclear modification factors for all of the above specified centralities have been measured. These are the first measurements of single muon spectra and nuclear modification factors at forward angles for any two heavy colliding ion systems.

Contents

List of Tables

List of Figures

Chapter 1

Introduction

It may take another 13.5 billion years to understand what the universe looked like during the "Big Bang", or why did it happen at all. Maybe, we will never find the answer. However, by now, we may have learned enough to understand the matter that the universe consisted of about 10^{-5} seconds after the Big Bang. Moreover, many believe, that this very matter, called "Quark-gluon plasma", has already been reproduced in laboratory conditions, specifically, in the ultrarelativistic heavy ion collisions at the Relativistic Heavy Ion Collider (RHIC). This work is one of many efforts towards understanding this matter.

1.1 Quark Gluon Plasma

The idea that matter is made of some elementary constituents is old. In the 5th century B.C., Democritus, a Greek philosopher, suggested that matter consists of unchangeable and indivisible entities, *atoms* (the Greek word for "uncuttable"), that constantly move around. According to him these atoms were made from the same type of material but had different shapes and sizes. Remarkably, Democritus' ideas

turned out to be extremely close to the present theoretical understanding of matter, confirmed by many experimental findings.

Indeed, matter consists of two basic types of fundamental elementary particles called *quarks* and *leptons*. There are four fundamental forces, *gravity*, the *weak force*, the *electromagnetic force* and the *strong force*, carried by the "force carrier" particles, that are responsible for the interactions between these elementary particles. The theory that describes these elementary particles and the fundamental interactions between them is called Standard Model.

According to the Standard Model, quarks, as well as leptons, come in six different flavors. Moreover, each of these elementary particles has a "mirror image" counterpart, called an anti-particle. Unlike leptons, quarks can also participate in the strong interaction and cannot exist as independent particles. Instead, in specific combinations with the other quarks, they are "confined" inside the particles called *hadrons*. There are only two types of hadrons, *baryons* and *mesons*. The baryons (p, n, Λ, ...) consist of 3 quarks or 3 anti-quarks. Whereas, mesons (π, K, ρ, ...) are the combinations of a quark and an anti-quark*.

Quantum Chromodynamics (QCD) is the theory within the Standard Model that describes the strong interactions between quarks and gluons, often referred as *partons*. According to QCD, quarks carry *color charge* and interact with each other via exchange of strong force carriers, *gluons*. Gluons, also carry color charge, and therefore can also interact with each other.

The effective strength of the interactions between the partons is quantified by the strong running coupling constant, α_s. To be precise, α_s is not exactly a constant as it changes depending on the momentum transferred in the interaction, μ, and can

*The proton is thought to be stable, as far as has been measured. All other free hadrons are known to decay eventually.

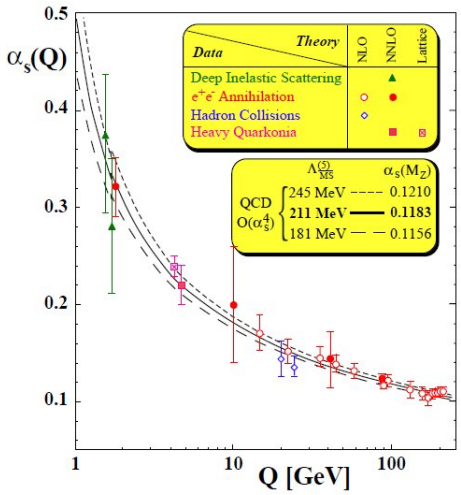

Figure 1.1: Theoretical and experimental comparison of the running coupling constant of the strong interaction as a function of Q [4]

be expressed as follows [1]:

$$\alpha_s(\mu) = \frac{2\pi}{b_0 log(\mu/\Lambda_{QCD})} \tag{1.1}$$

where $b_0 = 11 - \frac{2}{3}n_f$, with n_f being number of approximately massless quarks, and with Λ_{QCD} constant defining an arbitrary momentum scale at which α_s becomes "strong" and estimated experimentally to be about 200 MeV. Equation 1.1 expresses the principle of *asymptotic freedom* postulated by Gross, Politzer and Wilczek [2],[3] in 1973, which later on has been confirmed by many experimental results as illustrated in Figure 1.1. According to this principle, for the energy scales below Λ_{QCD}, roughly corresponding to the typical size of hadrons[†], the effective coupling between the interacting quarks becomes infinitely strong, exhibiting *confinement* phenomena. Conversely, as the energy scale gets larger, the interaction between quarks and gluons becomes weaker. In the extreme energy limit ($Q >> \Lambda_{QCD}$) this will lead to the complete deconfinement of partons from hadrons.

In his 1980 review Shuryak [5] argued that if energy density exceeds a critical value

[†] $r \sim 1/\Lambda_{QCD} \sim 1$ fm.

of $\epsilon_c \sim 1$ GeV/fm^3, the normal nuclear matter will make a phase transition to the new state of matter, where quarks and gluons will no longer be bound inside the hadrons, becoming the effective degrees of freedom of this matter. Because of the existing analogy to atomic physics he called it QCD plasma or Quark-Gluon Plasma (QGP).

Indeed the early universe is thought to have existed in the QGP-like state of very high temperature and zero baryon density. Deconfined matter can also exist in the lower energy or temperature limit, but in an environement with a very high baryon density like in neutron stars, as illustrated in Figure 1.2.

Independently, lattice QCD calculations shown in Figure 1.3 confirmed that the number of the degrees of freedom of the QCD matter at the low baryon density regime increases sharply near a critical temperature of $T_c \sim 170$ MeV indicating some type of phase transition. The order of this transition is not known.

1.2 Relativistic heavy ion collisions

As was discussed in the previous section, in order for the QGP to be created, predictions indicate that it is necessary to produce a system with energy density of 1 GeV/fm^3 or above. In the laboratory this can be achieved by colliding heavy nuclei at the ultrarelativistic center of mass bombarding energies of at least 10-100 times the rest mass of the nuclei, where unlike in p+p collisions, multiple subsequently occuring inelastic binary nucleon-nucleon collisions will ensure production of the matter large enough in extent to enable qualitative experimental exploration of its thermodynamical and other key properties.

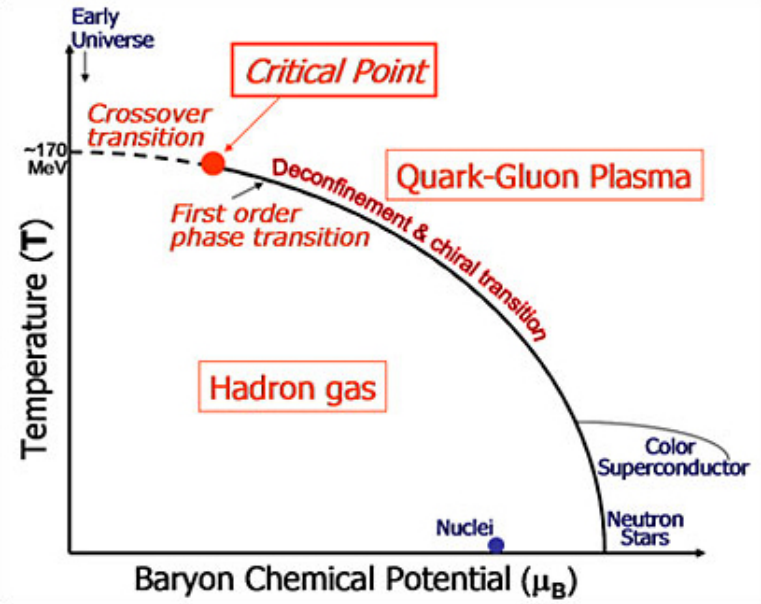

Figure 1.2: Phase space diagram of the QCD matter

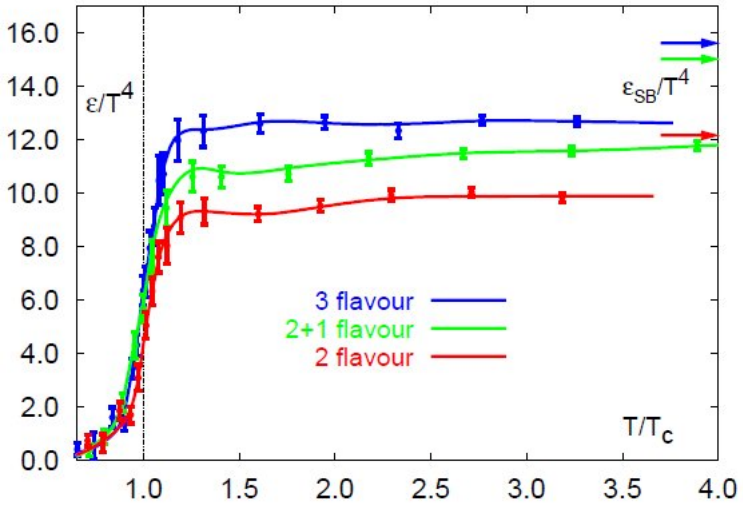

Figure 1.3: Lattice QCD calculations of ϵ/T^4 as a function of the temperature. The arrows indicate Stefan-Boltzmann limit.

1.2.1 Space-time picture of the collisions

According to the current understanding of the heavy-ion collision dynamics the system of the colliding heavy ions goes through a sequence of several different stages as illustrated in Figure 1.4. At time $t = 0$ the initial contact of two incoming Lorentz contracted (in the CM system) nuclei occurs. Since the maximum possible crossing time between these nuclei, $\tau_{cross} = 2\mathrm{R}/\gamma\mathrm{c} \sim 0.1$ fm/c, is much smaller than a typical timescale of the strong interaction, $\tau_{cross} \sim 1/\Lambda_{QCD} \sim 1.0$ fm/c, they pass through each other very fast, subsequently leaving behind matter with a very large energy density. At the *formation time* $\tau_{form} \leq 1$ fm/c the initial production of partons occurs. It is assumed that within another 1 fm/c at $t = \tau_{therm}$ the interactions between these partons will bring the system to local thermal equilibrum. The energy density continues decreasing as the system further expands. Once it drops below the QCD confinement threshold the system hadronizes. At this point the system can be viewed as a gas of hadrons interacting with each other. Finally, after the system cools down to the "freeze-out" temperature, hadrons cease interacting with each other and stream out into the detectors.

A key question here is whether the energy density at τ_{form} was sufficient to create the QGP. To answer it one needs to use the experimentally measured particle multiplicity per collision to extrapolate backwards to estimate the energy and volume of the initial collision region. The experimental challenge here is that, a typical Au+Au collision at RHIC produces thousands of hadrons, mostly pions. However, only a fraction of tracks, depending on their kinematics, can be reconstructed[‡].

The energy density can be estimated from Brjorken's formula [6]:

$$\epsilon_0 = \frac{\langle m_T \rangle}{\tau_0 \; A_T} \left. \frac{dN}{dy} \right|_{z=0} \tag{1.2}$$

[‡]For the detailed discussion on the kinematic variables and produced particles yield the reader is referred to Appendix A.

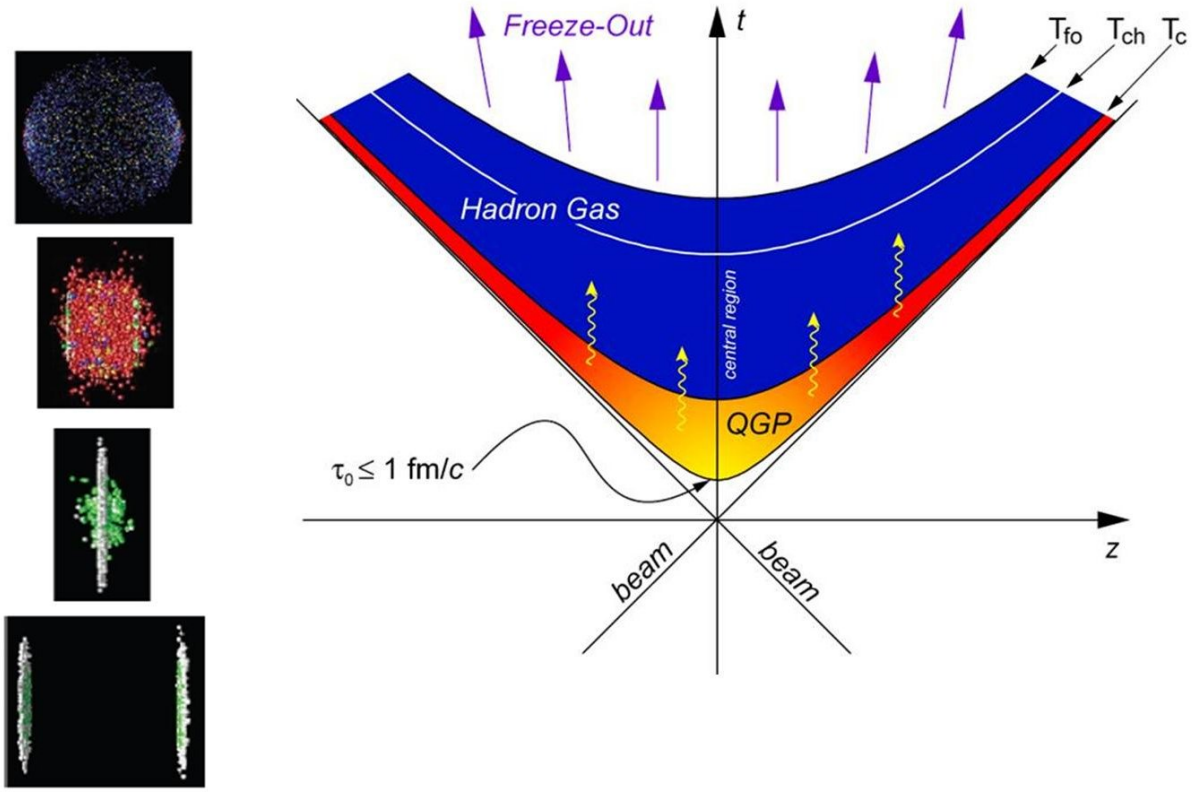

Figure 1.4: The space-time diagram of a heavy ion collision (right), with the corresponding visualization of the stages of the collision dynamics (left).

where $\langle m_T \rangle$ defines the average transverse mass per produced particle, which can be measured. A_T and $\frac{dN}{dy}$ represent the effective transverse overlap area of the colliding ions and particle multiplicity, respectively.

Based on Bjorken's formula and the existing experimental data, it was estimated that the peak energy density of the bulk matter in head-on Au+Au collisions at RHIC reaches at least 15 GeV/fm^3 [7]. Furthermore, after comparing hydrodynamical model predictions to RHIC data, it was concluded that the bulk matter thermalizes in a very short timescale of 0.6-1.0 fm/c, implying that the energy density of thermalized bulk matter is in the range beween 5.7 and 9.5 GeV/fm^3 [7], which is a few times above the predicted threshold value for creating QGP.

1.2.2 Centrality

For a specific CM energy and type of colliding ion species, heavy ion collisions can be qualitatively different (in terms of initially achieved peak energy densties and subsequently produced hadron multiplicities) from one another depending on the initial overlap of incoming nuclei or the impact parameter, b, illustrated in Figure 1.5. The impact parameter essentially determines the number of participant or "wounded" nucleons per heavy ion collision, defined as N_{part}.

On average each participant goes through more than one collision with the other participants. Therefore, the number of the subsequent inelastic binary nucleon-nucleon collisions, N_{coll}, is always larger than the N_{part} number for heavy ion collisions. Based on a specific set of the b, N_{coll} and N_{part} variables, the heavy ion collision events are usually categorized via the collision *centrality*, with $b \sim 0$ (the largest possible N_{coll} and N_{part}) and $b \sim 2$R (the smallest possible N_{coll} and N_{part}) corresponding to most central and most peripheral collisions, respectively.

The centrality cannot be directly measured as the collisions happen. Instead, exper-

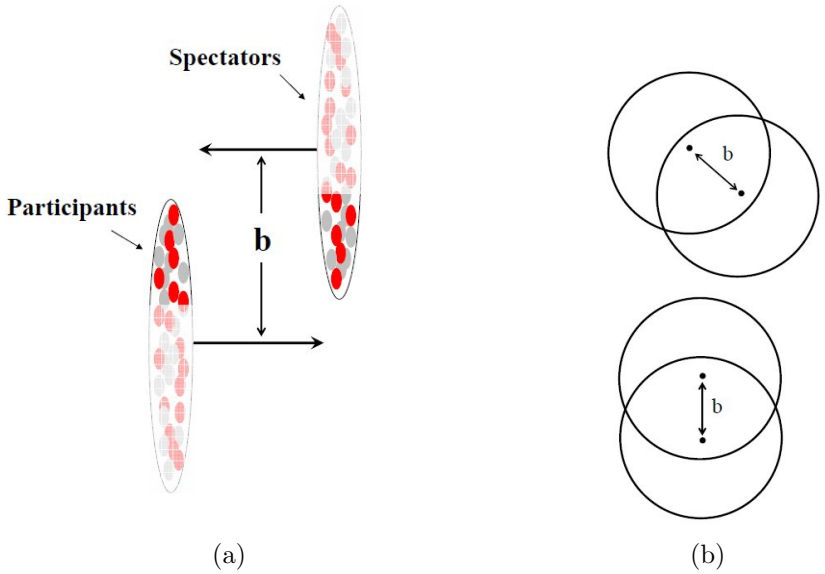

Figure 1.5: (a) A pictorial representation of a collision of the "Lorentz contracted" (along z-axis) heavy ions.(b) An illustration of the transverse overlap between the colliding nuclei looking along the collision axis.

imentally measured particle multiplicities are combined with a Glauber model based Monte Carlo simulation of heavy ion collisions to estimate the b, N_{coll} and N_{part} variables "(Appendix B)".

1.3 QGP signatures and observables at RHIC

One of the main challenges of the heavy ion physics program is that experimentally the QGP cannot be directly accessed, since it is a partonic state of matter with a very short lifetime. Therefore, identifying and measuring the hadron observables which would not only have a clear theoretical interpretation, but also provide critical information about the properties of the created matter, is of great importance.

Indeed, since the very first collisions in 2000, RHIC has produced many measurements that are consistent with the creation of a deconfined state of matter. Only the

observables relevant to the heavy flavor physics will be discussed here.

1.3.1 Jet quenching

Jet production is considered to be one of the best theoretical and experimental tools for studying the properties of the QGP matter. Jets are initially produced in the hard scatterings ($Q > 2$ GeV) of incoming partons which usually results in the subsequent creation of pairs of outgoing high p_T partons[§]. Each of these high p_T partons later fragment into a leading energetic hadron and large number of other hadrons consentrated in the nearby cone, providing a very clear experimental pattern as shown in Figure 1.6(a).

Because of the associated large energy scale, the initial production and later hadronization of jets can be precisely theoretically calculated within the perturbative QCD (pQCD) framework.

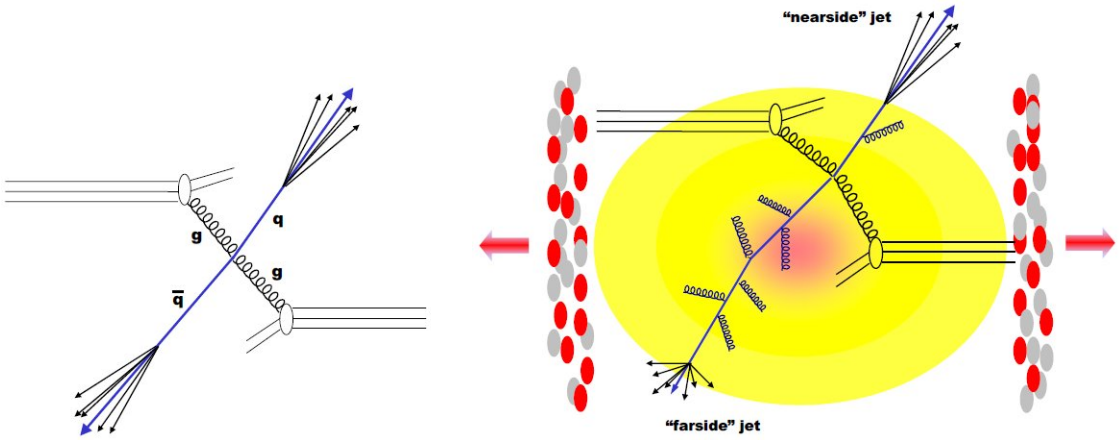

(a) (b)

Figure 1.6: (a) A production of a pair of jets in a nucleon-nucleon collision. (b) An illustration of the associated pair of jets traveling through the dense deconfined medium created as a result of the collision of two heavy ions.

[§]Also a common way to produce a jet is an elastic collision of 2 partons that leads to a significant re-orientation fo their relative velocity.

Hard scatterings are essentially point-like processes occuring in a very short time scale ($\tau \sim 1/p_T \sim 0.1 fm/c$). Therefore, the initial production cross section of the high p_T jet partons in A+A collisions is expected to scale with the production cross section measured in p+p collisions. However, unlike in p+p collisions, these high p_T partons encounter the created deconfined medium, and subsequently will suffer energy loss due to medium-induced gluon bremstrahlung and the collisions with abundant in-medium partons. Consequently, as illustrated in Figure 1.6(b) the jets produced near the medium surface in the out-of-medium direction , "nearside" jets, will suffer much smaller energy loss, as opposed to the "farside" jets that have to travel through the most of the medium.

The medium effects on the jet production in heavy ion collisions can be quantified with the *nuclear modification factor* defined by the following:

$$R_{AA} = \frac{dN_{AA}}{\langle N_{coll} \rangle dN_{p+p}} \tag{1.3}$$

where dN_{AA} and dN_{p+p} are invariant yields of measured hadron production from the jet fragmentation in A+A collisions and p+p collisions, respectively. $R_{AA} \neq 1$ would be indicative either of the suppression ($R_{AA} < 1$) or the enhancement ($R_{AA} > 1$) of the observed yield in A+A collisions with respect to naively scaled expectations from p+p collisions.

PHENIX measurements show a large suppression (by a factor of 4-5) of high-p_T hadron production in the most central (0-10%) Au+Au collisions as compared to $p + p$ and $d + Au$ data, as shown in Figure 1.7. Separately, the measurement of the correlated dijets by the STAR experiment, shown in Figure 1.8, reveal that in the central Au+Au collisions the high p_T component of the signal from away-side jets is completely vanished, in contrast to what has been observed either in p+p or d+Au collisions.

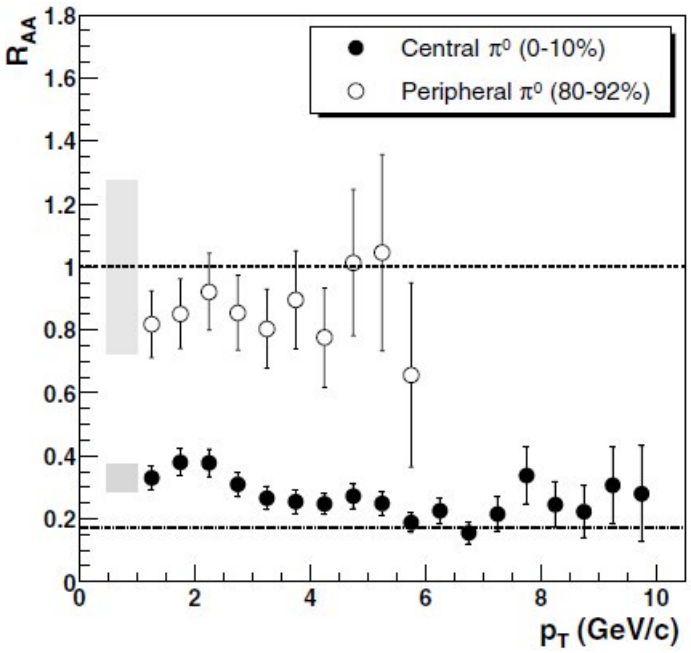

Figure 1.7: The PHENIX measurement of the nuclear modification factor for π^0 production in the most central and peripheral Au+Au collisions [8].

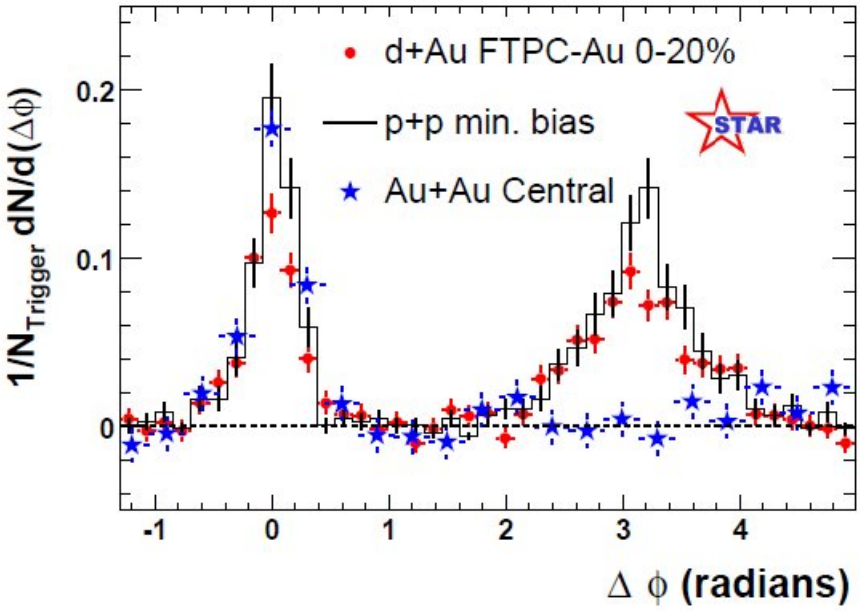

Figure 1.8: The comparison of the correlated two-particle azimuthal distributions observed in most central Au+Au collisions to those seen in p+p and d+Au collisions, measured by the STAR experiment [9].

These "smoking gun" type results from the two experiments are clearly suggestive of rather remarkable in-medium effects that can be caused only by the presence of a very dense and strongly interacting medium.

1.3.2 Elliptic flow

Another striking feature observed in heavy ion collisions, totally absent in p+p collisions, is the spatial anisotropy of the produced multiplicities of the various hadron species. This effect was most profound in non-central collisions ($b \neq 0$). In this case, due to the specific overlap, the incoming nuclei initially creates matter with an "almond"-like asymmetric shape, as illustrated in Figure 1.9(a). Now, if the QGP is a gas-like state of matter of weakly interacting partons, the created spatial asymmetry should quickly disappear due to the rapid thermal expansion, resulting in a nearly spherically symmetric expansion. Conversely, if the partons inside the medium experience much stronger interactions between each other than was originally presumed, the multiple rescatterings occuring in the system will develop pressure gradients directed outwards, with the largest ones along the x-axis in the reaction plane, Φ_R, which is the smallest of the almond axes. Consequently, as illustrated in Figure 1.9(b) the spatial anisotropy of the bulk turns into a momentum anisotropy referred to as "elliptic flow" of the partons. Finally, once the system hadronizes, particles are emitted asymmetrically in azimuth.

The magnitude of the elliptic flow is quantified by the second Fourier coefficient, v_2, of the azimuthal expansion of single semi-inclusive hadron spectra with respect to the reaction plane:

$$E\frac{d^3N}{d^3p} = \frac{1}{2\pi p_T}\frac{d^2N}{dp_T dy}\left(1 + 2\sum_{n=1}^{\infty} v_n cos[n(\phi - \Phi_R)]\right). \tag{1.4}$$

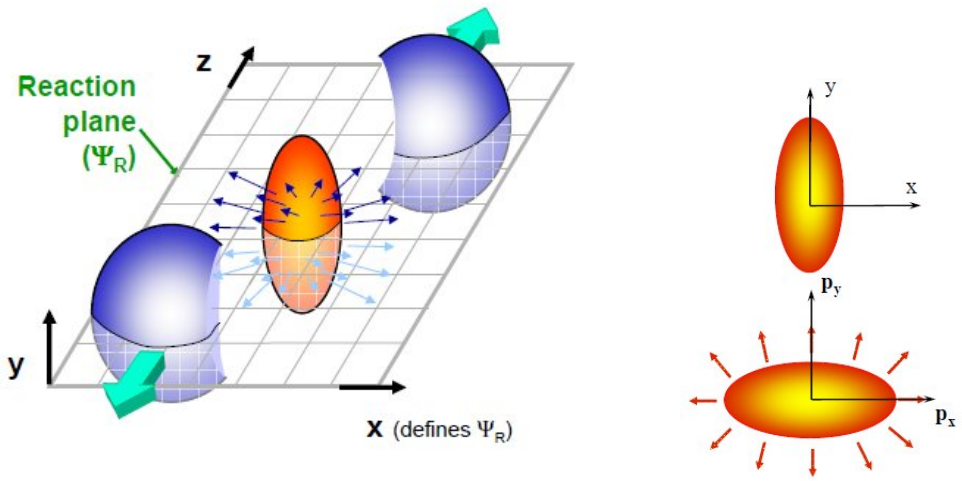

(a) (b)

Figure 1.9: (a) Illustration of the "almond" shaped matter created as the result of a non-central collision of heavy nuclei moving along the reaction plane and z-axis. (b)

Shown in Figure 1.10 is the elliptic flow of the various hadron species measured by the PHENIX and STAR experiments compared to the corresponding hydrodynamical model predictions. A substantial v_2 is measured over a wide p_T range, indicating the strong collectivity of the bulk matter in the initial phases of the collisions. It is important to note that in the kinematic range of $p_T \leq 2$ GeV, where the vast majority of the bulk particles are produced, the data is in good agreement with the hydrodynamical model prediction, which uses very short thermalization times (≤ 0.6 fm/c) as an input parameter, and assumes a strongly interacting liquid of a small viscosity to entropy ratio.

Figure 1.11 shows the same data, but this time the measured elliptic flow for each hadron species is scaled with the number of the corresponding constituent quarks, v_2/n. Quite remarkably, v_2/n for all hadron species follow identical universal scaling. This strongly indicates that it is quarks (partons) during the early times of the collisions, not hadrons, that participate in the collective motion caused by strong

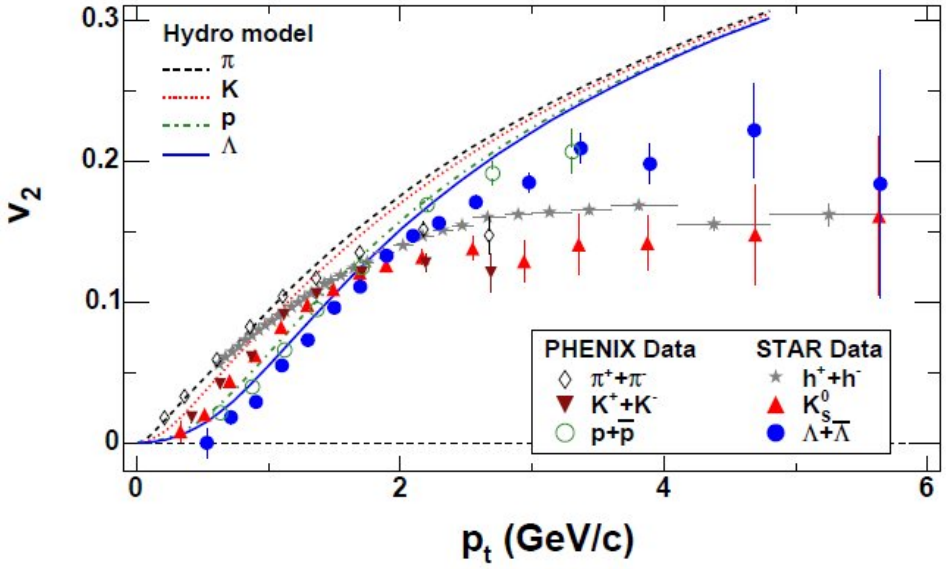

Figure 1.10: A comparison of the PHENIX and STAR measurements of the v_2 variable for the different hadron species [10][11] to the hydro model predictions from [12].

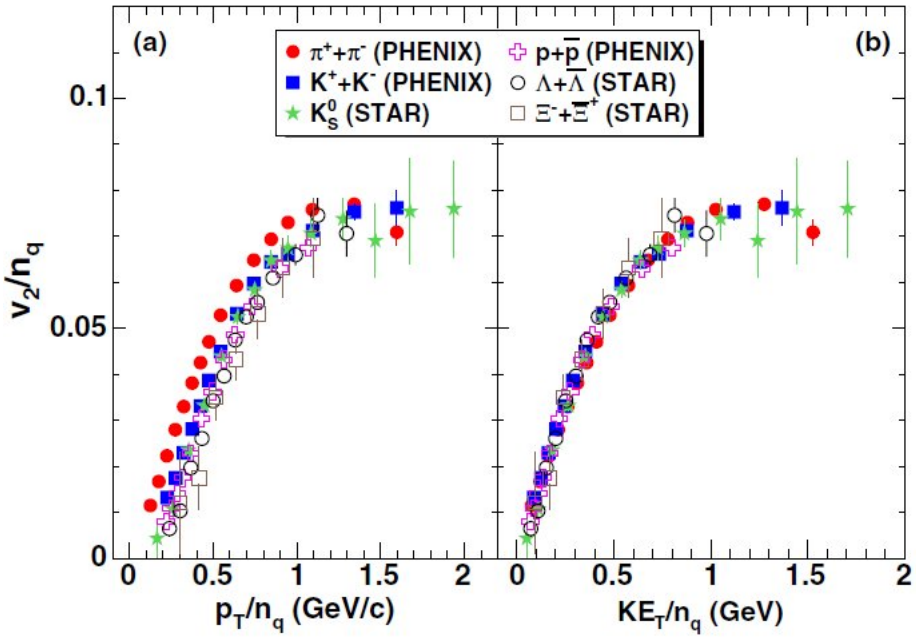

Figure 1.11: A compilation from [13] of the PHENIX and STAR results [14],[15] of v_2/n as a function of p_T (a), and kinetic energy (b) for various hadron species.

interactions.

These results were a huge surprise at the time. It turned out that the matter created in the Au+Au collisions at RHIC is consistent with a liquid-like strongly interacting bulk with very short thermalization times, quite different from the initially conjectured gas-like plasma. The data strongly supports the notion that the degrees of freedom of the created matter are of partonic origin, which would be a clear indication of deconfinement.

1.3.3 Charmonium suppression

Perhaps the most famous and the most controversial subject in the heavy ion physics, charmonium suppression has long been proposed as a direct evidence that the matter created in the heavy ion collisions is of a deconfined nature [16].

The J/ψ particle is the lightest and the most stable of the charmonium vector mesons, the bound states of the $c\bar{c}$ quark pairs. A $c\bar{c}$ quark pair is initially produced as a result of hard partonic collisions and subsequently hadronizes into a J/ψ particle. In normal QCD matter, the strong (confining) potential between the colored $c\bar{c}$ quarks at large distances behaves as

$$V_0(r) \sim \sigma r, \tag{1.5}$$

with σ being the string tension [17]. Thus, an infinitely large energy would be required to break up the bond between the pair. However, if a system of $c\bar{c}$ quarks finds itself in a dense environment of deconfined partons, the strong potential between the $c\bar{c}$ quarks will be screened due to the presence of other color charges [18],

$$V_0(r) \sim \sigma r \left[\frac{1 - e^{-\mu r}}{\mu r}\right] \tag{1.6}$$

with μ being the inverse of a screening radius. This is analogous to the Debye

screening of the electromagnetic potential arrising in a plasma of electric charges. As a result, J/ψ production is expected to be suppressed in the deconfined environment.

Remarkably, this was exactly what was initially observed in the heavy ion collisions at the CERN SPS, as shown in Figure 1.12. The suppression was not observed in the peripheral collisions of light nuclei, which was interpeted by many as a proof that QGP was indeed produced in the ultrarelativistic heavy ion collisions at the SPS.

However, it turned out that the production of J/ψ particles is also suppressed in p+A type collisions. These collisions are not expected to produce hot and dense deconfined matter, which suggests that there are some "cold" nuclear matter effects (different from the suggested color screening) that are absolutely necessary to take into account. In particular, *gluon shadowing*, the depletion of small momentum (with respect to the momentum of nucleon) gluons inside nuclei [20]. Another possible effect is so called "Cronin Effect", the observed broadening of p_T [21], also seen for the production of different particle species [7].

Understanding charmonium production and the underlying mechanisms of its suppression in heavy ion collisions is one of the priorities of the heavy ion physics program at RHIC.

These and other measurements (not discussed here) observed at RHIC are strongly supportive of the hypothesis that the matter created in the heavy ion collision is of deconfined nature. However, these results were indeed unexpected based on the early theoretical predictions for the QGP as a gas-like state of weakly interacting partons. Instead the data strongly suggest that the matter created in the early stages of heavy ion collisions behaves as a liquid-like, very dense and strongly interacting medium of color charges, often referred to as "strongly-coupled QGP" (sQGP).

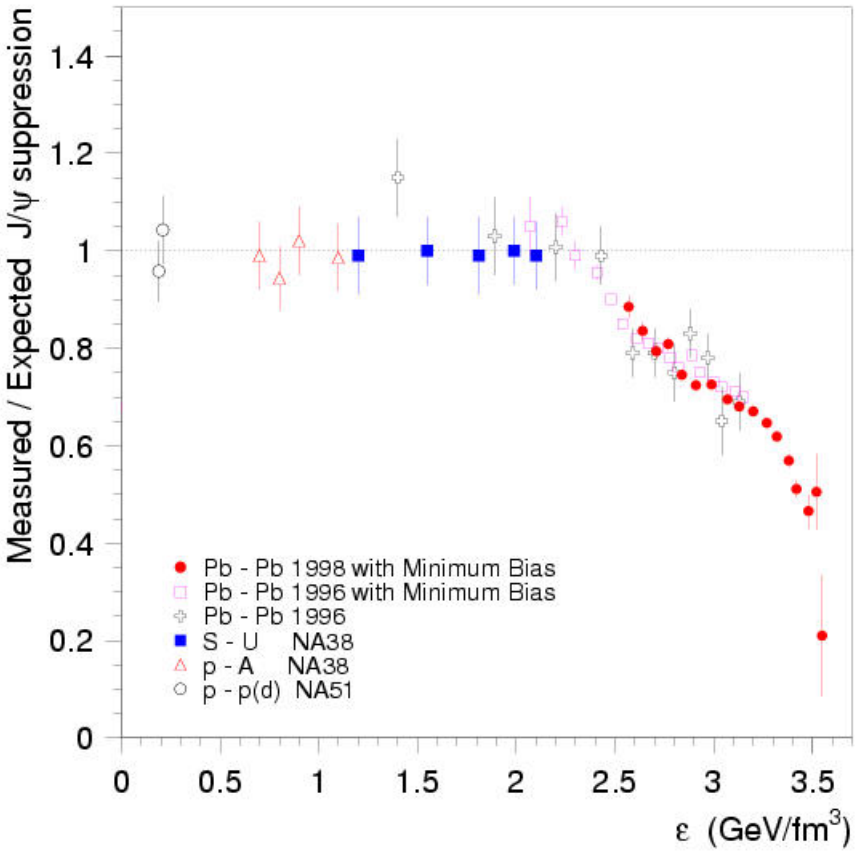

Figure 1.12: The ratio of the measured to the expected charmonium production as a function of energy density for the collisions of the different ion species as measured at SPS [19].

1.4 This work: Why measure single muon production in Cu+Cu collisions?

The main goal of the research presented in this dissertation is to measure the production of open heavy flavor at forward angles in Cu+Cu collisions using the PHENIX detector. Muons are used to tag heavy quarks via their semileptonic decay channel. Those muons can be measured at forward and backward rapidities using the PHENIX muon spectrometers.

There are several important reasons for measuring single muon production in Cu+Cu collisions:

- The production of open heavy flavor and its nuclear modification factor has not been measured at forward angles for any two heavy colliding ion system. The measurement of the nuclear modification factor for heavy flavor production can help to better understand the properties of the medium created as the results of the heavy ion collisions at the forward rapidity, a kinematic region which remains largely unexplored.
- The comparison of heavy flavor measurements in Cu+Cu and Au+Au collisions can help to understand the dependence of the properties of the created medium on the size of the colliding ion species.
- Precisely measuring heavy quark production is very important for a better understanding of the heavy quarkonia production.

The rest of this dissertation is organized as follows: The first part of Chapter 2 is devoted to the phenomenology and experimental measurements on heavy quark production in p+p collisions, followed by a discussion of theoretical models of the

heavy flavor production in relativistic heavy ion collisions with subsequent comparisons with up-to-date experimental measurements. Chapter 3 provides a description of the experimental apparatus used in making this measurement. The details of the extraction of the heavy flavor signal via the single muon measurement using the PHENIX muon arms are provided in Chapter 4. The results are shown in Chapter 5, followed by the concluding discussion in Chapter 6.

Chapter 2

Open heavy flavor

The very dense deconfined matter, thought to be produced in the heavy ion collisions at RHIC, almost completely consists of gluons and light quarks (u, d, s). Heavy flavor, at the RHIC energies represented mainly by the charm quarks and to a lesser extent by the bottom quarks*, would comprise only a very small fraction of this matter. However, for the following reasons, the production of heavy quarks is considered as a very important experimental and theoretical tool for studying the properties of the matter created in the collisions at RHIC:

- Heavy flavor production in p+p collisions provides a crucial baseline measurement for understanding the production of heavy quarks in the heavy ion collisions. It also serves as an important and independent cross check of QCD.
- Because of their large masses, heavy quarks are expected to be produced well before the QGP is formed†. Therefore, they can be utilized as an external

*The maximum CM energies achieved in the collisions at RHIC are below the threshold energy for producing the heaviest *top* quarks $m_t = 178$ GeV/c^2. Conversely, these energies are sufficient for the production of much lighter c and b quarks($m_c \sim 1.5$ GeV/c^2 and $m_b \sim 4.5$ GeV/c^2).

†A typical timescale on which heavy quarks are produced can be calculated by $\tau_Q \sim 1/2m_Q$, which gives about 0.1 fm/c for charm and even less for bottom.

probe of the bulk matter, especially in the earliest stages of its evolution. The interactions with the in-medium partons are expected to modify the kinematics of heavy quarks, leading to the modifications of the subsequent heavy flavor hadron spectra.

- Precisely measuring the production of $c\bar{c}$ pairs is of great importance for the better understanding of the underlying mechanisms that can modify the expected charmonium production in heavy ion collisions.

2.1 Heavy flavor production in p+p collisions

The production of heavy quarks falls into a category of the processes described by the hard scatterings of partons, which in heavy ion collisions occur as a result of the individual inelastic nucleon-nucleon collisions. Therefore, it is important first to understand relevant mechanisms responsible for heavy flavor production in p+p collisions.

Indeed, the main concepts behind heavy flavor production are fairly well understood within the QCD framework, to a large extent due to the large amount of high quality data acumulated over three decades of experimental observations. However, there are still a number of very important open questions which need to be resolved. These along with the heavy flavor related phenomenological issues will be briefly discussed.

2.1.1 Heavy flavor production: Theoretical framework

In p+p collisions, the whole process of heavy flavor creation with the subsequent production of experimentally detectable heavy flavor observables can be described by a sequence of several different processes, as illustrated in Figure 2.1. Initially,

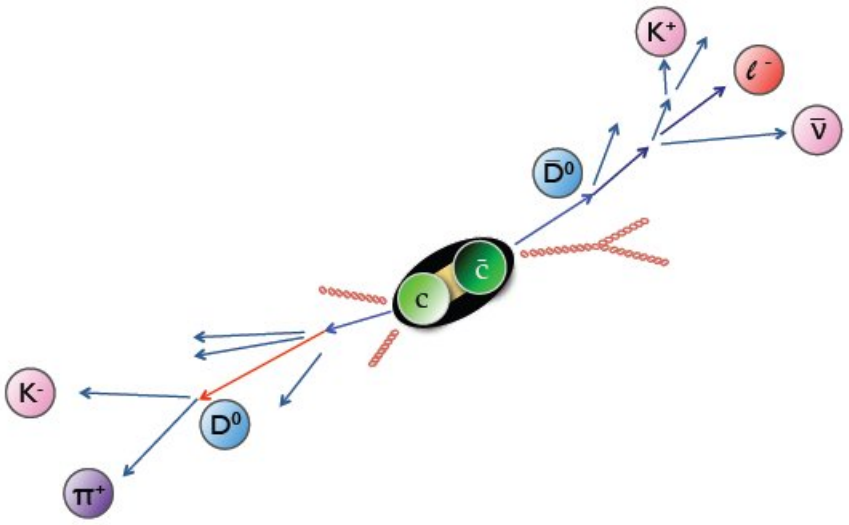

Figure 2.1: An illustration of the hadronization process with the subsequent decay into the product particles of the initially created $c\bar{c}$-pair. Courtesy of Donald Hornback[22].

heavy flavor is created as a result of hard p+p collisions. The created heavy quarks then hadronize into heavy flavor hadrons, which subsequently decay into the final product particles that can be experimentally detected.

Factorization theorem

The first stage that describes the hadron collisions in which the subsequent hard parton collisions result in the initial production of heavy quarks, is indeed well understood within the *factorization theorem* framework [23]. According to the factorization theorem the inelastic cross-section for the production of a heavy quark in a collision of hadron A with hadron B can be written as the following convolution:

$$E\frac{d\sigma_{AB\to Q}}{d^3p} = f_{i/A}(x,\mu) \otimes f_{j/B}(x,\mu) \otimes E\frac{d^3\hat{\sigma}_{ij}(s)}{d^3p} \tag{2.1}$$

where $f_{i/A}(x_i,\mu)$ denotes the probability distribution function (PDF) for the i-th parton (gluons, light quark or anti-quark) inside hadron A for a given energy scale

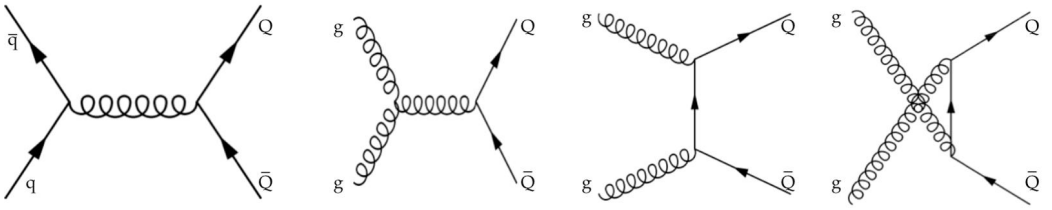

Figure 2.2: Leading Order Feynman diagrams corresponding to the processes of the creation of heavy quark pairs: *quark anti-quark annihilation* (far left) and three different kinematic channels of *gluon-gluon fusion*.

μ and the momentum fraction of hadron A carried by the i-th parton, denoted by x. $\hat{\sigma}_{ij}(s)$ denotes the cross-section of heavy quark production in the collision between i-th and j-th partons, with $\otimes$ indicating a generic convolution.

The factorization theorem implies that in the hadronic collisions heavy quarks are essentially produced as the result of point-like interactions between the partons themselves, not the hadrons. Depending on the specific kinematics of the hadron collisions, these partonic interactions are essentially controlled by the parton PDF's.

The energy threshold needed for the creation of heavy quarks ($\mu \sim 2m_Q$) is much larger than Λ_{QCD}, which implies that the running coupling constant, $\alpha_s(Q)$, is small. Therefore, the cross-section $\hat{\sigma}_{ij}$ can be calculated as a perturbation series in α_s. The leading terms in the series contribute as $\mathcal{O}(\alpha_s^2)$. The equivalent Leading Order (LO) processes for heavy quark production, $q\bar{q} \rightarrow Q\bar{Q}$ and $gg \rightarrow Q\bar{Q}$ are illustrated in Figure 2.2. However, the most important mechanism for the heavy flavor creation at RHIC is gluon-gluon fusion. The annihilation process is expected to be almost irrelevant, since the densities of light anti-partons inside protons or heavy nuclei are much smaller than for gluons.

While bottom production is qualitatively well described with the LO perturbative QCD calculations, the Next-to-Leading Order(NLO) which accounts for $O(\alpha_s^3)$ contribution needs to be included for better prediction of the production of charm[24].

Fragmentation

The nexp step is hadronization, the step in which the originally produced heavy quarks fragment into heavy flavor hadrons. Depending on the kinematics of the created pair of heavy quarks there are two possible scenarios. In the rare case where their moments are aligned, the created heavy Q and $\bar{Q}$ quarks combine together to form a *heavy quarkonium* meson.(Charmonium is a bound state of a $c\bar{c}$ pair, while Bottomonium is a bound state of a $b\bar{b}$ pair). Since the quantum numbers corresponding to their net heavy flavor content are zero, heavy quarkonia particles are often referred as "hidden" heavy flavor mesons.

Most of the time ($> 99\%$), however, the created heavy quarks combine with light quarks to form "open" heavy flavor mesons. D (open charm) mesons are defined as the combinations of either $(c\bar{q})$ or $(\bar{c}q)$. B (open bottom) mesons are defined as the combinations of open bottom mesons consisting of either $(b\bar{q})$ or $(\bar{b}q)$ combinations.

The fragmentation of heavy quarks into open heavy flavor mesons can be approximately visualized through Figure 2.3. While the exact mechanism of the fragmentation process is not known, it is important to understand momentum degradation of a heavy quark caused by combining with a light quarks. This can be described through the fragmentation function, $D_Q^H(z)$, which defines the distribution of the energy carried by the formed hadron with respect to the heavy quark's energy, $z = E_H/E_Q$.

The process of the fragmentation of a quark into a hadron by itself does not depend on how the quark was produced. Thus these fragmentation functions are assumed to be universal. Usually they are extracted from precise measurements made in e^+e^- collisions and used for hadronic collisions. The data on the hadronization of light quarks are well described through the $D_Q^h(z) \propto \dfrac{(1-z)^n}{z}$ parametrization[27].

However, the heavy quarks are expected to retain most of their momenta during

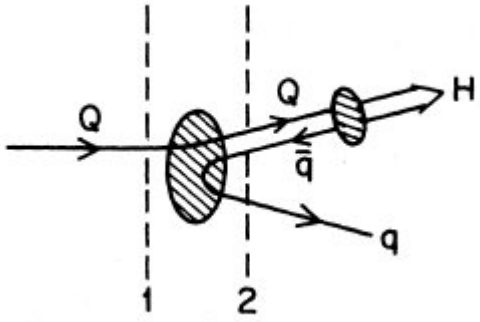

Figure 2.3: A pictorial representation of the heavy quark fragmenation process into heavy flavor meson from [25].

the hadronization process, which implies that, unlike $D_Q^h(z)$ functions for the light quarks, the $D_Q^H(z)$ distributions for the heavy quarks must be peaked closer to $z = 1$ [27], as illustrated on Figure 2.4 where the examples of widely accepted fragmentation functions are shown. The dashed lines represent the fragmentation functions introduced by Peterson et al. [25] parametrized as

$$D_Q^H(z) \propto \frac{1}{z[1-(1/z)-\epsilon_Q/(1-z)]^2} \tag{2.2}$$

with the parameter ϵ_Q, originally introduced as $\epsilon_Q = (m_q/m_Q)^2$, fixed at 0.06 for charm and 0.006 for bottom. This function has a maximum at $z \approx 1 - \sqrt{\epsilon_Q}$. The solid lines, corresponding to a harder fragmentation scheme, represent the predictions based on the Lund string model [26] parametrized as

$$D_Q^H(z) \propto \frac{(1-z)^a}{z^{1+bm_Q}} e^{-\frac{bm_T^2}{z}} \tag{2.3}$$

with $a = 0.3$, $b = 0.58$ GeV^{-2}, $m_c = 1.5$ GeV/c^2 and $m_b = 4.8$ GeV/c^2. The Lund fragmentation scheme is used by PYTHIA.

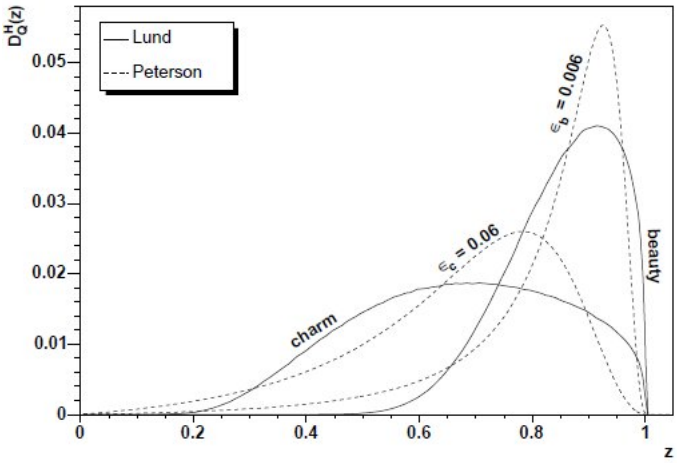

Figure 2.4: The comparison of the heavy quarks fragmentation functions. "(dashed lines)" the parametrization from Peterson et al. [25]. "(solid lines)" and the Lund string model parametrization [26].

Decay

The lifetime of heavy flavor mesons is very short, $\tau \sim 10^{-12} - 10^{-13}$ s. Therefore they can only be experimentally detected through their decay products ("daughter particles"). Generally, heavy flavor mesons, as well as most of the resonance particles, may decay through multiple different decay channels. The probability of each decay process to occur, called its *branching ratio*, is an experimentally measurable quantity which is used to extrapolate backwards to determine the production rate of the original resonance particles of interest.

Two particular types of decay processes occuring for the heavy flavor mesons, *hadronic decays* and *semileptonic decays*, are of particular interest for the RHIC experiments. In general, "hadronic decay" is the name given to a process in which a produced heavy flavor meson(s) decays exclusively into hadrons, as in the example illustrated on the left in Figure 2.1 where the D^0 meson decays into $K^-\pi^+$ hadrons. In this case, the D^0 meson can be directly identified through measuring the invariant mass

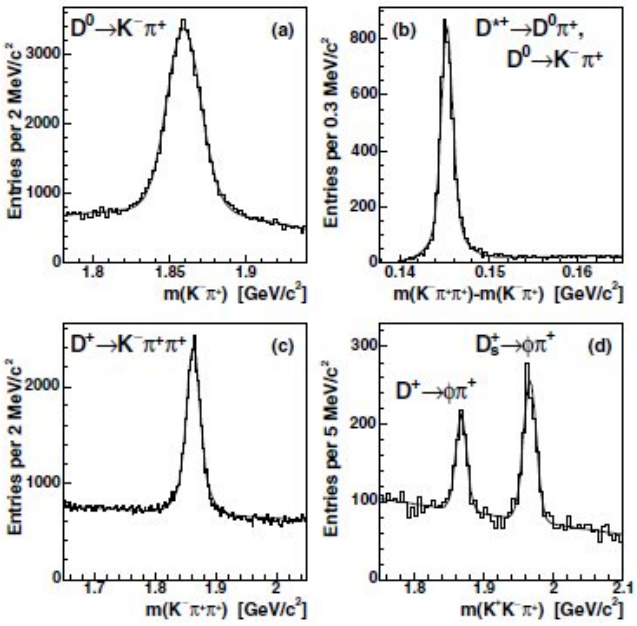

Figure 2.5: The invariant mass of the various D-meson species measured in the $p\bar{p}$ collisions at $\sqrt{s} = 1.92$ TeV with the CDF experiment [28].

of the system of decay products[‡]. An example of this type of measurement is shown on Figure 2.5.

Very often, however, it is impossible to experimentally reconstruct all decay products resulting from the decays of the parent resonances. One of those cases is a semileptonic decay of the open heavy flavor mesons, resulting in production of a hadron, a neutrino and an electron or a muon, as illustrated in the right side of Figure 2.1. Of all produced daughter particles in this case, only the electrons(muons) are usually experimentally measured. These "single" leptons are then used to tag the parent heavy flavor mesons, providing an "indirect" measurement of the heavy flavor production. Measuring heavy flavor production using single muons reconstructed in the PHENIX detector is the main goal of the research presented here.

This approach has two potential experimental and phenomenological challenges.

[‡]Using measured energy and momenta of the decay products, one can calculate invariant mass of the system $M^2 = \left(\sum_i E_i\right)^2 - \left(\sum_i p_i\right)^2$, which is the mass of the parent meson.

First of all, one needs to carefully identify all sources of leptons other than open heavy flavor mesons and subtract their contribution from the total inclusive spectra of the measured leptons. Secondly, because of the semileptonic decay kinematics, the resulting single lepton spectra would be different from the orginal p_T spectra of heavy flavor mesons which needs to be carefully taken into account in the theoretical models predicting single lepton production. For the extensive survey of the theory and available experimental results on decay kinematics of the semileptonic decay the reader is referred to [29], [30] and [31].

2.1.2 Single lepton production phenomenology: FONLL

The theoretical models that predict the single lepton production in the p+p collisions should consist of three ingredients precisely reflecting the above discussed sequence of procesess related to the heavy flavor production: (1) The invariant cross section of the heavy quarks calculated within the pQCD framework; (2) The fragmentation functions deduced from the comparison of the selected fragmentation model to the e^+e^- data; and (3) the final lepton spectra resulting from the decays of heavy flavor mesons. The invariant cross section for the lepton production, therefore, can be written as

$$E\frac{d^3\sigma(l)}{d^3p} = E_Q\frac{d^3\sigma(Q)}{d^3p_Q} \otimes D(Q \to H_Q) \otimes f(H_Q \to l) \tag{2.4}$$

where $E_Q\frac{d^3\sigma(Q)}{d^3p_Q}$ is the heavy quark production invariant cross section, calculated using the factorization theorem. $D(Q \to H_Q)$ and $f(H_Q \to l)$ represent the heavy quark fragmentation function and the single lepton spectrum from the heavy flavor meson decays, respectively.

FONLL [32], an acronym for of "Fixed-Order(FO) plus Next-to-Leading-Log(NLL)", is perhaps the most advanced theoretical framework that predicts heavy flavor production by incorporating the scheme described by Equation 2.4 and is most often

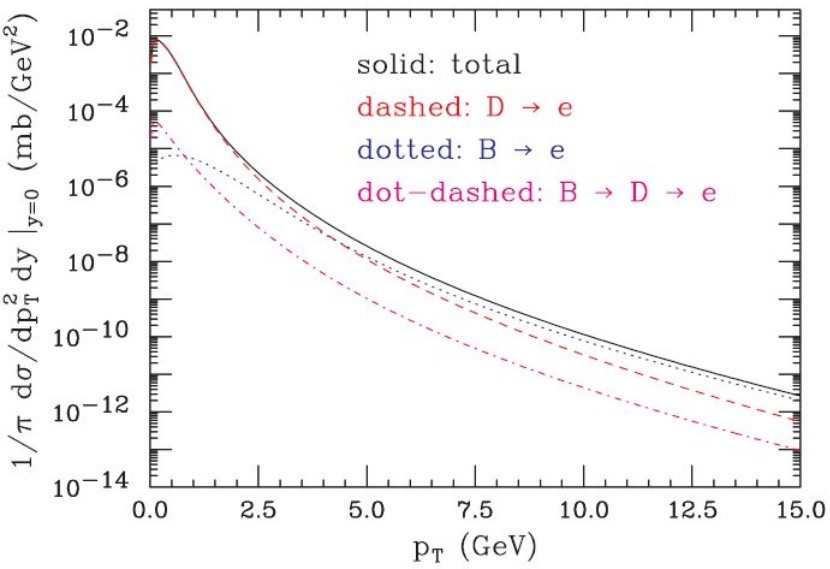

Figure 2.6: The FONLL prediction of the invariant cross section of non-photonic $e^{\pm}$'s, electrons resulting from the semileptonic decays of heavy flavor mesons. At lower p_T the spectra is dominated by heavy flavor electrons from $D \rightarrow e$. Above $p_T = 5.0$ GeV/c electrons are mainly produced from B decays.

compared to the RHIC heavy flavor data. Within the FONLL framework the heavy quark production cross section, $E_Q \frac{d^3\sigma(Q)}{d^3 p_Q}$, is calculated by including both the standard fixed-order NLO results and the resummation of large perturbative terms propotional to $\alpha_s^n log^k(p_T/m)$ arising from renormalization/factorization scale dependence [33], especially at high p_T[§].

The fragmentation functions for the charm and bottom quarks, $D(c \rightarrow D)$ and $D(c \rightarrow B)$, used with the FONLL scheme are extracted from the e^+e^- data using the parametrizations from [34] and [35].

For predicting the total single lepton spectrum from the decays of heavy flavor mesons, firstly the individiual lepton spectra resulting from $D \rightarrow l$, $B \rightarrow l$ and $B \rightarrow D \rightarrow l$ decays are combined. These are extracted from BABAR and CLEO

[§]In the low p_T regime where the effective scale is the mass of heavy quark, m_Q, these $\alpha_s^n log^k(p_T/m)$ terms are almost negligible compared to standard NLO terms in the perturbative expansion. At the $p_T \geq m_Q$ regime logarithmic terms become important, and therefore must be included [33].

data, [36] [37]. At the final stage, single lepton spectra are normalized by using corresponding branching ratios from [38] and the chemistry of the production of D and B mesons.

2.2 Open heavy flavor measurements in p+p collisions at RHIC

2.2.1 RHIC results

The major experiments at RHIC, PHENIX and STAR, are designed to measure heavy flavor production by using both the direct measurement of heavy flavor mesons, and single lepton production.

While the PHENIX detector can measure heavy flavor mesons through the hadronic decay channel, it is optimized to measure single lepton production in several rapidity ranges. Indeed, PHENIX has measured single lepton production both in the form of non-photonic electron spectra at mid-rapidity [39], as well as in the form of single muon spectra at forward/backward rapidity [40], as shown on Figure 2.7. In each case, for calculating the total charm cross section at a given rapidity, the measured p_T spectra are extrapolated to $p_T = 0$ GeV/c using a spectral shape derived from a FONLL prediction [32]. Figure 2.7 shows the PHENIX measurements of the charm cross section, $dN_{c\bar{c}}/dy$, at mid and forward rapidities compared to FONLL predictions. Within the systematic uncertainties, the measured data points are compatible with theoretical predictions. However, the exact rapidity evolution cannot be precisely verified due to large systematic uncertainties. The total charm cross section extracted from the $\frac{dN_{c\bar{c}}}{dy}|_{y=0}$ distribution is $\sigma_{c\bar{c}} = 567 \pm 57(\text{stat}) \pm 224(\text{sys})\ \mu b$. This result is in good agreement with another PHENIX charm cross section measurement,

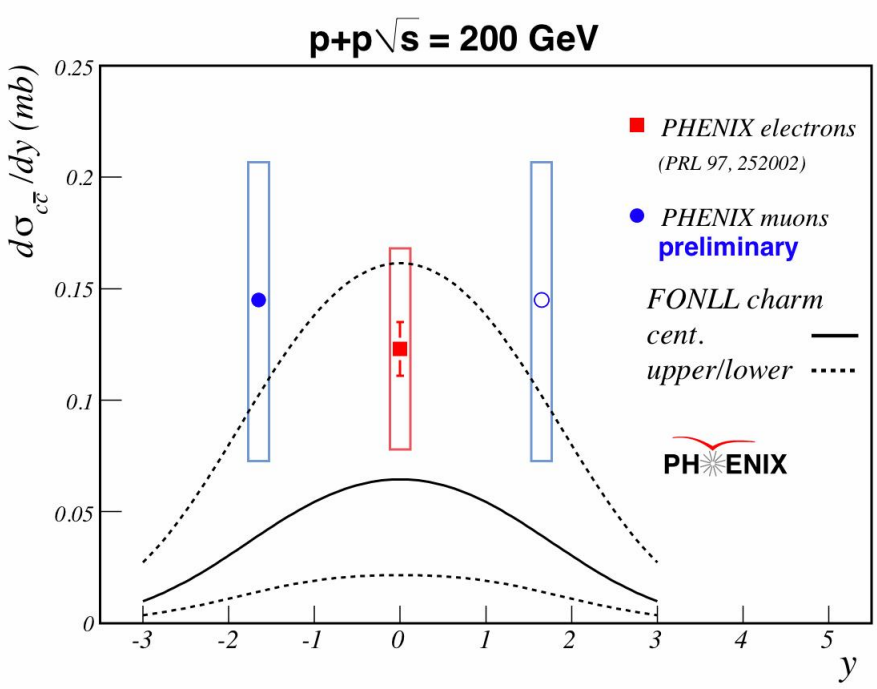

Figure 2.7: The PHENIX measurement of the total charm cross section, $dN_{c\bar{c}}/dy$, at y = 0, and ±1.65 compared to the corresponding FONLL prediction.

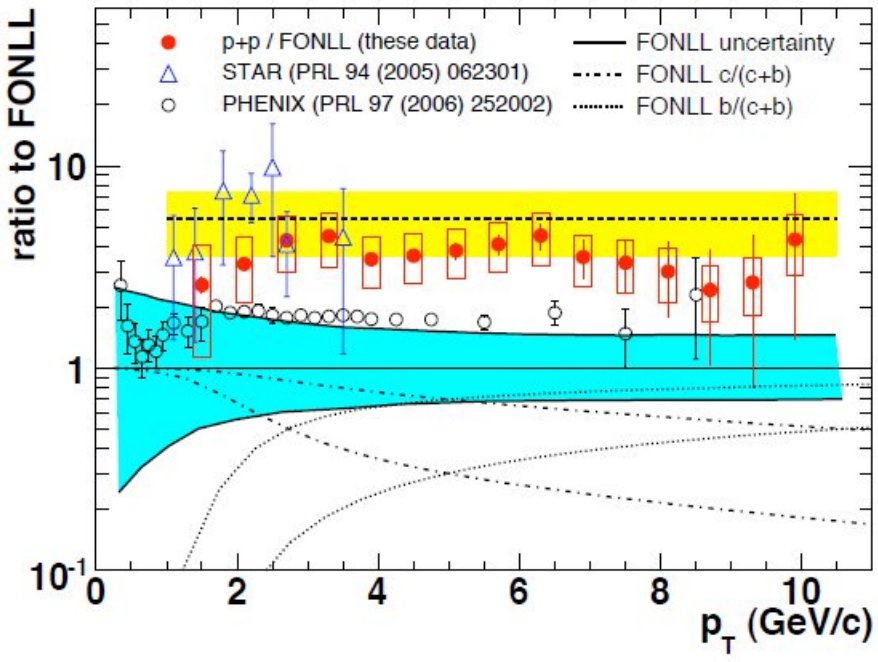

Figure 2.8: Comparison of ratio to FONLL predictions for open heavy flavor measurements reported by STAR and PHENIX.

derived from electron-positron pair correlation (di-electron) analysis [41], $\sigma_{c\bar{c}} = 544 \pm 39(\text{stat}) \pm 142(\text{sys}) \pm 200(\text{model})\ \mu b$.

The STAR experiment with its 4π solid angle coverage is optimized to make the direct measurements of heavy flavor mesons and non-photonic electrons. It also has an ability to measure non-photonic leptons, despite, relative to PHENIX, a larger amount of detector material which introduces additional $e^{\pm}$ background due to photon conversions. The total charm cross section is calculated from combining non-photonic electron spectra with the direct D^0-meson measurement [42].

The total charm cross section measured by STAR [43], as well as their non-photonic electron spectra are about a factor of 2 above those of PHENIX, as shown in Figure 2.8. At this point this difference is still unresolved.

By selecting a sample of non-photonic electrons in the offline analysis, PHENIX was also able to measure the charm to bottom ratio via partial $D/\overline{D} \rightarrow e^{\pm}K^{\mp}\text{X}$ (K unidentified) reconstruction [44]. This ratio is then used to extract the total bottom cross section, which is measured to be $\sigma_{b\bar{b}} = 3.2 \pm {}^{1.2}_{1.1}(\text{stat}) \pm {}^{1.4}_{1.3}(\text{sys})\ \mu b$. Independently, the cross section of bottom quark production was extracted from a di-electron analysis yielding $\sigma_{b\bar{b}} = 3.9 \pm 2.5(\text{stat}) \pm {}^{3}_{2}(\text{sys})\ \mu b$.

2.3 Heavy quarks in QGP

Heavy quarks in heavy ion collisions are created in hard point-like processes. Therefore, in the heavy ion collisions, the total number of the initially produced $c\bar{c}$ pairs is expected to scale with the number of binary collisions [45]. Once quarks are created they travel through the medium with a large density of color charges, which is believed to be present after the collisions of heavy ions. As a consequence of the multiple scatterings with the in-medium partons, intially created quarks lose a part of

their energy, subsequently leading to a modification of the heavy flavor hadron spectra. In this case, the lepton production cross section, calculated from Equation 2.4 for p+p collisions, can be rewritten as

$$E\frac{d^3\sigma(l)}{d^3p} = E_i\frac{d^3\sigma(Q)}{d^3p_i} \otimes P(E_i \rightarrow E_f) \otimes D(Q \rightarrow H_Q) \otimes f(H_Q \rightarrow l) \tag{2.5}$$

where $P(E_i \rightarrow E_f)$ denotes the probability of energy loss.

In principle, the amount of the energy lost by a quark traversing through the medium, ΔE, depends on the properties of the quark itself such as mass (m_Q), energy (E) and charge. On the other hand, ΔE also depends on the characteristics of the medium such as thickness(L), temperature (T), coupling constant (α_s), etc. Therefore the amount of the energy lost can provide information about these key properties of the medium.

Depending on their kinematics, there are two major mechanisms through which quarks can lose their energy, illustrated in Figure 2.9:

- **radiative energy loss** caused by medium-induced inelastic scatterings in which the quarks traversing the medium radiate gluons (*gluon bremsstrahlung*), is expected to dominate at higher p_T.
- **collisional energy loss** occuring due to elastic collisions with the abundant in-medium partons becomes important at lower p_T.

The total energy loss is expected to be a result of the interplay between these two effects ($\Delta E = \Delta E_{rad} + \Delta E_{rad}$).

The radiative energy loss occurs when a quark (probe) undergoes strong inelastic interactions with the in-medium partons, subsequently radiating gluon(s), $Qg \rightarrow Qgg$ or $Qq \rightarrow Qqg$. This is almost identical to the electron bremsstrahlung in Quantum

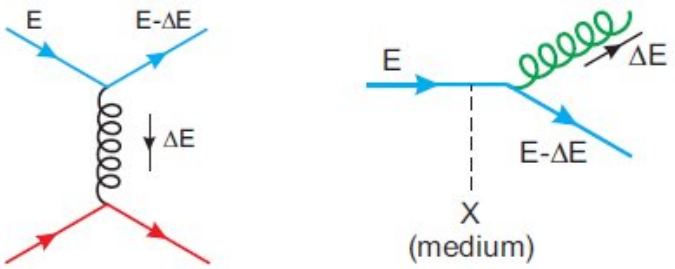

Figure 2.9: Diagram of the collisional and radiative energy loss mechanisms from [46].

Electro Dynamics (QED).

The amount of the energy lost in one inelastic scattering can be calculated as follows:

$$\Delta E^1_{rad} = \int^E \omega \frac{dI_{rad}}{d\omega} d\omega \tag{2.6}$$

where $\omega \frac{dI_{rad}}{d\omega}$ defines the gluon brehmasstrahlung spectrum and ω is the energy of the radiated gluon. The average number of those interactions, called the *medium opacity*, can be calculated via $\bar{n} = \frac{L}{\lambda}$, with λ being the *mean free path*[¶]. Assuming that all inelastic scatterings occur incoherently, the total radiative energy loss is $\Delta E_{rad} = \bar{n} \Delta E^1_{rad}$. In direct analogy with QED one can calculate stopping power as

$$-\frac{dE}{dl} \approx \frac{\langle \Delta E_{rad} \rangle}{L} \approx \frac{\langle \Delta E^1_{rad} \rangle}{\lambda} \tag{2.7}$$

In a realistic scenario a traversing quark is expected to undergo several inelastic interactions with in-medium partons. In this case, the gluon radiation can be described analogously to the Landau-Pomeranchuk-Migdal (LPM) radiation introduced in QED theory [47],[48]. According to the LPM theory, two qualitatively different gluon radiation regimes are possible with respect to the *characteristic energy scale*

[¶]The mean free path is defined as $\lambda = 1/(\rho\sigma)$, where ρ and σ are the density of matter and the integrated cross section of the interaction of the traversing particle with the medium partons, respectively

of the radiated gluons

$$\omega_c = \frac{1}{2}\hat{q}L^2 \tag{2.8}$$

where $\hat{q}$, the *scattering power* of the QCD medium, is defined as

$$\hat{q} \equiv \frac{{\mu_D}^2}{\lambda} \tag{2.9}$$

with $\mu_D = 1/r_D$ as the *Debye mass* representing a typical magnitude of momentum transfer in the interactions with the medium, $\mu_D^2 \sim \langle Q^2 \rangle$ [49].

In the $\omega < \omega_c$ regime, the gluon radiation spectra can be approximated as

$$\omega \frac{dI_{rad}}{d\omega} d\omega \approx \alpha_s \sqrt{\hat{q}L^2/\omega} \tag{2.10}$$

which for the total energy loss gives

$$\Delta E_{rad} \approx \alpha_s \hat{q} L^2. \tag{2.11}$$

On the other hand, in the case of $\omega > \omega_c$ one has

$$\omega \frac{dI_{rad}}{d\omega} d\omega \approx \alpha_s \hat{q} L^2/\omega \tag{2.12}$$

which for the total energy loss gives

$$\Delta E_{rad} \approx \alpha_s \hat{q} L^2 ln(E/(\hat{q}L^2)). \tag{2.13}$$

While the gluon radiation spectrum is steeply falling, it is also suppressed for small ω values. This means that the radiative energy loss is mainly due to the region right below ω_c. Therefore the overall radiative energy loss in the medium is expected to be L^2 dependent($\Delta E_{rad} \approx \alpha_s \hat{q} L^2$).

It turns out that there is a significant difference in between the gluon bremsstrahlung

process for heavy quarks and for light quarks in vacuum. The gluon radiation spectrum for heavy quarks at small angles can be described by:

$$\omega \frac{dI_{rad,Q}}{d\omega} \approx \omega \frac{dI_{rad,q}}{d\omega} \cdot \left(1 + \frac{\theta_0^2}{\theta^2}\right)^{-2} \tag{2.14}$$

where $\theta_0 \equiv \frac{M}{E}$. Equation 2.14 shows that for $\theta < \theta_0$ gluon radiation for heavy quarks is largely suppressed compared to light quarks [50]. This is called the "dead cone" effect. Because of the dead cone effect, heavy quarks in the medium are expected to lose less energy since they radiate less gluons. The heavier the quark, the stronger is the effect. This is illustrated in Figure 2.10, which shows the theoretical prediction of the DGLV energy loss model [51] based on the radiative and collisional mechanisms, $\Delta E/E$, for c,b and light quarks. As can be clearly seen c quarks are expected to lose significantly less energy than light quarks. On the other hand, the difference in the expected energy loss between b and c quarks is predicted to be even more significant.

Before the first RHIC heavy flavor data for heavy ion collisions became available, conventional theoretical models for jet-quenching were based solely on the radiative energy loss mechanism, disregarding possible effects of elastic collisions with in-medium partons.

It was a surprise, therefore, when the first heavy flavor data measured in Au+Au collisions became available. The measured spectra for non-photonic $e^{\pm}$'s in the most central Au+Au collisions at $p_T > 4$ GeV/c [45],[43] were suppressed almost as much as the light vector meson spectra[52]. An even bigger surprise was that PHENIX measured a very substantial elliptic flow, v_2, for non-photonic electrons up to $p_T \sim$ 6 GeV/c [40], suggesting that heavy quarks may flow and even thermalize with the medium [53].

Theoretical calculations based exclusively on the radiative energy loss mechanism can in principle provide a good matching with data by artificially increasing gluon

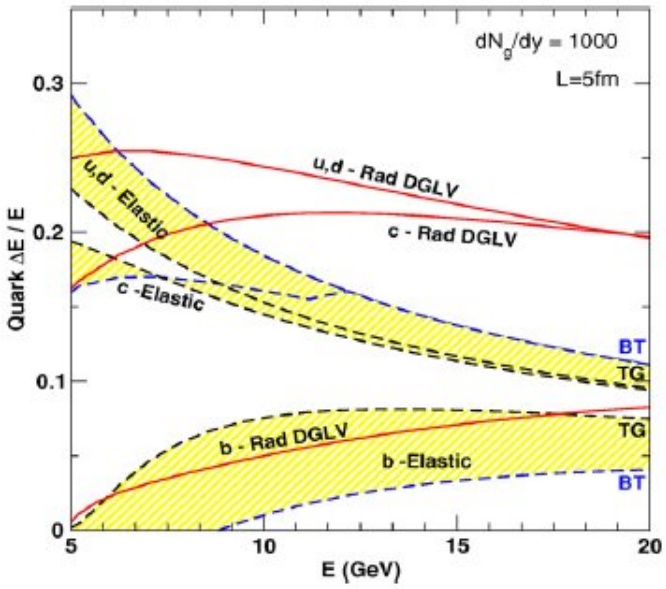

Figure 2.10: A DGLV prediction of collisional and radiatine energy losses for the different parton species.

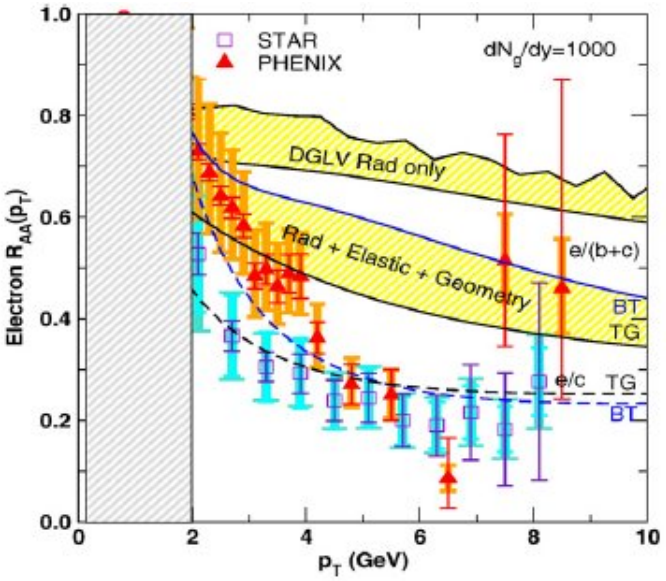

Figure 2.11: R_{AA} for non-photonic $e^{\pm}$ spectra measured at RHIC compared to two different DGLV model predictions: (1) for only radiative energy loss and (2) radiative and collisional energy loss.

densities or $\hat{q}$ of the medium [54]. However, in this case they significantly undepredict the observed elliptic flow of heavy flavor mesons [45].

This reinforced the need for more careful theoretical consideration of the initially disregarded collisional energy loss mechanism. Indeed, a theoretical model describing 5-10 GeV charm quarks in the expanding plasma [55] estimated that the magnitude of collisional energy loss is at least as significant as that of radiative energy loss. Independently, the importance of elastic collisions with the in-medium partons was emphasized in Langevin-based simulations describing heavy quark diffusion in the medium [56],[57]. While the predictions from these models were able to match the observed data reasonably well, they also indicated a strong correlation between the nuclear modification factor and the elliptic flow.

The collisional dissociation model of heavy flavor mesons in a QGP [58] is another interesting alternative which predicts the R_{AA} of the non-photonic electron spectra resonably well. The main idea of this model is, that if a significant fraction of the originally produced heavy quarks hadronize into heavy flavor mesons before or shortly after timescale τ_{form}, they may dissociate while being inside the QGP due to the collisions with the in-medium partons, causing the subsequent suppression of high-p_T spectra. This is exactly the same mechanism as for the dissociation of J/ψ particles inside the QGP suggested in [59]. The qualitative difference of this model from the other predictions is that the suppression of B-mesons is expected to be comparable to that of D-mesons. While the measured non-photonic electron specra was predicted well, as illustrated in Figure 2.12, the prediction of the corresponding v_2 variable from this model has not been introduced.

Two things are clear at this point. Although there has been a significant progress in the phenomenological understanging in the underlying mechanisms leading to the large suppression and a significant elliptic flow observed for heavy flavor hadron spectra, the theory still cannot provide a comprehensive interpretation, which si-

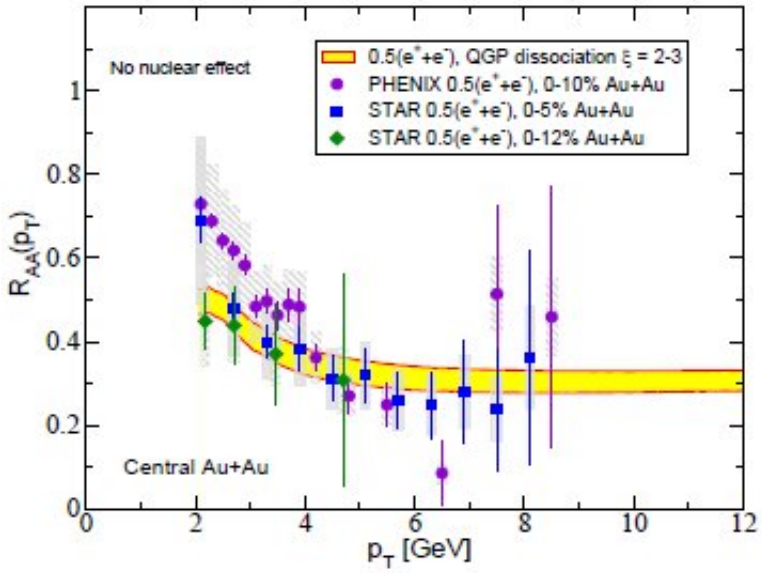

Figure 2.12: The comparison of the collisional dissociation model prediction to the non-photonic electron spectra measured by STAR and PHENIX.

multaneously and precisely predicts both of these observables. On the other hand, more precise experimental measurements providing better constraints for the existing models are needed, specifically better measurements of the spectra of the charm to bottom production ratio.

Chapter 3

The experimental apparatus

3.1 RHIC

The relativistic heavy ion collider (RHIC), the first collider built specifically to facilitate ultra-relativistic heavy ion collisions, is located at the Brookhaven National Laboratory (BNL) on Long Island, NY.

A schematic view of the entire RHIC facility is illustrated on Figure 3.1. The biggest part of RHIC is the 3.8 km ring housing two separate superconducting magnet rings, often referred as beamlines, where the beams of the fully stripped from the electrons ions accelerated to 99.7% of the speed of light are injected*. The beamlines cross each other at six different places where the collisions between the heavy nuclei from the different beamlines can occur. The four RHIC experiments BRAHMS, PHENIX, PHOBOS and STAR were built around four out of the six intersection points to study these collisions.

*Before being injected into the collider ring a beam of a particular heavy ion species goes through the chain of processes, starting from the atom at rest. For the detailed description of this process the reader is referred to [22].

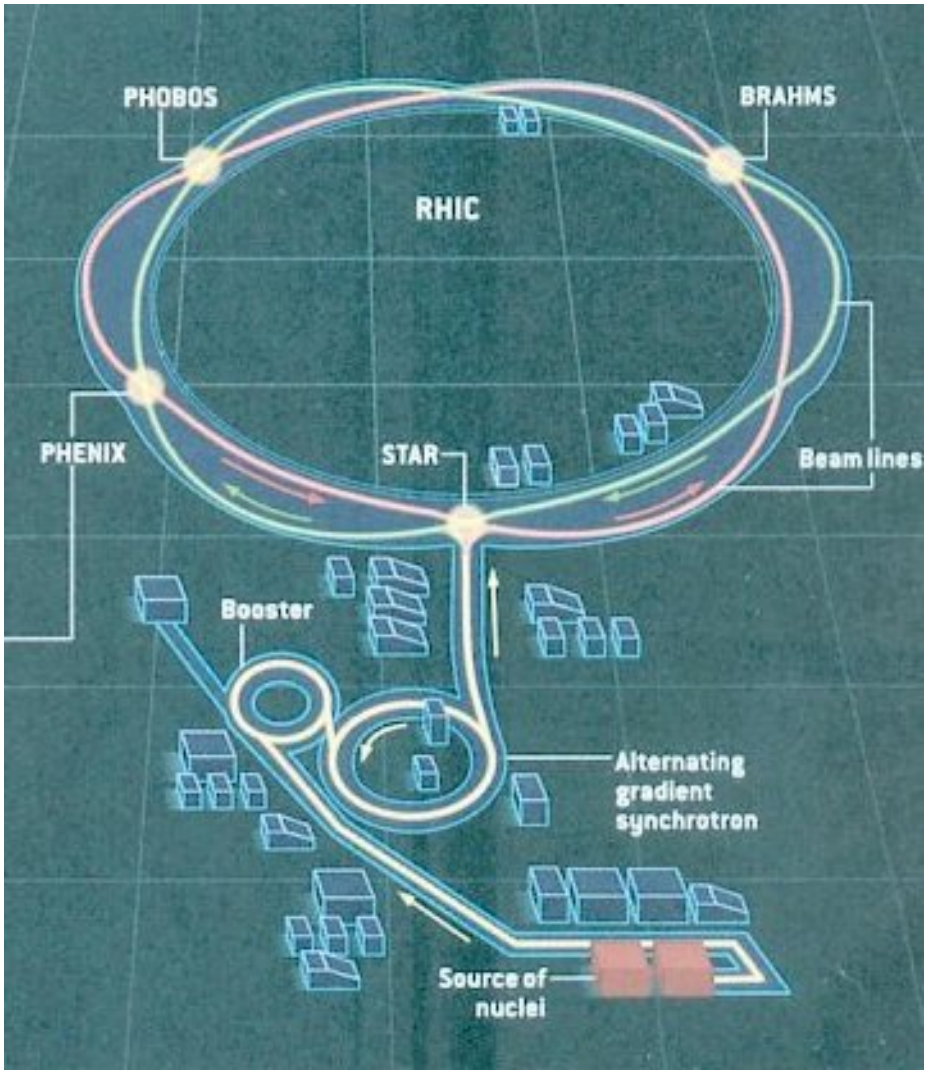

Figure 3.1: Schematic view of the RHIC facility.

The RHIC has a capability of accelerating beams of the different heavy ion species to the maximum energy of 100 GeV per nucleon, resulting thus in the maximum CM energy per nucleon-nucleon collision of $\sqrt{s_{NN}} = 200$ GeV. In 2009 RHIC achieved $\sqrt{s} = 500$ GeV for protons-proton collisions.

Since 2000, when the very first collisions were observed, RHIC has been able to deliver the collisions of the different nuclei species for a wide range of CM energies, as described in detail in Table 3.1. The research presented in this dissertation has been performed for the data from Cu+Cu collisions at $\sqrt{s_{NN}} = 200$ GeV collected during the RHIC Run 5 period in 2005.

3.2 The PHENIX experiment

PHENIX (**P**ioneering **H**igh **E**nergy **N**uclear **I**nteraction e**X**periment)[60] is one of the leading nuclear physics experiments in the world primarily designed to make a wide variety of measurements for studying the properties of the matter created in heavy ion collisions.

The PHENIX detector is illustrated in Figure 3.2. The beams inside the beampipe collide at the interaction point (IP), which is taken to be the origin of the PHENIX coordinate system. In both Cartesian and cylindrical coordinate systems, adopted by PHENIX, the z-axis runs along the beamline with South to North (left to right in the figure) corresponding to the positive direction. The kinematic acceptance of the PHENIX detector is shown in Figure 3.3.

The entire detector can be nominally subdivided into three main parts. The first part essentially consists of the two global subdetectors [61], Beam-Beam Counter(BBC) and Zero-degree calorimeter(ZDC) (ZDC has not been operational starting from RHIC Run 5). The BBC detector provides the measurement of the global event

Table 3.1: The table describing collision species, CM energy, PHENIX sampled luminosity and the total number of events for the first eight RHIC runs since 2000. The presented single muon analysis has been performed using RHIC Run-5 data corresponding to Cu+Cu collisions at $\sqrt{s_{NN}} = 200$ GeV.

	Year	Species	$\sqrt{s}$ [GeV]	$\int$Ldt	$N_{tot(sampled)}$	Data Size
Run-1	2000	Au-Au	130	1 μb^{-1}	10 M	3 TB
Run-2	2001/02	Au-Au	200	24 μb^{-1}	170 M	10 TB
		Au-Au	19		< 1 M	
		p-p	200	0.15 pb^{-1}	3.7 B	20 TB
Run-3	2002/03	d-Au	200	2.74 nb^{-1}	5.5 B	46 TB
		p-p	200	0.35 pb^{-1}	6.6 B	35 TB
Run-4	2003/04	Au-Au	200	24 μb^{-1}	1.5 B	270 TB
		Au-Au	62.4	9 μb^{-1}	58 B	10 TB
Run-5	2004/05	Cu-Cu	200	24 μb^{-1}	170 M	173 TB
		Cu-Cu	62.4	0.19 pb^{-1}	3.7 B	48 TB
		Cu-Cu	22.4	2.7 μb^{-1}	3.7 B	1 TB
		p-p	200	3.8 pb^{-1}	85 B	262 TB
Run-6	2006	p-p	200	10.7 pb^{-1}	233 B	310 TB
		p-p	62.4	0.1 pb^{-1}	10 B	25 TB
Run-7	2007	Au-Au	200	725 μb^{-1}	4.6 B	570 TB
Run-8	2007/08	d-Au	200	81 nb^{-1}	160 B	437 TB
		p-p	200	5.7 pb^{-1}	115 B	140 TB
		Au-Au	9.2		few K	

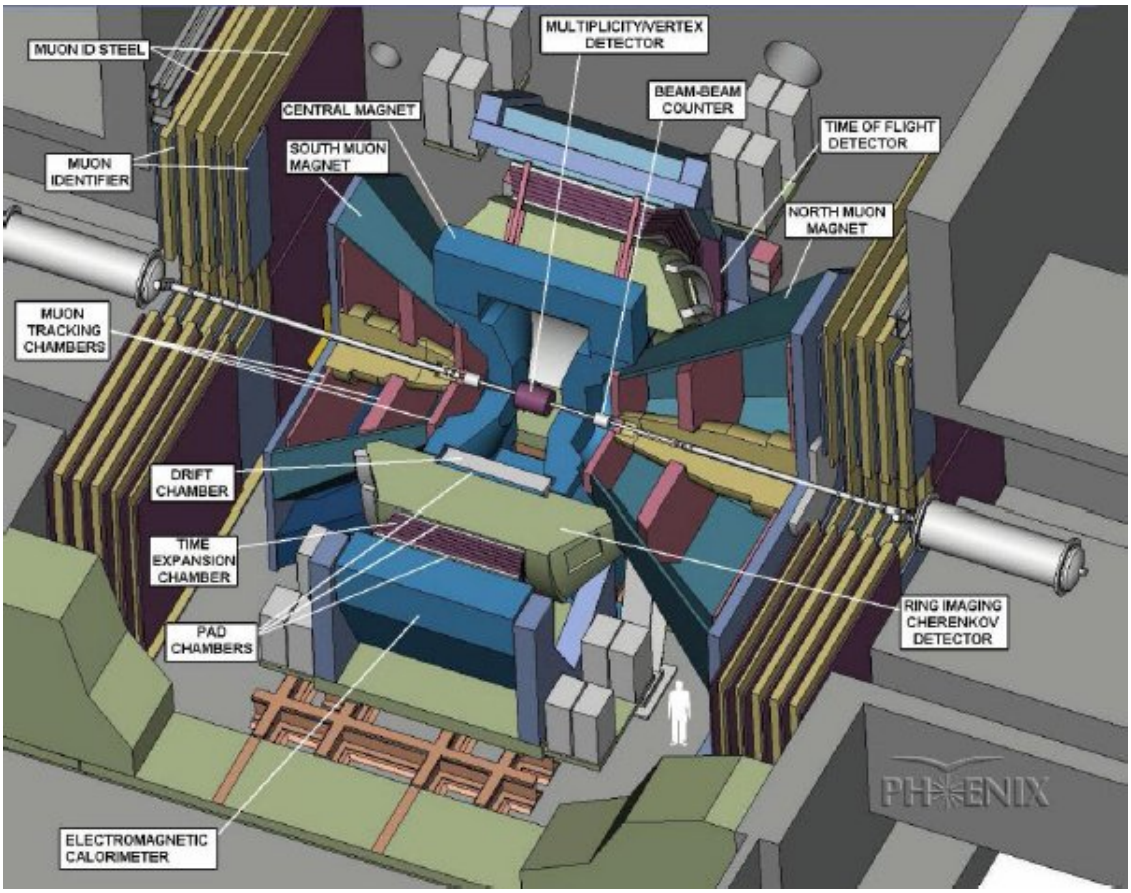

Figure 3.2: 3D illustration of the entire PHENIX detector.

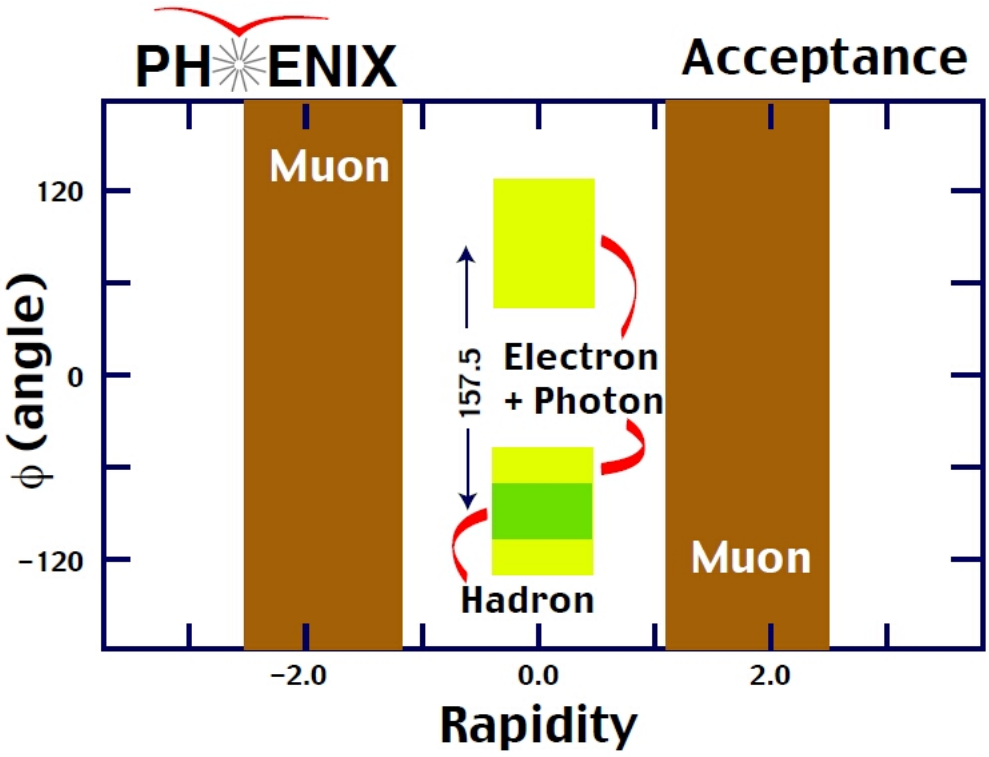

Figure 3.3: The kinemtaic acceptance of the PHENIX detector.

characteristics, such as the z-coordinate of the collision vertex and the event centrality. Additionally, it plays a major role in the PHENIX triggering scheme, providing the selection of the "MinBias" events.

The second part is represented by the pair of "central arms", consisting of several different subdetector systems: Drift Chambers (DC), Pad Chambers (PC), ring-imaging Cherenkov detectors (RICH), Electromagnetic calorimeter (EMCal), Time Expansion Chamber (TEC) and Time-of-flight (TOF) detector. Each of the two central arms provide the kinematic coverage of $|\eta| \leq 0.35$ in pseudo-rapidity and π angle in azimuth, where electrons, photons and charged hadrons can be measured.

The third part is the pair of the muon spectrometers, referred to as the North and South "arms", designed to measure muon tracks within the $1.2 \leq |\eta| \leq 2.2$ rapidity range and full coverage in azimuth, as shown on Figure 3.3. The presented

measurement is made from the data reconstructed by the muon arms, therefore they will be described in more details here.

3.3 The PHENIX muon arms

The PHENIX Muon Arms provide a unique ability to measure muons in forward and backward rapidities, which benefitstudies of the production of vector mesons, the Drell-Yan process and the production of heavy quarks. Additionally, the ability to reconstruct high p_T single muons provides a tool to study the production of the Z and W particles, which play a significant role in the spin physics program.

Each of the two muon arms consists of a muon tracker, which provides the momentum measurement, and a muon identifier, designed to separate muons from hadrons. The tracker in the South arm is 1.5 m shorter in z compared to the tracker in the North arm to facilitate removal of its magnet from the collisions hall. On the other hand, the muon identifiers are almost identical between the two arms.

3.3.1 The muon tracker detector

The muon tracker detector (MuTR), with its spatial resolution of about 100 μm, corresponding to the relative mass resolution of about $\sigma(M)/M = 6\%/\sqrt{M}$, provides the ability for clear separation of the ρ/ω peak from ϕ, J/psi and $\psi^{'}$, and satisfactory separation of Υ and $\Upsilon^{'}$.

The MuTR, which is placed inside the muon magnet frame, as illustrated in Figure 3.4, consists of three octant-shaped stations of tracking chambers with cathode-strip readout. The numbering convention of the MuTR stations is illustrated on Figure 3.5. Stations 1 and 2 consist of three layers ("gaps") and Station 3 composed from 2

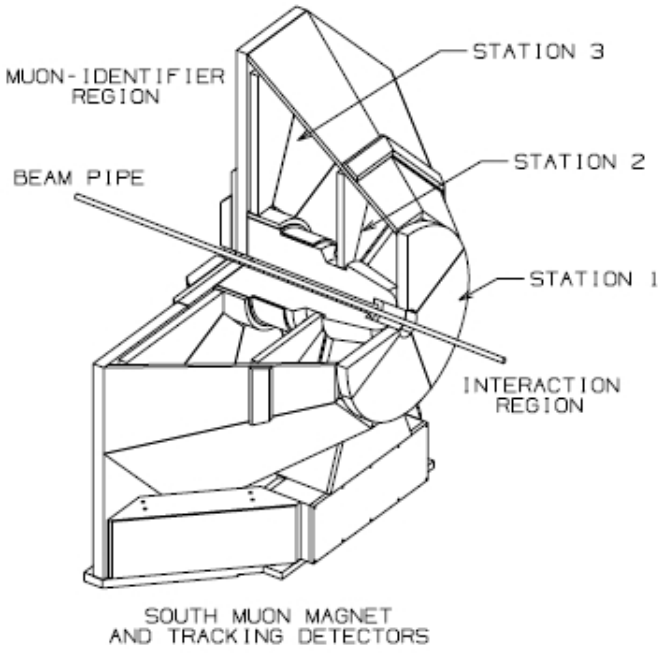

Figure 3.4: Drawing of the South muon arm tracking spectrometer.

layers ("gaps"). Each gap consists of the plane of almost azimuthally running anode wires, which is sandwiched between two planes with 1 mm wide cathode strips. Only cathode strips are read out. In the first plane the cathode strips run radially, exactly perpendicular to the anode wires. In the second plane, the cathode strips are positioned at the stereo angles within $\pm 11.5^{\circ}$ with respect to the perpendicular strips. This specific configuration of strips results in a position resolution of 100 μm.

The MuTR chambers are operated with a 50:30:20 (non-flammable) gas mixture of Ar:CO_2:CF_4 at a typical voltage of 1850 V on the anode wires.

The momentum of a charged particle traversing the MuTR is measured using the bend in its trajectory (sagitta) due to the influence of the magnetic field. According to the Lorentz law only the perpendicular component of the velocity vector is affected by the magnetic force, therefore the bend in trajectory is in the perpendicular direction with respect to the magnetic field. The momentum of the track can be

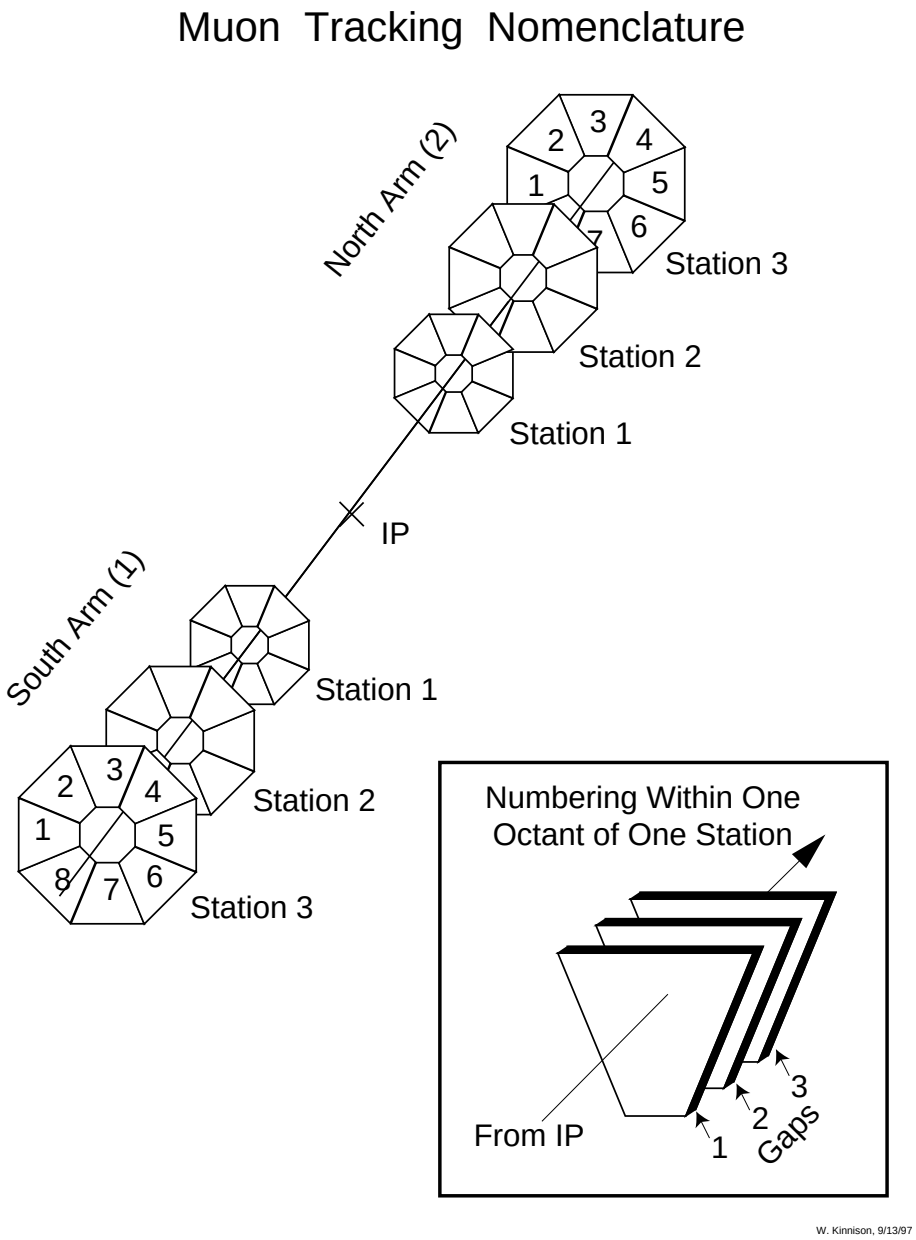

Figure 3.5: Pictorial illustration of the numbering scheme of the MuTR stations

calculated from the following formula:

$$p = q \cdot B \cdot R \tag{3.1}$$

where q is the charge of the track, B is the strength of the magnetic field, and R is the 3D-radius of the "bent" trajectory, which is determined from measuring track coordinates in all three stations.

Although the magnets between the arms are different (1.5 m shorter in the south arm), they are operated to provide a similar $\int B \cdot dl$, which is about 0.75 T·m at the 15° polar angle. The detailed information about the operational principles and performance of the PHENIX magnets can be found in [62].

3.3.2 The muon identifier detector

The main purprose of the muon identifier (MuID) is to significantly reduce the hadronic background in the muon arms. This is primarily achieved by optimizing the size, segmentation and placement of the absorber material which is the integral part of the muon spectrometers. Muons traversing through the absorber material lose a constant amount of their energy at every step, $-dE/dx$, mainly due to the ionization energy loss [38]. On the other hand, hadrons also experience strong interactions inside the absorber, which cause a complete or significant energy degradation. As a result, the intial hadron flux decreases inside the absorber depending on the penetration depth.

The placement of the multiple layers of the entire absorber material in the muon arms along the z-axis is schematically drawn on Figure 3.6. Particles produced at the IP first encounter the "nosecone" absorber situated before Station 1 of the MuTR. It is about 80 cm thick, which translates into $\sim 5\lambda_I$ of integrated nuclear interaction

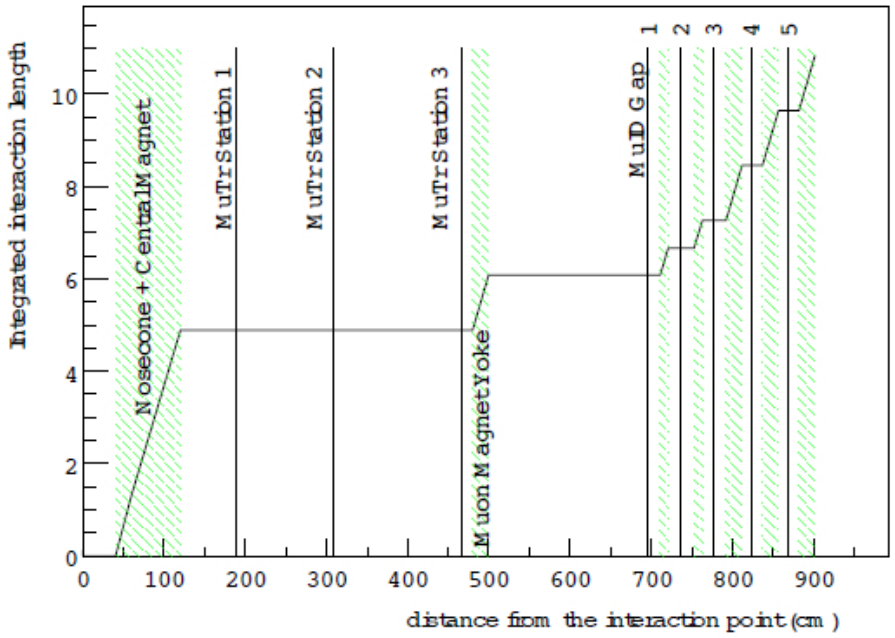

Figure 3.6: Locations of the absorbers and active layers of the muon detectors along the z-axis from the interaction point in the south arm.

length[†]. The second absorber layer, called the muon magnet backplate, is 30 cm wide in north arm and 20 cm wide in south arm and. It is located immediately after the muon tracker, and followed by the four layers of the MuID absorbers of thicknesses 10, 10, 20, 20 cm. The particular finer segmentation of the first two MuID absorbers was designed to enhance the acceptance for detecting ϕ mesons.

While the vast majority of hadrons produced at the IP are expected to be absorbed by the absorber material, there still remains an irreducible background due to weak decays into muons (μ/π ratio of 1×10^{-3}), which is fixed by the proximity of the nearest absorber. The background content will be discussed in detail in Section 4.1.1.

Five active layers, referred to as "gaps", of the MuID detector are created by the specific segmentation of the absorber. The gaps are numbered from 0 to 4 in the

[†]The nuclear interaction length, λ_I, is defined as the mean free path length required to reduce the flux of hadrons inside the absorber material by factor of e: $I = I_0 e^{-z/\lambda_I}$, with I and I_0 being reduced and initial flux, respectively.

direction away from the IP. The conventional limited steamer tubes of the Iarocci type, referred to as "Iarocci tubes", were selected as the MuID detector technology. The Iarocci tubes, illustrated in Figure 3.7, are 8.35 cm wide, 1.3 cm high, and can be up to 2 m long. Each tube is subdivided into eight 9×9 mm channels consisting of 100 μm CuBe anode wires placed inside the graphite-coated plastic cathode case.

To increase detection efficiency Iarocci tubes are paired up to form "two-packs". Tubes are fixed with a half cell offset with respect to each other. A non-flammable gas mixture of isobutane 8.5 % + CO_2 91.5 % is used inside the MuID. The Iarocci tubes are operated in the proportional mode, at 4500 V, to minimize the aging effects.

Each MuID gap is composed of six panels placed around the square hole left for the beampipe to pass through, as illustrated on Figure 3.8. Each panel consists of two layers of horizontally and vertically oriented two-packs, which provides 8.4 cm granularity along the x and y coordinates. If a traversing track deposits enough energy through the ionization energy loss in each two-pack, a "hit" will be registered. There are total number of 6140 two-packs in the MuID detectors.

3.4 Track reconstruction procedure in the muon arms

The track reconstruction procedure is performed offline. The information from the MuTR and MuID detectors that were previously recorded online are combined together to form the tracks in the muon arms. For each reconstructed track the relevant information including its vertex, kinematics, penetration depth in the MuID, etc. is determined.

The track reconstruction algorithm starts from forming "roads" in the MuID de-

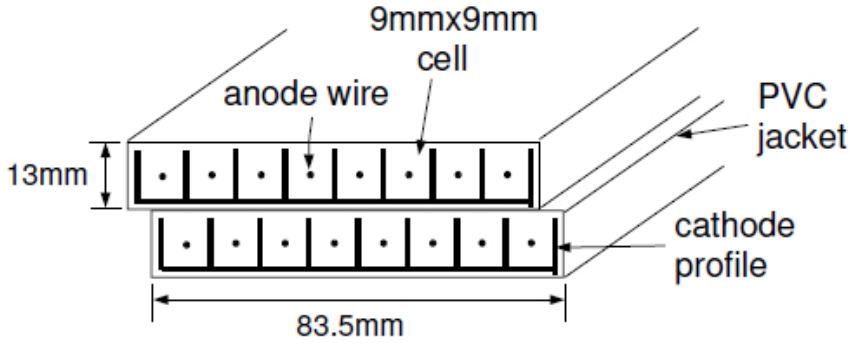

Figure 3.7: Cross section of a two-pack assembled from Iarocci tubes

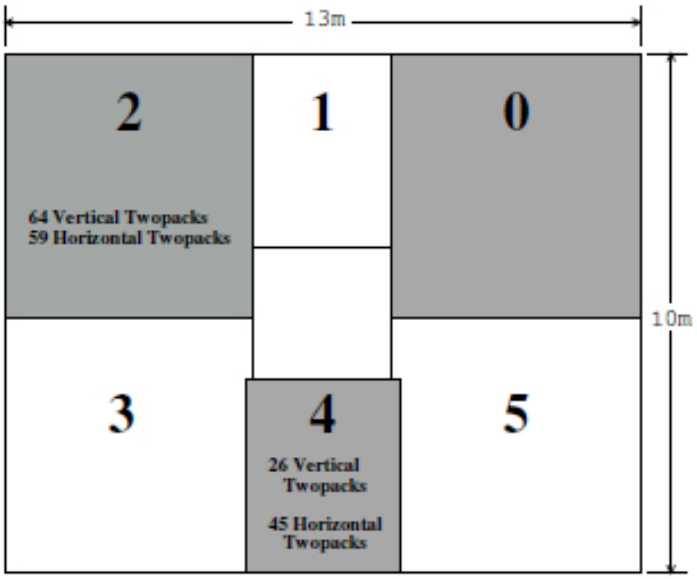

Figure 3.8: Schematic view of a MuID layer from the interaction point. The panels are numbered from 0 to 5 in the clockwise direction.

tector. As was mentioned in Section 3.3.2, in each gap two-packs are oriented in horizontal and vertical directions. The traversing track can register up to two "hits" in each MuID gap if the two-packs are fired. For each orientation one dimensional roads are formed by fitting the registered hits with the straight line. Under various constraints these roads are then merged with the roads from the opposite orientation forming the potential two dimensional roads. Only roads with the penetration depth up to at least Gap 2 are kept. Much more detailed information about the MuID road finding procedure can be found in [63].

At the next step, all possible two dimensional roads are matched with potential tracks reconstructed in the MuTR. A traversing particle can fire a maximum of three adjacent strips in each layer of a MuTR station, which are then combined to form "clusters". The layers in each station are within a distance of a few centimeters. Closely concentrated clusters are further combined to form MuTR "stubs" by a simple linear fit. Since in each layer strips are placed in two orientations, each stub essentially provides two-dimentional position information in a given station.

Once all stubs are formed, the MuTR tracking algorithm matches tracks with potential roads by selecting the closest stubs in Station 3 for each road. After a match is made, the algorithm extrapolates to the stubs in Stations 2 and 1 to form a complete track. Finally, each track is also projected through the nosecone absorber to the interaction point for determining track vertex position, momentum, etc. This also provides a check that the track originates at the collision vertex.

3.5 MinBias Trigger

The events with Cu+Cu collisions for the analyzed dataset were selected solely based on so called BBCLL1 or "MinBias" trigger. In order for an event to be selected by the MinBias trigger the following two conditions were required simultaneously:

1. At least one hit registered in each of the four BBC subdetectors.

2. The position of the event vertex along the beam axis, BBCz, reconstructed in online mode is required to be within the ±37.5 cm of the PHENIX interaction point.

3.6 The PHENIX dataflow and software framework

A detailed chart describing the flow of measured and simulated data through the all possible stages of PHENIX reconstruction software framework is shown in Figure 3.9.

As the collisions occur, only the information from the events preselected by the PHENIX triggers are recorded. The data is collected by the PHENIX Data Acqusition system (DAQ) and is written to the PHENIX Raw Data Files (PRDF) files with a typical size of 2 GB. The raw information can be further processesed either into Data Summary Tape (DST) files (1-2 GB) which contains hit information for each subsystem, or into picoDST files with track-by-track information in the muon arms.

The picoDST files were transfered to the ORNL Herans computing cluster where the analyses were perfomed. The transferred picoDST files are further filtered into more compact femtoDST files. Analysis was performed using the ROOT framework [64].

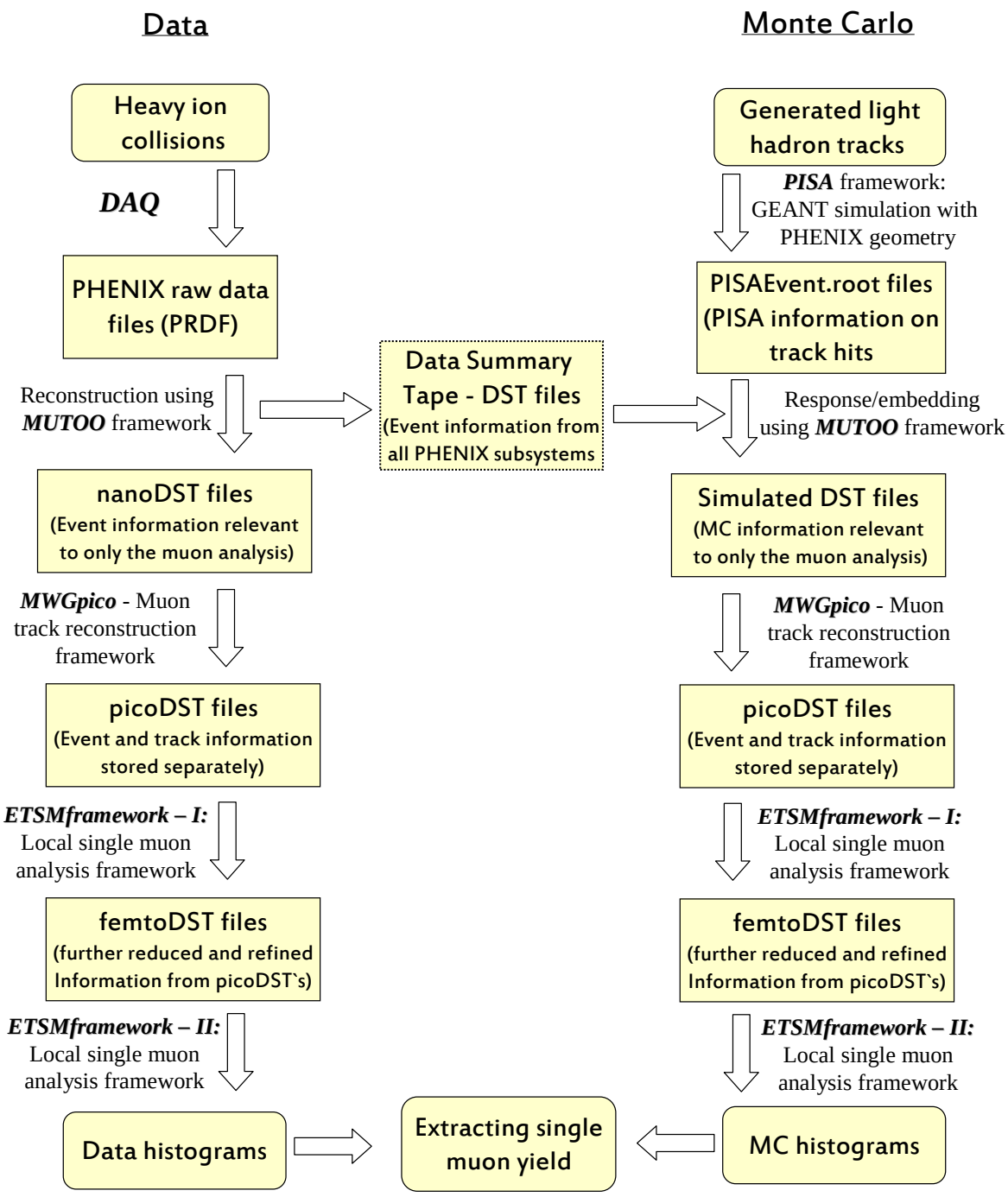

Figure 3.9: PHENIX dataflow and software framework.

Chapter 4

The single muon analysis

This dissertation presents the measurement of the negatively charged single muons resulting from the semileptonic decays of the heavy flavor mesons produced in Cu+Cu collisions at $\sqrt{s_{NN}} = 200$ GeV. The data used in this analysis were collected by the PHENIX experiment during the RHIC Run-5 period in the first quarter of 2005.

The negatively charged single muon spectra have been measured for $1.4 < |y| < 1.9$ and 1.0 GeV/c $< p_T <$ 4.0 GeV/c in three different centrality classes (0 - 20%, 20 - 40%, 40 - 94%). Furthermore, these measurements were compared to already measured single muon spectra in p+p collisions at $\sqrt{s_{NN}} = 200$ GeV to determine the nuclear modification factors for each centrality class.

The first RHIC single muon measurement was performed for p+p collisions collected during Run-2 and was based on the methodology pioneered by Youngil Kwon [65]. The current measurement is largely based on a new methodology developed by Donald Hornback for analyzing Run-5 p+p data [22].

The methods for extracting single muon spectra, determining nuclear modification factors, and calculating the corresponding systematic uncertainties are described in

detail in this chapter.

4.1 Analysis overview

All tracks reconstructed to the last layer of the MuID detector (Gap 4), are considered to be heavy flavor muon candidates. However, a large fraction of the inclusive spectra in Gap 4 is composed of tracks that originate from sources other than heavy flavor mesons. Those tracks are considered as the single muon background. Since the tracks reconstructed in the PHENIX muon arms are indistinguishable on an event-by-event basis, background must be subtracted in a statistical manner.

The heavy flavor muon signal extraction procedure is illustrated in Figure 4.1. The single muon yield (open triangles) is determined by the statistical subtraction of the background (stars), estimated by using a data driven Monte Carlo simulation of the relevant light hadron species called "Hadron Cocktail", from the inclusive spectra in Gap 4 (closed cirles). The single muon spectra are determined separately in the north and south arms, and then combined to form one spectrum as demonstrated by Figures 4.19 and 4.20.

4.1.1 Sources of tracks

The background is dominantly from light hadrons produced in between the collision vertex and nosecone absorber, and consists of two main components. The first is *Decay Muons* (DM), from the decay of light hadrons. This is the largest component, particularly at low p_T. The second component is *Punchthrough Hadrons* (PH), hadrons created at the collision vertex which pass through the entire absorber material to reach the last MuID gap. The punchtrough hadrons are more statistically significant at higher p_T.

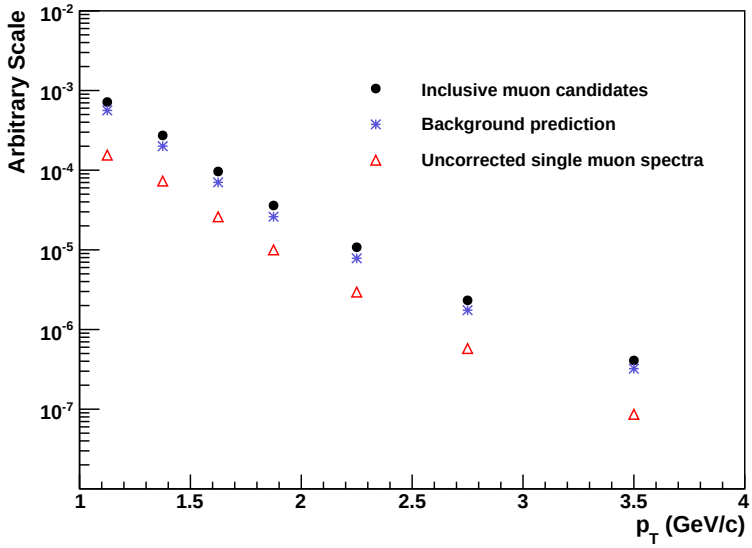

Figure 4.1: Inclusive spectrum of the muon candidates (black circles), the full background prediction (blue stars) and the resulting raw spectra of single muons (open red squares) reconstructed in the south arm are drawn as an illustration of signal extraction procedure.

Decay Muons

The majority of the particles produced at the collision point which eventually get reconstructed, either directly or through their decay products, are kaons and pions. According to the PDG, the decay into muons is, by far, the largest branching ratio for charged pions and kaons, BR($\pi^{\pm} \rightarrow \mu^{\pm}\overset{(-)}{\nu}_{\mu}$)=99.98% and BR($K^{\pm} \rightarrow \mu^{\pm}\overset{(-)}{\nu}_{\mu}$)=66%. In the laboratory frame, the average distance traveled by a particle before its decay is equal to $\gamma c\tau$. Since $(c\tau)_{\pi} = 7.8$ m and $(c\tau)_{K} = 3.71$ m, pions and kaons with $p = 2$ GeV/c has $\gamma(c\tau)_{\pi} \approx 110$ m and $\gamma(c\tau)_{K} \approx 50$ m, respectively, which on average is about two orders of magnitude larger than the distance between the IP and the nearest absorber. Therefore only a relatively small fraction pions and kaons decay before reaching the nearest absorber material. However, the contribution from this small sample of muons to the total inclusive spectra is still aproximately 2 - 3 times larger than the contribution from the signal.

Naturally, the light hadrons produced further from the absorber have a higher probability to decay into muons than those created near the absorber. The probability of the K and π-decay as a function of the distance traveled from the IP to the nearest(nosecone) absorber, Δz, can be expressed as [66]:

$$P(\Delta z) = 1 - e^{-\frac{\Delta z}{\gamma c\tau}}. \tag{4.1}$$

Using the Taylor expansion in the $\Delta z \ll \gamma c\tau$ limit, one has

$$P(\Delta z) \approx \frac{\Delta z}{\gamma c\tau}. \tag{4.2}$$

As a result, the vertex distribution of the decay muons, and thus, the entire sample of inclusive muon candidate tracks is expected to increase linearly with increasing distance from the absorber. This key feature is illustrated in Figure 4.2, which shows the normalized z-vertex distribution of the muon candidates. The slope of this distribution is proportional to the mean value of $\gamma c\tau$, and thus to the total yield of decay muons.

Punch-through hadrons

Almost all light hadrons intially produced within the kinematic acceptance of the muon arms reach the nosecone absorber. Unlike muons, hadrons can undergo strong interactions with the absorber. The initial hadronic flux decreases steeply as a function of the number of interaction lengths of the absorber material, λ_I. The more than $10\lambda_I$ of absorber material in between the IP and MuID Gap 4 ensures that only a very small fraction of light hadrons punches through the entire detector volume to be detected at the MuID Gap 4. However, even this relatively small sample of punchtrough hadrons is comparable to the number of muons from the heavy flavor decays. Unlike decay muons, the punchtrough hadrons do not have a significant

vertex dependence.

The "stopped" hadrons

Unlike particles detected in the last gap of the MuID detector, tracks that end at Gap 2 or Gap 3 are not considered to be single muon candidates. However, as will be demonstrated later on, these tracks are instrumental in correctly determining the hadronic background in Gap 4.

The fluxes of stopped particles in Gaps 2 and 3 are composed of the tracks that stop in material after their last gap, either due to range out or due to a strong interaction. This is illustrated in Figure 4.3, which shows the momentum distribution of simulated light hadron tracks that stop in Gap 3. As can be seen from the figure, the vast majority of muons, obviously resulting from the decays of simulated light hadrons, are concentrated under the peak. While most of the hadrons that did not decay into muons are reconstructed in the tail. This can be explained by the fact that muons traversing any material lose almost constant amount of energy due to ionization energy loss, $-dE/dx$, and thus require some minimum amount of energy (peak value) to reach Gap 3. In contrast, hadrons, regardless of their initial energy, may stop in the absorber after Gap 3 because of possible strong interactions. A relatively clean sample of unidentified hadrons ("stopped hadrons) can be selected by choosing tracks with momentum above the peak.

Clean identification of stopped hadrons in Gaps 2 and 3 provides a key data constraint to the hadron cocktail simulation needed for the background determination.

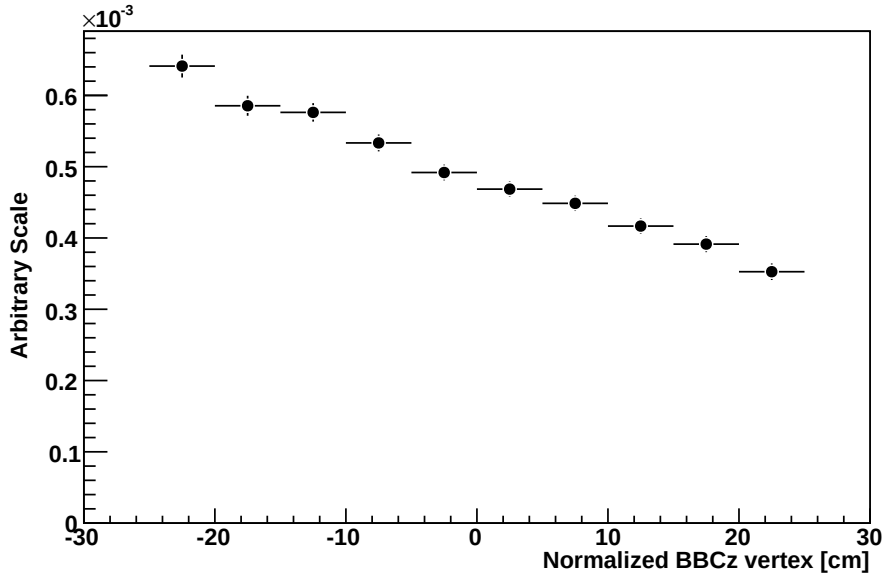

Figure 4.2: Distribution of the vertex position along the beam pipe (z-coordinate) of the muon candidate tracks in the north arm (situated in the positive z-direction) normalized with the event vertex z-coordinate distribution, BBCz.

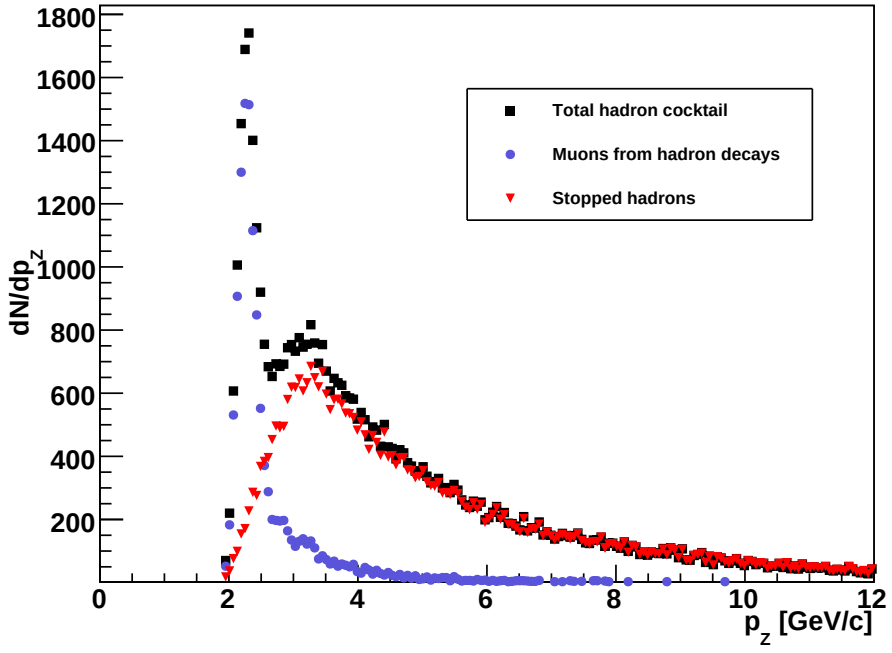

Figure 4.3: Longitudinal momentum distribution of the tracks stopping in Gap 3 from the simulation of light hadron particles.

4.1.2 Predicting background with the hadron cocktail

The need for a Monte Carlo simulation that can provide the full background prediction for the last gap of the MuID detector was essentially dictated by the unsustainably large systematic uncertainties associated with the previously attemped purely data-driven peacemeal approach, which separately measures each of the background components. Instead, the full background in gap 4 is predicted by employing the hadron cocktail, a full-scale data-constrained Monte Carlo simulation of the mixture of the relevant light hadrons, which are propagated through the simulated PHENIX detector geometry using GEANT-3 software [67].

The hadron cocktail used for extracting the present measurement is implemented through the sequence of the following four steps:

- The specific admixture of the relevant light vector mesons are generated first with the "realistic" p_T spectra in the kinematic acceptance of the muon arms.
- The generated particles are propagated through the full PHENIX detector geometry using GEANT and then reconstructed with the PHENIX muon tracking software.
- The reconstructed tracks are then embedded into the Cu+Cu data in order to reproduce the possible effects caused by the high multiplicity detector environment, known to exist during the heavy ion collisions.
- Finally, the hadron cocktail input is normalized and its p_T shape adjusted so that its prediction of stopped hadron yields in Gap 3 matches the stopped hadron yield observed for the data. Additionally, the adjusted simulation is required to simultaneously agree with the observed stopped hadron yield in Gap 2 and exactly reproduce the shape of the z-vertex distribution for the observed inclusive spectra in Gap 4.

In large part, the hadron cocktail framework used for the present analysis is similar to one used for the run 5 p+p single muon analysis[22]. However, there are several major updates and improvements specifically adapted and optimized for analysing the Cu+Cu dataset. For instance, the simulated hadron tracks were "embedded" into real Cu+Cu events to account for the detector performance in the heavy ion collision environment. This and other specifics of the background simulation framework will be discussed in detail in this chapter.

4.1.3 Summary of signal extraction procedure

The invariant single muon yield, $N_\mu(p_T)$, is measured separately for each arm. The raw yield of single muons is obtained by the procedure illustrated in Figure 4.1 and then converted to an invariant yield and corrected for detector acceptance and efficiency for the final answer. This can be specified with the following formula:

$$N_\mu(p_T) = \frac{1}{2\pi p_T}\frac{1}{dydp_T}\frac{N_{I,raw} - N_{C,raw}}{N_{MB}\cdot A\epsilon_\mu} = \frac{N_{\mu,raw}}{A\epsilon_\mu} \tag{4.3}$$

where $N_{I,raw}$, $N_{C,raw}$ and $N_{\mu,raw}$ represent raw yields of inclusive, background and single muon tracks, respectively. $A\epsilon_\mu$ and N_{MB} represent the acceptance and efficiency correction factors and the number of analyzed MinBias events.

The single muon signal extraction procedure can be outlined via the following successive steps:

1. The analysis begins by selecting the dataset to analyze. Specifically, a sample of data describing the pool of events of Cu+Cu collisions are preselected by the MinBias trigger. After initial quality assurance (QA) is performed, the total number of "good" MinBias events, N_{MB}, is determined.

2. The raw spectra of negatively charged particles in Gaps 2, 3 and 4 are deter-

mined from the total sample of tracks separately reconstructed in the North and South arms. Additionally, a cut on the longitudinal momentum is applied to tracks in Gaps 2 and 3 to select only stopped hadrons, as discussed in Section 4.1.1.

3. These selected tracks are further refined by using a set of track selection criteria, referred to as "analysis cuts", described in Section 4.2.3. The retained track yields in every gap of each arm are then transformed to raw invariant yields through the normalization with the total number of analysed MinBias events, N_{MB}, and the phase-space correction procedure, described in Section 4.2.5.

4. Multiple different versions of the hadron cocktail (the "cocktail packages") are simulated, each with a unique combination of hadron shower code (FLUKA or GHEISHA) and a specific modified value of nuclear interaction cross section for the absorber material within the GEANT framework. It is important to emphasize that the choice of shower code and the nuclear interaction cross section is the only difference between otherwise identical cocktail simulations.

5. Each hadronic cocktail package is compared to the data. Exactly the same analysis cuts are applied to the simulated tracks in Gaps 2, 3 and 4 and to the data. In each arm, the simulated flux of stopped hadrons is normalized to approximately match the data in Gap 3 first. Then the input p_T spectra of light hadrons in the cocktail simulation are modified iteratively until the simulation output matches the data over the entire p_T range in Gap 3. For each version of the cocktail simulation, the iterative tuning procedure of the input spectra is implemented separately for each muon arm which results in two slightly different input spectra. These are averaged between the arms providing one input spectrum for each cocktail version.

6. The agreement between the output of each simulation and the data is examined simultaneously in Gaps 2, 3 and 4. The simulation is required to match the

data for the stopped hadrons in the shallow gaps, and most importantly, to exactly reproduce the vertex dependence of the inclusive yield in Gap 4 caused by decay muons. This is discussed in details in Section 4.4.4.

7. For a given p_T bin, only predictions from cocktail versions that satisfy the matching criteria are considered. The Gap 4 yield prediction from only these cocktail versions are combined to form a single value, $N_C(p_T)$, representing the background for that p_T bin .

8. For each arm, the raw muon yield is calculated and corrected with the detector acceptance and efficiency.

9. As described in Section 4.5.1 the corrected muon yield calculated separately in each arm is combined to form final spectra of muons from heavy flavor decay.

Each of the above outlined steps are described in the following sections.

4.2 Initial data reduction

4.2.1 The analyzed dataset

The specifics of the collected data and initial QA

The analyzed dataset, the large collection of events Cu+Cu collisions at $\sqrt{s_{NN}} = 200$ GeV, was taken during the first part of RHIC Run-5. More than 550 total runs, corresponding to run numbers between 149539 and 160487, were recorded during this period. During initial QA procedure the following categories of runs were rejected: converter runs and runs with magnet server being down or unknown status during the run period. This information can be found at [68].

Much more detailed and precise QA, which was a starting point for the current

analysis, has been performed as a part of Run-5 Cu+Cu dimoun analysis [69]. Run selection criteria were based on the various aspects of hardware and software peformance of the muon arms during the Run-5 period. Finally, a total of 225 total "good" runs, as specified in Table C.1 were selected.

One of the most important factors that greatly affected this analysis was the reversal of the magnetic field at run 155920 which effectively split the analysed dataset into two parts (A and B). The need for separately considering these two parts of Cu+Cu data became apparent after realizing that PISA and muon reconstruction software requires the specification of a run number as an input. Since all cocktail simulations need to be performed with correct field, part B was dropped.

Centrality selection

The specified centrality is mapped to a cumulative function of BBC multiplicity. Data is calssified into three bins. For each centrality we need to know the average value of physics quantities associated with the collision geometry. These are estimated via the Glauber model as described in Appendix B. The simulated geometric quantities b, N_{coll} and N_{part} that characterize heavy ion collisions are mapped to the measured charged particle multiplicities [70].

The analyzed dataset has been categorized into the three different subsets based on the following selected centrality ranges:

1. 0 - 20 % (central)
2. 20 - 40 % (mid-central)
3. 40 - 94 % (peripheral)

It is important to note, that the particular choice of the centraility class ranges was

designed to achieve approximately matching statistical significance for each set, in addition to having sufficient statistical significance at $p_T = 4.0$ GeV/c.

Single muon spectra and nuclear modification factors for each of the above specified centrality ranges have been separately calculated.

4.2.2 Analysis variables

The measured and simulated datasets are studied using on the analysis variables. For every reconstructed track the same set of analysis variables are constructed based on the knowledge of detector geometry and relevant kinematics. The following is the list of the main analysis variables used in the single muon analysis:

- **BBCz** - The event z-vertex position measured by the BBC detector.
- **refitZ** - The z-vertex position of a track provided by the muon track reconstruction framework, taking the momentum of this track reconstructed in Station 1 of the MuTR and projecting back to the collision vertex through the nosecone absorber.
- **Number of MuTR hits** - As was described in Section 3.4, any track passing through the three stations of the MuTR can register up to 16 hits per arm.
- **refR** - The refR variable, illustrated in Figure 4.4, is the projected radial offset of the track associated MuID road at the z=0 plane. The refR variable is calculated from $\sqrt{\Delta x^2 + \Delta y^2}$, where Δx and Δy represent the separate offsets at z=0, which are obtained by extrapolating to the z=0 plane the one-dimensional slope in either x or y of the MuID road through the gap 0 hit position.

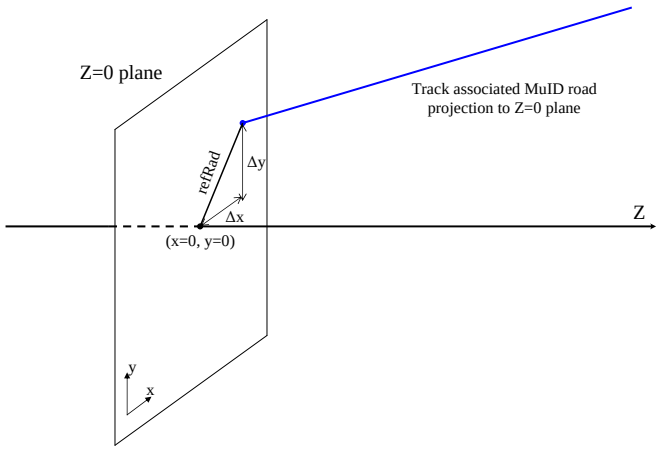

Figure 4.4: Pictorial representation of refRad variable.

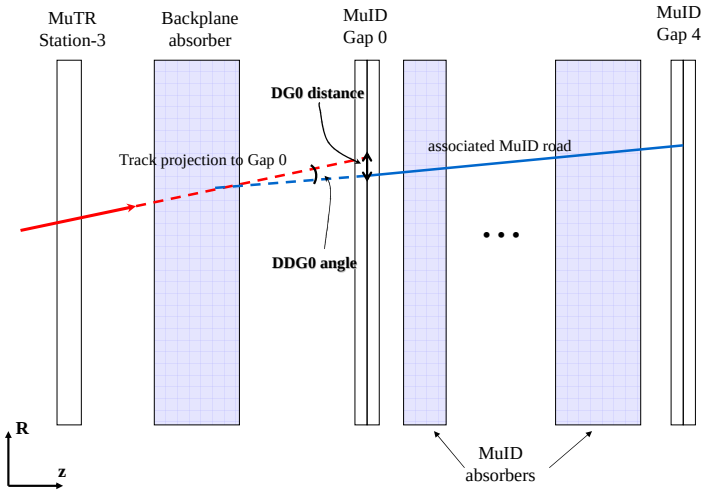

Figure 4.5: Pictorial representation of DG0 and DDG0 variables.

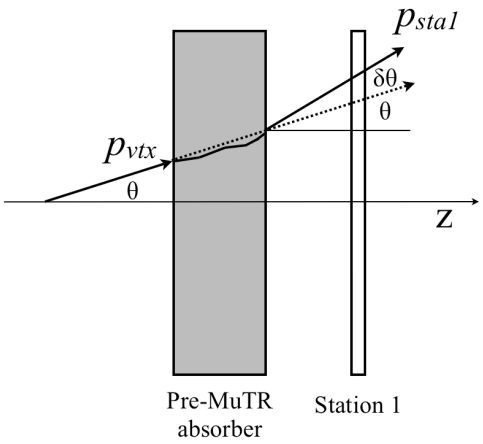

Figure 4.6: Definition of $p\delta\theta$

- **Road Slope** - MuID road slope in Gap 0, $\sqrt{\left(\frac{dx}{dz}\right)^2 + \left(\frac{dy}{dz}\right)^2}$, which is used to eliminate tracks that point to the square hole in the absorber steel and MuID gaps.

- **DG0** - The 2D-distance (in centimeters) at Gap 0 between the MuID road projection and the MuTR track projection from Station 3, as illustrated in Figure 4.5.

- **DDG0** - The angle (in degrees) between the MuTR track projection vector from Station 3 and the MuID road projection vector, also illustrated in Figure 4.5.

- $p\delta\theta$ - The scattering angle of the track in the nosecone absorber, $\delta\theta$, scaled by the average of the momentum magnitude at the vertex and at Station 1, $\bar{p} = \frac{p_{vtx} + p_{sta1}}{2}$.

  The $\delta\theta$ angle, illustrated in Figure 4.6, can be calculated from the following:

$$\delta\theta = cos^{-1}\left(\frac{\overrightarrow{p}_{vtx} \cdot \overrightarrow{p}_{Sta1}}{|\overrightarrow{p}_{vtx}| \cdot |\overrightarrow{p}_{Sta1}|}\right). \tag{4.4}$$

  The quantity $\overrightarrow{p}_{Sta1}$ is the momentum vector measured at Station 1, whereas,

$\overrightarrow{p}_{vtx}$ is the momentum vector at the event vertex estimated by the tracking algorithm. For a given track, the $\delta\theta$ angle essentially measures the extent of deflection due to multiple scattering and radiative energy loss ocurring in the nosecone absorber. The angular deflection of a track in the absorber is expected to be inversely proportional to the momentum. Therefore scaling the scattering angle by the total momentum ensures, in principle, that the total distribution, $p\delta\theta$, remains approximately a Gaussian with constant width in all p_T bins.

- $\delta\mathbf{Z}$ - The difference between the event vertex reconstructed by the BBC and the vertex reconstructed from the muon reconstruction code, $\delta Z = BBCz - refitZ$. As shown in the recent single muon analysis [22], those tracks which show large differences between the event z-vertex and the track fit vertex correlate strongly with those tracks exhibiting pathologically large $p\delta\theta$ values.

4.2.3 Analysis cuts

Analysis cuts for muon candidate tracks

The initial inclusive sample of tracks reconstructed in Gap 4 can be further refined using the track quality selection criteria, called analysis cuts, based on the distributions of the analysis variables introduced above. The main idea behind applying these cuts is to reduce or eliminate the tracks with unphysical or defective kinematic variable values, most likely originating from the different types of background, poor reconstruction, or tracks with strong interactions, without affecting the muon tracks from the heavy flavor decay, at the same time. As a result, the reduction in the total inclusive flux of muon candidates, mostly at the expense of tracks coming from background sources, increases the signal to background ratio.

The analysis cuts for the inclusive tracks reconstructed in Gap 4 are optimized using

the simulation of the single muon tracks*, which are then embedded into the Cu+Cu data to reproduce the possible effects caused by the high occupancy environment expected to exist during the heavy ion collisions. It also turns out that distributions of the analysis variables differ from each other depending on the p_T of a given track, therefore, they need to be examined as a function of p_T.

Once the analysis cuts are established, they are applied to both the measured and simulated inclusive spectra in Gap 4 in the same manner. An example of typical cut values used are illustrated in Figure 4.1.

Analysis cuts for stopped hadrons

As has been already discussed, the comparison between the data and simulation in the shallow MuID gaps is a key part of the analysis. Therefore, extra care needs to be taken when dealing with the stopped hadron tracks reconstructed in Gaps 2 and 3. Also cuts are expected to be different because the stopped hadron yields could include hadrons that may have interacted in the steel.

Although the embedded simulation generally does a good job of reproducing the data, the comparison for various kinematic distributions reveals that some non-negligible differences between MC and data still remain. This is illustrated in Figure 4.7 where the DG0 distributions for the data and MC are drawn separately in each p_T bin. As can be seen from the figure, the DG0-distributions for the data tends to be slightly wider than those for the simulation. It turns out that these differences also depend on the centrality selection and the choice of the hadron shower code (FLUKA and GHEISHA) within GEANT [67].

*Indeed, in the previous single muon analysis, the cut values were initially established using a known heavy heavy flavor muon sample, such as measured J/ψ particles from the Run 5 data. While this approach is limited to the low p_T region, it also turned out that single muon simulation very closely reproduces the measurement.

Table 4.1: A selection criteria for inclusive negatively charged tracks reconstructed with the p_T between 1.0 GeV/c and 1.25 GeV/c, in Gap 4. Values in brackets represent the corresponding cut values for the south arm.

Cut #	Variable	Cut description
1.	*bbcZ* & *refitZ*	Event $\|bbcZ\| < 25$ cm Track $\|refitZ\| < 25$ cm
2.	*DG0*	DG0 $< 15(20)$ cm
3.	*DDG0*	DDG0 $< 10(9)^\circ$
4.	*refRad*	refRad $< 100(120)$ cm
5.	*Road Slope*	Road Slope > 0.2
6.	$p\delta\theta$	$p\delta\theta < 0.2$ GeV·rad/c
7.	δZ	$\delta Z < 2$ cm
8.	*bbcZ* & *refitZ*	"Nearside" Z cut: 0 cm $< bbcZ$ & $refitZ < 25$ cm (-25 cm $< bbcZ$ & $refitZ < 0$ cm) (Applied to the inclusive sample of single muon candidates to increase S/B ratio by reducing the relative fraction of decay muons.)

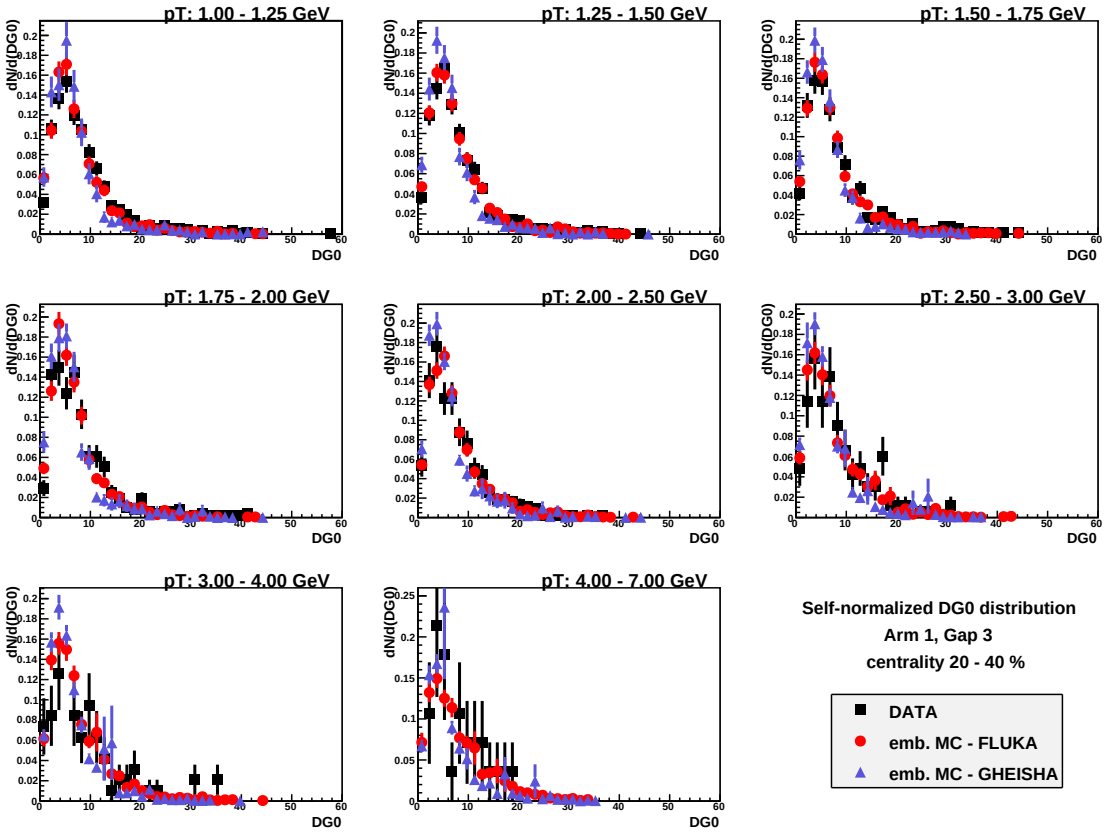

Figure 4.7: Comparison of data and simulation for self-normalized distribution of DG0 variable in each p_T bin.

Using the same approach as for the muon candidate tracks in Gap 4, i.e applying exactly the same cut values for tracks reconstructed in the shallower MuID gaps for both data and MC, will lead to a biased result in the relative comparison of stopped hadron fluxes. Differences are magnified by the relatively small signal to background ratio. Instead, a different approach has been used.

For a given p_T bin, separately for the data and the simulations, the cumulative distributions for each analysis variable have been constructed using the following ansatz:

$$f(X) = \int_0^X \frac{dN}{dX} dX \tag{4.5}$$

as illustrated in Figure 4.8 for DG0. In each case, a value of the considered variable (DG0) for which the corresponding cumulative function, $f(DG0)$, is equal to 0.97 is determined and then selected as the corresponding analysis cut value for this distribution. This approach essentially leads to the three different analysis cut values in each analyzed p_T bin corresponding to the data and simulations with the different hadron shower codes.

This procedure is also carried out for the other kinematic variables.

Restricting geometric acceptance

Assessing the matching between the data and MC is extremely important, since any possible difference in matching between the data and simulation are direct sources of systematic uncertainties of the background prediction.

A given Monte Carlo simulation of hadron tracks in the muon arms is not always expected to perfectly reproduce the data in every part of the detector. The main reason for this is that the simulation does not completely reflect the hardware conditions in all parts of the detector, which may change during the months of the data-taking

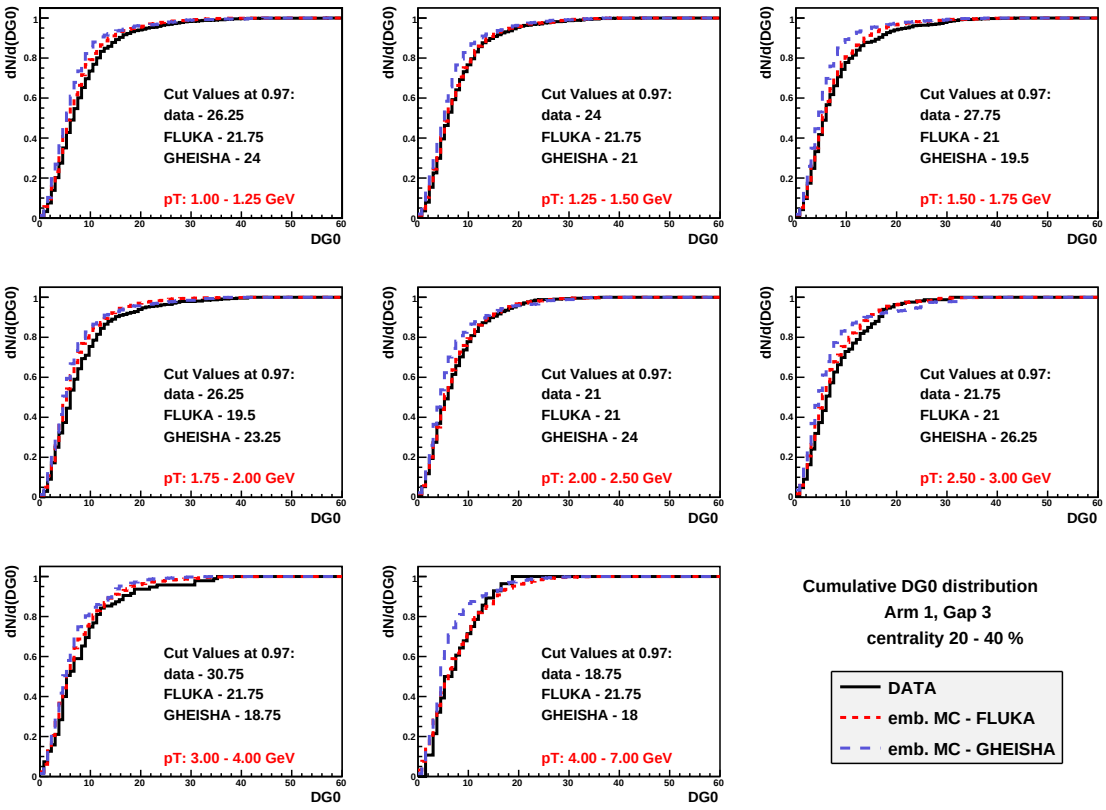

Figure 4.8: Comparison of data and simulation for the corresponding cumulative distribution, $f(DG0)$, calculated using Equation 4.5 for each p_T bin.

period. Therefore it is extremely important to carefully identify and examine the specific detector areas where the simulation produces different output as compared to the data.

To improve the overall matching between the Monte Carlo simulations and the data, tracks that traverse the detector in the "problematic" areas are eliminated. This is done by scrutinizing hit densities for the tracks reconstructed in the muon arms. Initially x vs.y radiographs in the MuID are visually checked. After eliminating the areas with obvious mismatch between the MC and data, one dimensional histograms of radial and azimuthal hit densities in the MuTR are examined by using chi-square per degree of freedom comparison criteria. All possible mismatches are eliminated on a bin-by-bin basis.

Figures 4.9 and 4.10 illustrate examples of two separate comparisons between the MC and data (FLUKA vs. data and GHEISHA vs. data) for ϕ-distributions of hits registered in Station 1 of the MuTR after eliminating bins with large disagreements. In both cases, the data and MC exhibit excellent agreement which further increases confidence in the hadron cocktail prediction.

4.2.4 Estimating combinatoric background using $p\delta\theta$ and δZ variables

As discussed in Section 4.2.2, the $p\delta\theta$ distributions for tracks that originate from the real physics signal are expected to follow a Gaussian-like distribution with a constant width for every p_T bin. The $p\delta\theta < 0.2$ selection criteria ensures that the majority of the tracks with misreconstructed momentum are eliminated from the total sample of reconstructed tracks. However, some background may remain "underneath" the Gaussian peak of the $p\delta\theta$ distribution. While the fraction of such background is pretty small in the low p_T region, it is expected to become significant at the higher

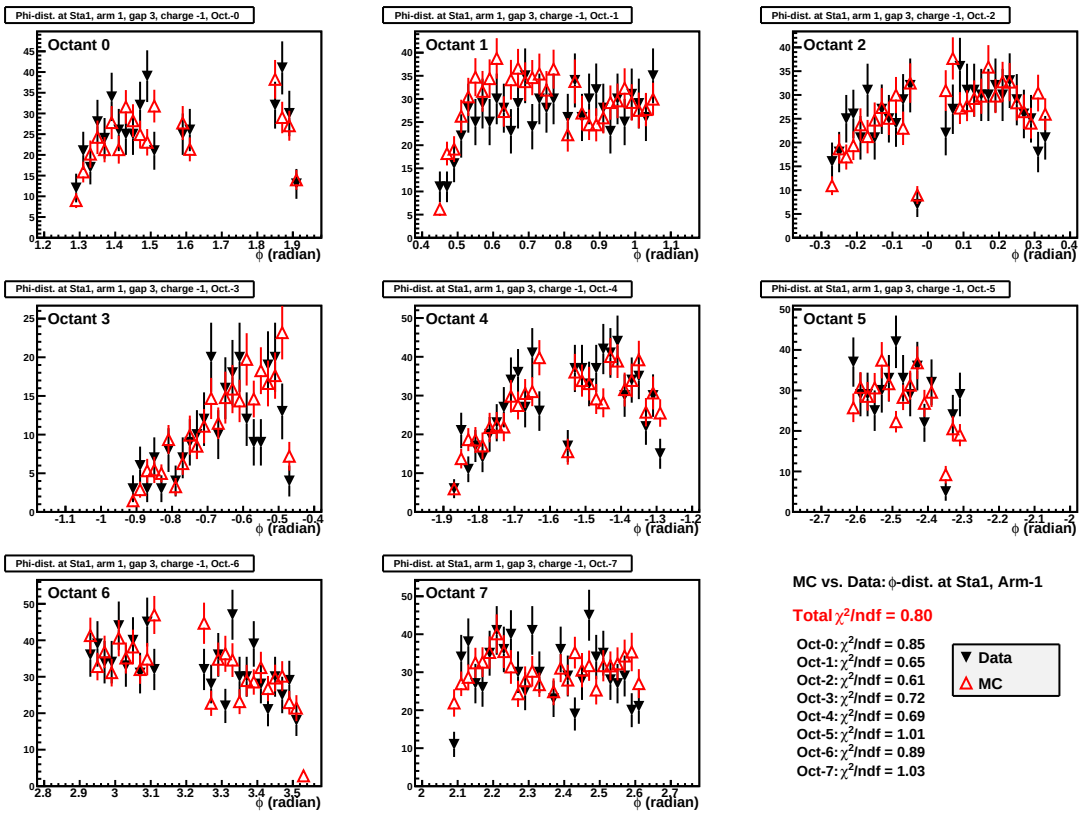

Figure 4.9: Comparison of MC(FLUKA) to data for the $\phi-$distributions for all eight octants of Station 1 of the MuTR.

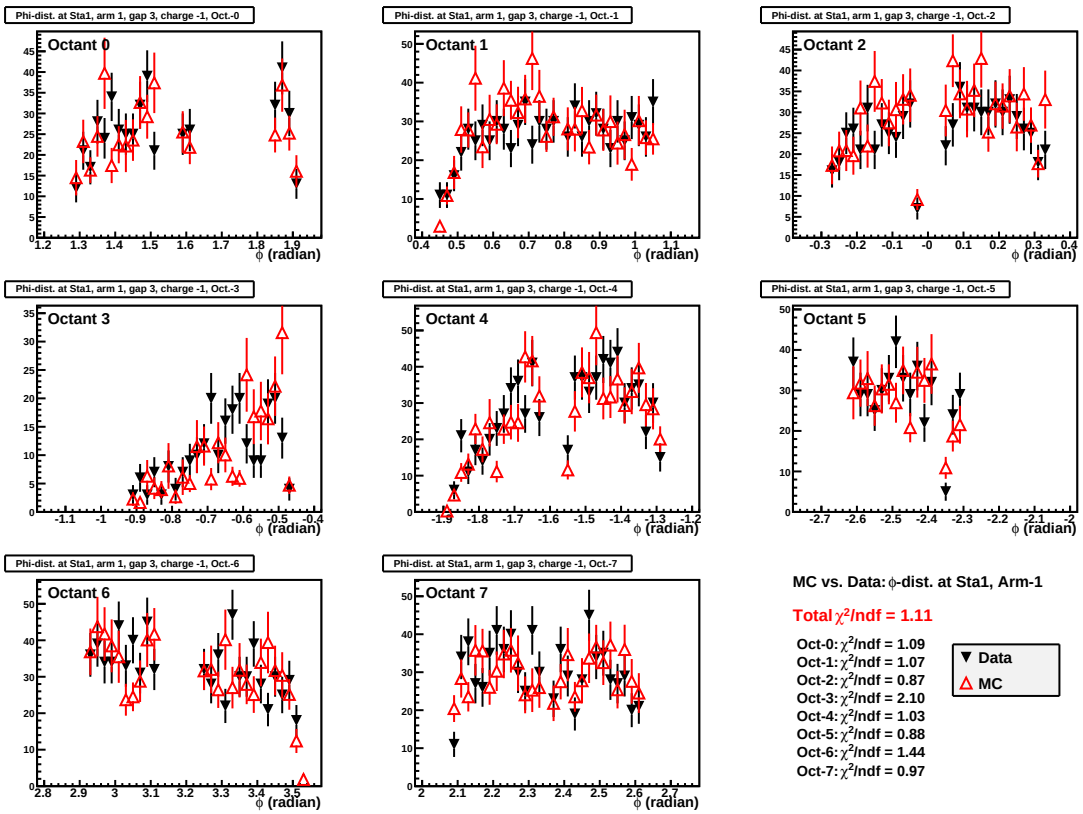

Figure 4.10: Comparison of the MC(GHEISHA) to data for the $\phi-$distributions for all eight octants of Station 1 of the MuTR.

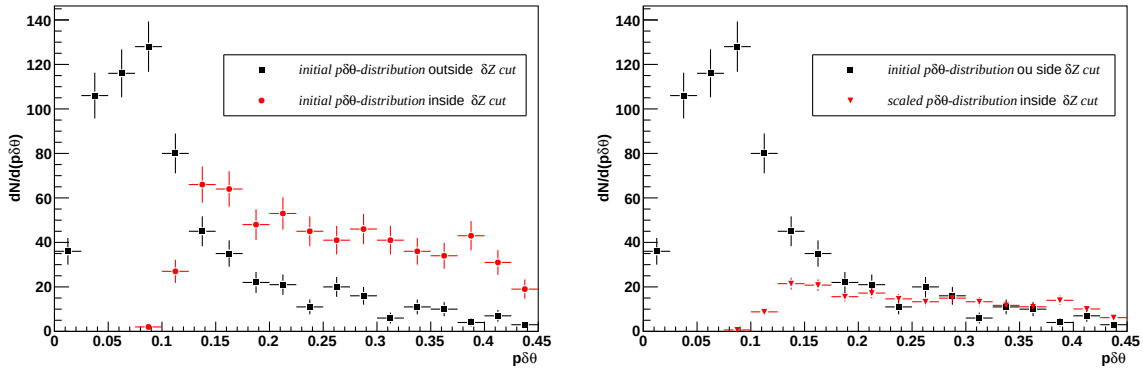

Figure 4.11: Representative $p\delta\theta$ distributions for stopped hadrons reconstructed in Gap 3 of the north arm for the transverse momentum range 2.5 to 3.0 GeV/c]. The left plot compares the raw distribution for $\delta Z < 2$ cm with the raw distribution for $\delta Z > 2$ cm. The right plot compares the same initial distribution for $\delta Z < 2$ cm with the intial distribution for $\delta Z > 2$ cm scaled to match the tail of the $p\delta\theta$ distribution for $\delta Z < 2$ cm.

p_T. Therefore, it is important to estimate the constribution from this background.

Generally, the structure of the combinatoric background underneath the signal is very hard to estimate, since it does not follow a simple, or even a single, physics principle. However, a correlation analysis between the $p\delta\theta$ and δZ variables revealed that, indeed, the combinatorial background for the reconstructed tracks in the muon arms has a specific structure. This is illustrated in Figure 4.11 which compares the $p\delta\theta$-distributions for tracks falling inside the $|\delta Z| < 2$ cm cut to the $p\delta\theta$-distributions of tracks with $|\delta Z| > 2$ cm. It turns out that the $p\delta\theta$-distribution for the latter exhibit an identical pattern across the entire p_T range.

Therefore, to estimate the background contribution for each p_T bin, the yield of particles reconstructed outside the δZ-cut is scaled to match the non-Gaussian "tail" of the $p\delta\theta$ distributions for the tracks reconstructed inside the δZ-cut, as shown in Figure 4.11. Finally, the background extrapolated underneath the peak is subtracted from the overall yield.

4.2.5 Invariant yields

After applying all analysis cuts and subtracting the estimated contribution of the combinatoric background, the remaining part of the reconstructed raw data yields for each gap are converted to the invariant yields using the following formula:

$$N_x(p_T) \equiv \frac{1}{N_{MB}} \frac{1}{2\pi p_T} \frac{dN_x(p_T)}{dy dp_T} \tag{4.6}$$

where N_{MB} serves as a normalization factor, representing the total number of analyzed MinBias events. The quantities dy and dp_T represent the analyzed rapidity and p_T bin width, respectively. It is important to note that these yields are not yet corrected for detector acceptance and efficiency.

The simulated hadron yields in all gaps are normalized and adjusted to match the corresponding invariant data yields, which is essentially equivalent to the above described procedure.

4.3 Acceptance and efficiency corrections

The sample of the reconstructed single muons is only a fraction of the heavy flavor muons within the kinematic reach of the muon arms, largely as a result of the application of the analysis cuts and limiting the geometric acceptance. Additionally, the track reconstruction efficiency is affected by the muon detector performance during the dataking period. Therefore, at the final stage of the analysis, the "uncorrected" spectra of single muons needs to be corrected with the appropriate acceptance×efficiency factors ($A\epsilon_\mu$).

Since the spectra remaining after the statistical subtraction of the final background prediction are considered to be completely composed of heavy flavor muons, simula-

tions starting exclusively from muon tracks have been employed to calculate Aϵ_μ's.

For simulating single muons in the PHENIX muon arms, a Monte Carlo framework very similar to the hadron cocktail has been implemented. Initially, single muon tracks are generated following the "realistic" p_T shape and flat z-vertex position over the rapidity range of $1.1 \leq| \ y \ |\leq 2.1$ (wider than the analyzed rapidity interval $1.4 \leq| \ y \ |\leq 1.9$), to account for the possible effects due to finite detector resolution[†]. To cover the entire kinematic range of interest, single muons tracks are initially generated in the p_T interval of 0.8 GeV/c - 10.0 GeV/c. To achieve sufficient statistics at higher p_T bins, separate simulations are performed in which muons are thrown with exactly the same shape but with the initial p_T near the low end of the analyzed bin. As in the case of the hadron cocktail simulation, the simulated single muon tracks have been embedded into the Cu+Cu data to simulate the possible effects for the track reconstruction inefficiency caused by the detector occupancy for collisions of different centrality.

In principle, the Acceptance×Efficiency for reconstructing a given muon track also depends on its kinematics. Therefore, the correction factors, Aϵ_μ, must be separately calculated for each selected centrality class, for each combination of p_T bin and z-vertex position. The Acceptance×Efficiency for a given centrality class is defined as:

$$A\epsilon_\mu(\Delta p_T, \Delta z) = \frac{N_{reco}(\Delta p_T, \Delta z)}{N_{thrown}(\Delta p_T, \Delta z)} \tag{4.7}$$

where $N_{thrown}(p_T, \Delta z)$ is the total number of the single muon tracks originally generated (thrown) within the given Δp_T bin and Δz position interval. The numerator, $N_{reco}(\Delta p_T, \Delta z)$, represents the total number of simulated muon tracks reconstructed after passing through the full set of the analysis cuts.

The simulated Acceptance×Efficiency corrections as a function of z-vertex, calculated

[†]These ("bleed-over") effects have been extensively explored by Donald Hornback in his dissertation[22].

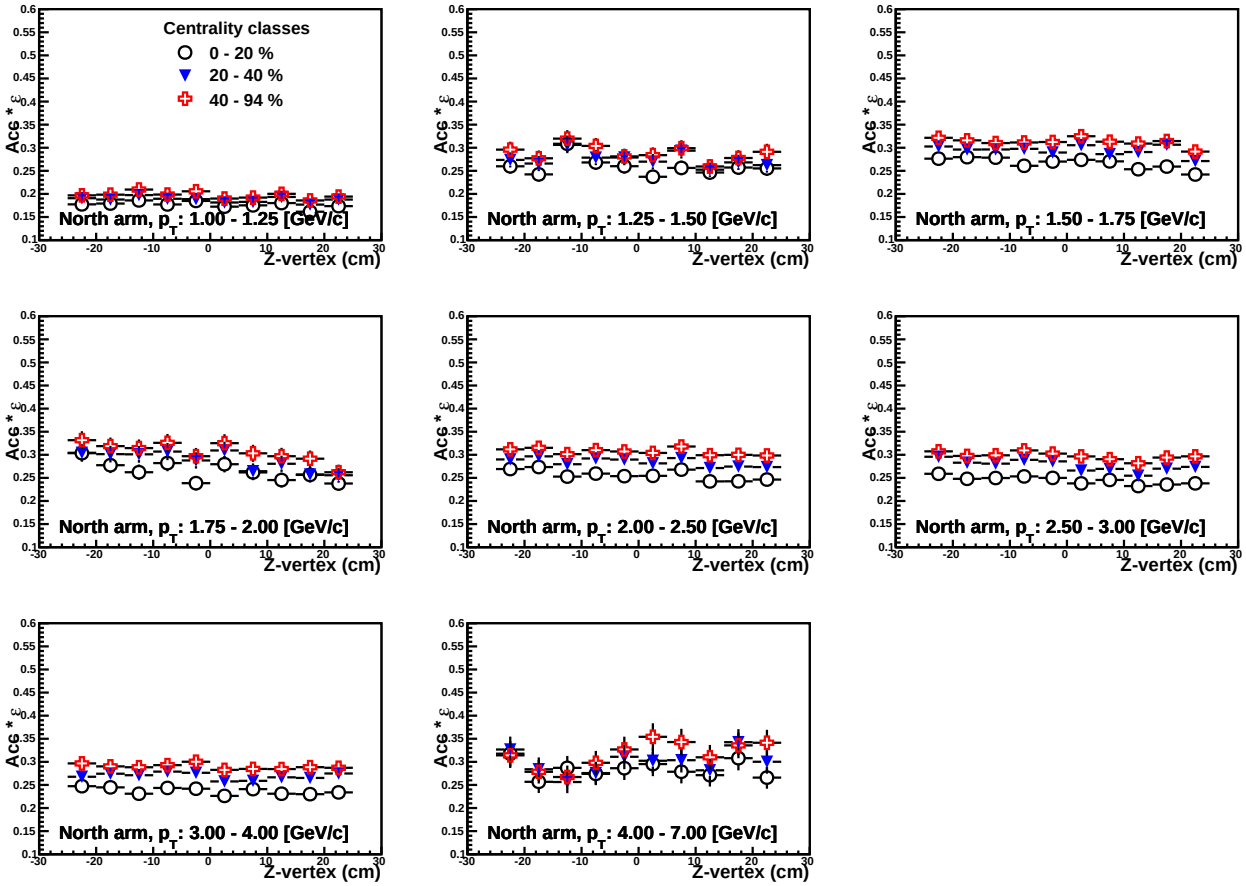

Figure 4.12: BBC z-vertex dependence of acceptance×efficiency correction for all centrality ranges for individual p_T bins (North arm).

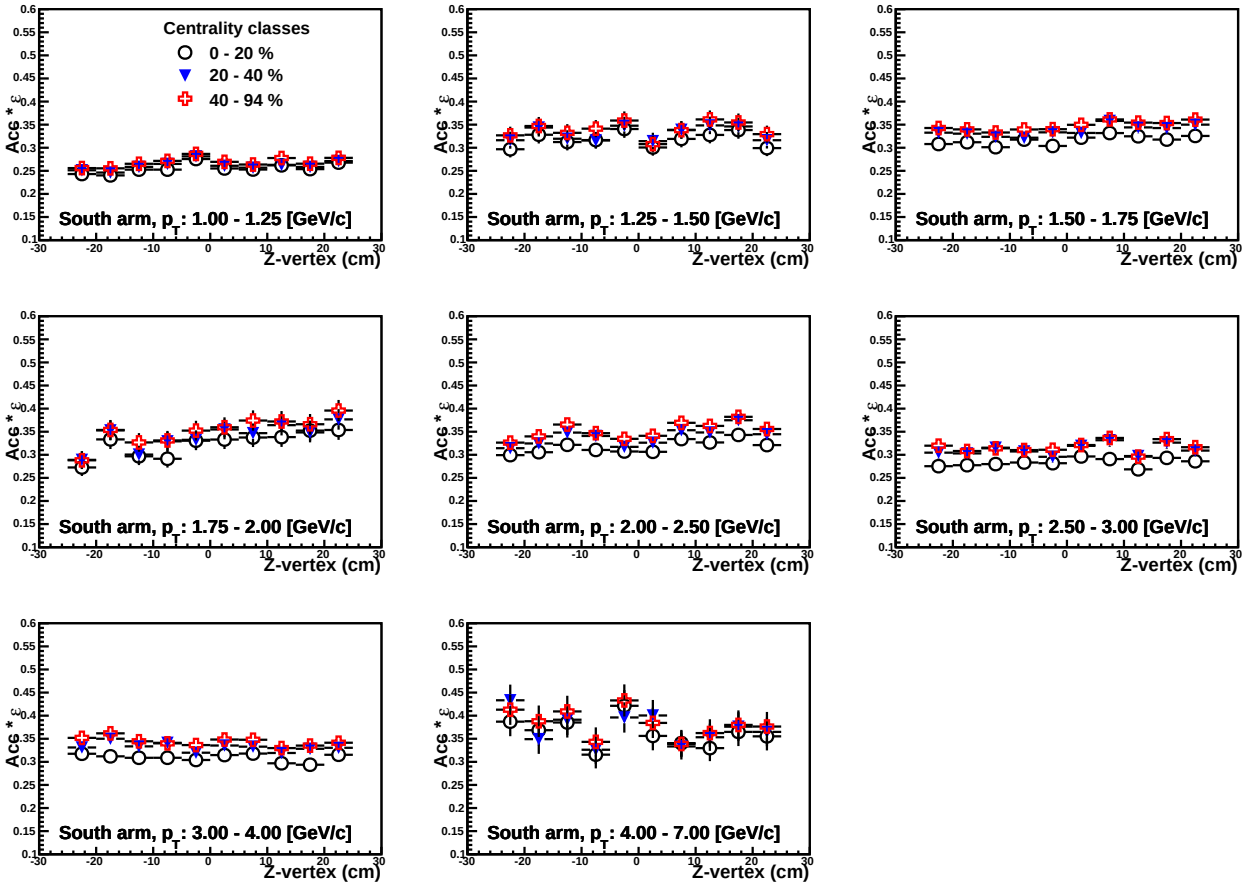

Figure 4.13: BBC Z-vertex dependence of acceptance*efficiency correction for all centrality ranges for individual p_T bins (South arm).

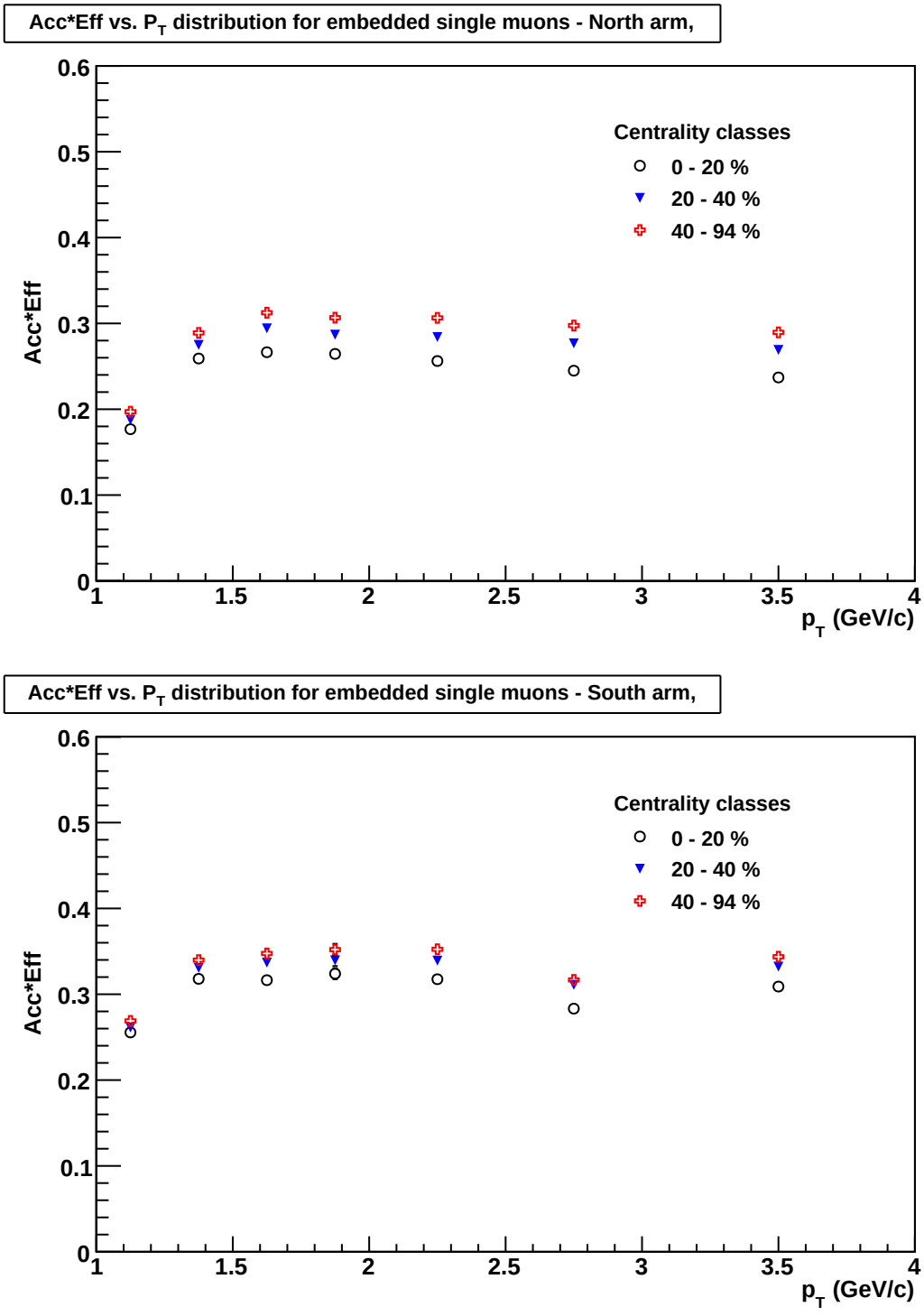

Figure 4.14: Acceptance×Efficiency correction factors (averaged over z-vertex) as a function of p_T for all centrality ranges: North arm (upper) and south arm (lower).

separately for each centrality class, arm and p_T bin, are shown in Figures 4.12 and 4.13. As can be seen from the figures, there is essentially no significant (at most 15 %) vertex dependence for the Aϵ_μ factors. Therefore, the Acceptance×Efficiency corrections can be applied as a function of p_T alone. Figure 4.14 shows the simulated Acceptance×Efficiency corrections drawn as a function of p_T for each centrality class. The results clearly illustrate a significant centrality dependence in the reconstruction efficiency, as expected.

4.4 Monte Carlo simulation of the background

The hadron cocktail, a Monte Carlo simulation of the light hadron background in the muon arms is the key element of the presented analysis. This section describes in detail the hadron cocktail framework and how it is utilized to determined the background.

4.4.1 Generating cocktail input

First, p_T (spectra) distributions of $\pi^\pm, K^\pm, p, \bar{p}, K^0_L, K^0_S$ particles are generated as the input for further processing through the GEANT simulation. Ideally these have already been measured so they can be directly utilized for generating the hadron cocktail. Unfortunately, the spectra of light hadrons in p+p or Cu+Cu collisions at $\sqrt{s_{NN}}$ = 200 GeV have not been measured at $1.4 < |y| < 1.9$[‡]. Therefore the PHENIX measurement of π^0 spectrum at $y \sim 0$ in $p+p$ collisions has been selected as a starting point. Since the spectrum was measured as an invariant cross section,

[‡]At the Quark Matter conference in Knoxville in March/April 2009, the BRAHMS collaboration presented a small portion of preliminary approved data of the identified light hadron spectra at different rapidities

it needs to be converted to particle yields:

$$f(p_T, y) \equiv \frac{d^2N}{dp_T dy} = N_0 2\pi p_T E \frac{d^3N}{dp^3} \tag{4.8}$$

where N_0 is a normalization factor. In order to extrapolate to forward rapidity a Gaussian rapidity evolution is used [71], so that Equation 4.8 can be rewritten as the following:

$$f(p_T, y) = f(p_T, 0) \cdot \exp^{-\frac{y^2}{2\sigma_y^2}} \tag{4.9}$$

where σ_y^2 is the standard deviation of the rapidity evolution (dN/dy vs. y) for the production of pions measured in p+p collisions at $\sqrt{s_{NN}} = 200$ GeV, estimated to be about 2.25[71]. The π^0 spectrum is extrapolated to seven rapidity bins within the [1.0 - 2.4] interval, with width $\Delta y = 0.2$.

Once the pion distributions are constructed, the K/π ratio is used to determine the input distributions for kaons. The K/π ratio as a function of p_T was constructed from combined STAR and PHENIX measurements of pions and $K^{\pm}$'s ,K_S^0's [72]. In the present framework it is assumed that K/π ratio is approximately the same for p+p and Cu+Cu collisions [71].

4.4.2 Altering hadronic shower code

The generated light hadron particles are propagated through the PHENIX geometry using GEANT 3 simulation software [67]. The number of hadrons reaching Gaps 2, 3 and 4 in the simulation mostly depends on the specifics of the hadron track propagation through the absorber material. In GEANT, this is implemented through the hadron shower code, which models the physics of strong interaction that the hadron tracks undergo while traversing the absorber material. GHEISHA and FLUKA, two different models within the GEANT framework, have been used in this

analysis providing a better assessment of the model dependent systematics.

However, as has already observed in the previous single muon analyses, the GEANT simulations using either GHEISHA or FLUKA default settings do not simultaneously and satisfactorally reproduce the measured hadronic fluxes for all MuID gaps. Therefore, both hadron shower codes are separately modified until an adequate agreement is achieved. This is done by altering the default nuclear interaction cross section for the absorber material. Specifically, the cross section is scaled up (FLUKA) or down (GHEISHA) by several percent.

Indeed, the particular choice of the shower code and nuclear interaction cross section for the absorber material defines the uniqueness of a given hadron cocktail simulation, which will be referred as a "cocktail package" here. The cocktail packages are otherwise (initial input and embedding procedure) identical. The following cocktail packages were used in the analysis: (1) FL105, (2) FL106, (3) FL107, (4) GH92 and (5) GH93. Each package is abbreviated by combining the first two letters of shower code name and percentage (in integer numbers) scaling of the nuclear interaction cross section. Each package represents a simulation of approximately 10^{10} hadrons.

4.4.3 "Tuning" cocktail to match the data

Each cocktail package is adjusted to match data in Gap 3 by modifying the shape of thrown p_T spectra. This is implemented by applying specific weights to the reconstructed tracks based on their "thrown" (initially generated) p_T values[§].

These weights are determined separately for each arm and on a p_T bin by p_T bin basis. This is done by comparing the simulated yield of the stopped hadrons in Gap 3 to the data. The simulated stopped hadron spectra are first normalized to

[§]This procedure is mathematically equivalent to simulating (from scratch) a new hadron cocktail with the modified input spectra, which requires at least several weeks of computing.

approximately match the data accross the entire p_T range. The initial set of weights are calculated from the simple MC/data ratios for all p_T bins:

$$\omega_0(p_T) = \frac{N_3^0(p_T)}{N_3^{data}(p_T)} \tag{4.10}$$

where N_3^{data} represents the measured invariant yield of stopped hadrons. $N_3^0(p_T)$ represents the simulated stopped hadron yield normalized to match data.

The initially calculated weights, $\omega_0(p_T)$, are then simultaneously applied to the tracks reconstructed by the simulation in Gaps 2, 3 and 4 based on the thrown p_T. After weighting, the output of the cocktail package is again compared to the data in Gap 3.

Usually applying the initially determined set of weights is not sufficient for the simulation to match data simultaneously in all p_T bins. Therefore, this procedure is iteratively repeated until the MC/data ratio becomes unity across the entire p_T range:

$$\omega_n(p_T) = \frac{N_3^n(p_T)}{N_3^{data}(p_T)} = 1 \tag{4.11}$$

where $N_3^n(p_T)$ represents the simulation output after the n-th iteration needed to achieve the simultaneous matching for all p_T bins.

Since the tuning procedure is performed separately for each arm, it results in two different input spectra. These spectra are then combined to form the final common cocktail input. This is done by first calculating the combined set of weights, $\omega_{comb}(p_T)$, with the following:

$$\omega_{comb}(p_T) = \frac{\omega_n^N(p_T) + \omega_m^S(p_T)}{2} \tag{4.12}$$

where $\omega_n^N(p_T)$ and $\omega_m^S(p_T)$ represent the weights after the final iterations in the north and south arm, respectively.

Finally, the input spectra are modified one last time by simultaneously applying the combined set of weights determined from Equation 4.12. The comparison between the data and the FL106 cocktail package output tuned with combined set of weights for the stopped hadron yields in Gap 2 and 3 is illustrated in Figure 4.15.

4.4.4 The "successful" matching criteria

The tuning procedure described in the previous section is performed for each simulated cocktail package. The prediction of each cocktail package is compared to data in Gaps 2, 3, and 4. For each p_T bin, the degree of agreement between the data and simulation is determined based on the following two factors:

1. The agreement of the stopped hadron yields in Gaps 2 and 3, which essentially is evaluated based on the percentage difference between the data and simulation. This difference is also folded into systematic uncertainties.

2. The agreement of the z-vertex slopes of the inclusive yields in Gap 4, illustrated in Figure 4.16, is evaluated using the χ^2/NDF criteria. The χ^2 for each p_T bin is calculated through the following formula:

$$\chi^2_{Gap4}(p_T) = \sum_{i=1}^{Nzbins} \frac{(\Delta z_i - \overline{\Delta z})^2}{\sigma_i^2 + \sigma_{mean}^2} \tag{4.13}$$

   where $\Delta z_i = z_i^{data} - z_i^{MC}$ is the z-vertex difference between the data and simulation for i-th bin. The quantity $\overline{\Delta z}$ represents the z-vertex difference averaged over Nzbins, the total number of bins within the z-vertex distribution. The variables σ_i and σ_{mean} represent the uncertainties corresponding to Δz_i and $\overline{\Delta z}$, respectively.

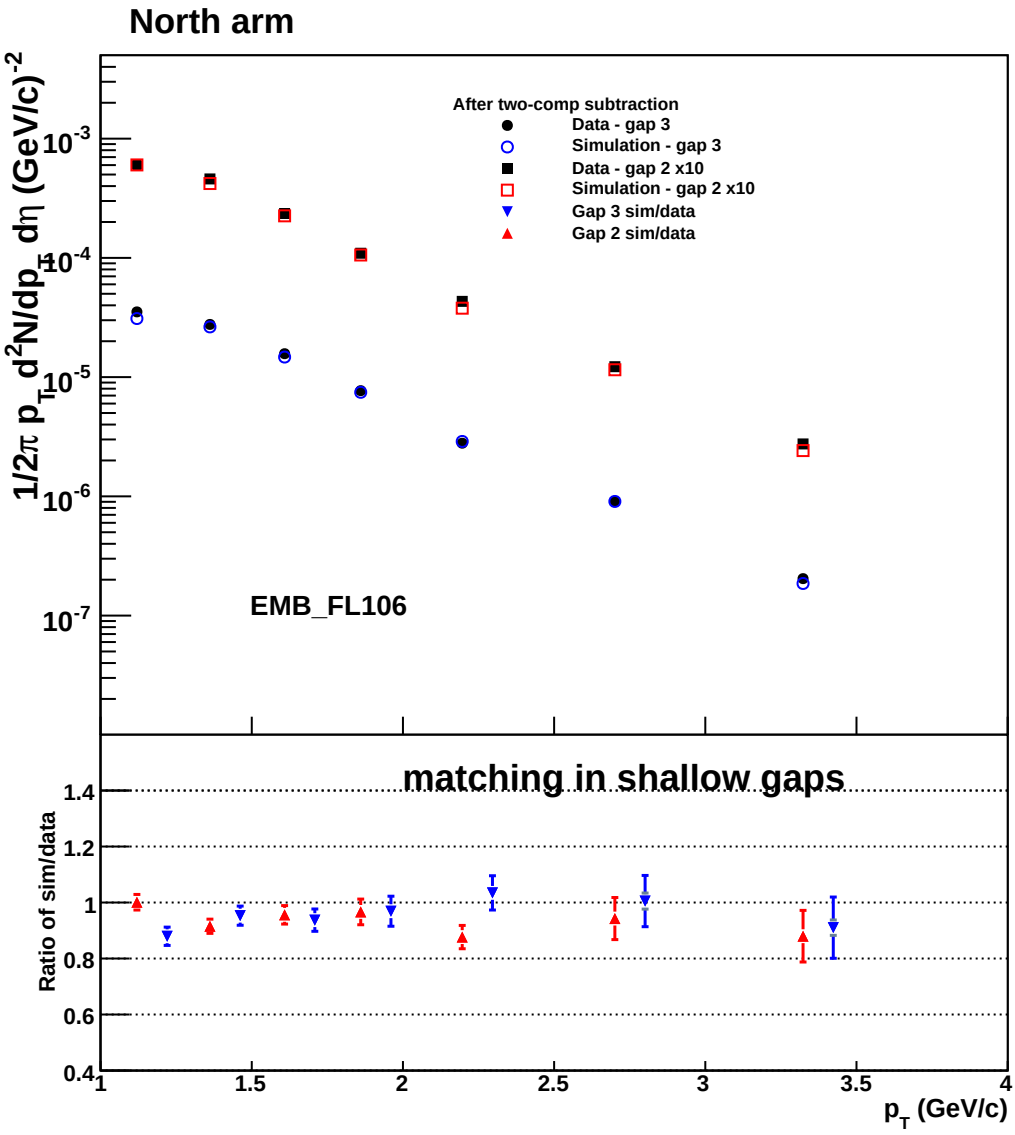

Figure 4.15: Illustration of matching of the stopped hadron fluxes for Gaps 2 and 3: (Upper plot) A direct comparison of the invariant yields of stopped hadrons in Gaps 2 and 3 in the north arm between the data (black) and the finally adjusted FL106 cocktail package output (red-Gap 2 and blue-Gap 3). (Lower) The corresponding simulation to data ratio.

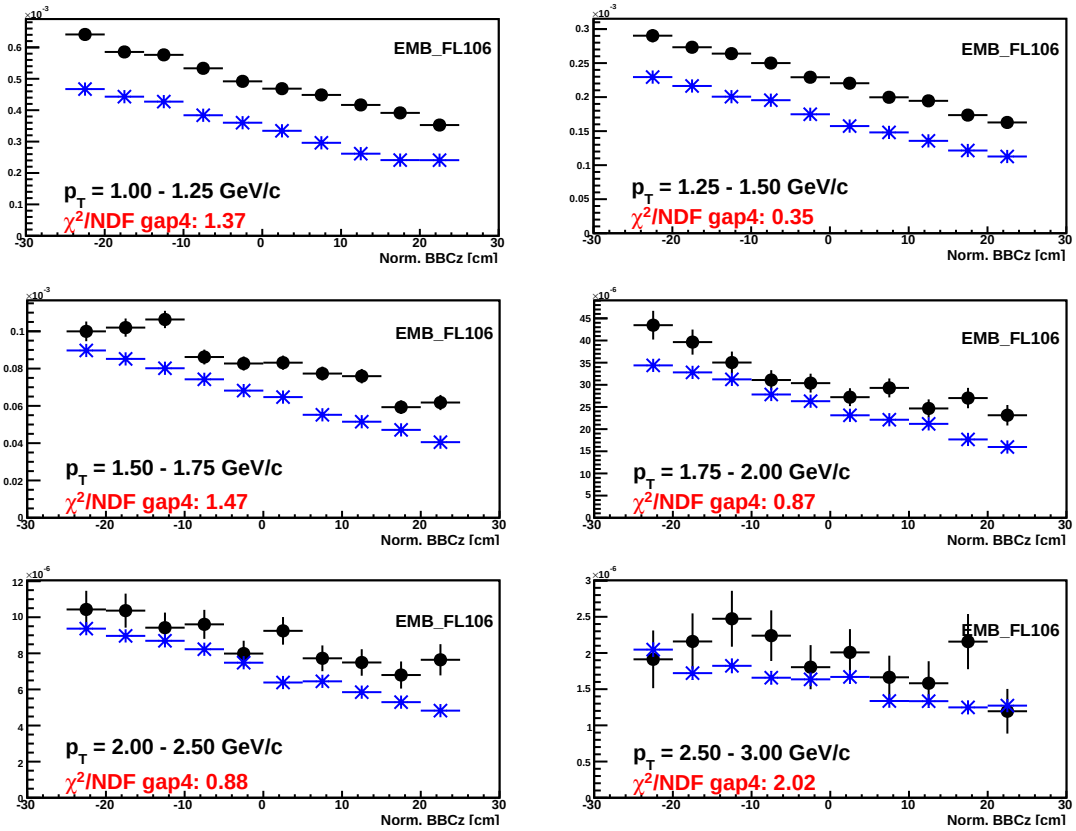

Figure 4.16: Illustration of the χ^2 matching of Z-slopes in Gap 4 of the north arm, between the data (black circles) and the prediction from the FL106 cocktail simulation package (blue stars).

Table 4.2: "Successful" MC to data matching criteria in Gaps 2, 3 and 4 for a given p_T bin.

Gap-4	Gap-2	Gap-3
$\chi^2_{Gap4}/ndf < 2$	$\frac{\lvert N_2^{MC} - N_2^{data}\rvert}{N_2^{data}} < 0.25$	$\frac{\lvert N_3^{MC} - N_3^{data}\rvert}{N_3^{data}} < 0.25$

The comparison between the data and predictions from all analyzed cocktail packages in Gaps 2, 3 and 4 in all p_T bins is illustrated in Figure 4.17.

For each cocktail package, the overall matching with data is classified as "successful" in a given p_T bin, only if the conditions specified in Table 4.2 are simultaneously satisfied. As will be discussed in the subsequent sections, differences between package predictions in different gaps are folded into the systematic uncertainties for the total background prediction of a given cocktail package.

4.4.5 Combining qualified packages for full background prediction

For each p_T bin and arm, only those packages that satisfy the successful matching criteria (listed in Table 4.2) for the specified p_T bin are considered[¶]. For a given p_T each qualified package is represented with the central value of its background prediction, $N_{C,i}(p_T)$, and the systematic uncertainty associated with this prediction, $\sigma_{C,i}(p_T)$, with $i = 1, ..., nqual$, where "$nqual$" represents the total number of qualified packages for the analyzed p_T bin.

The prediction from each qualified hadron cocktail package is treated as an indepen-

[¶]In principle, a given package could pass the goodness criteria for some p_T bins, and in the same time get rejected in the other p_T bins.

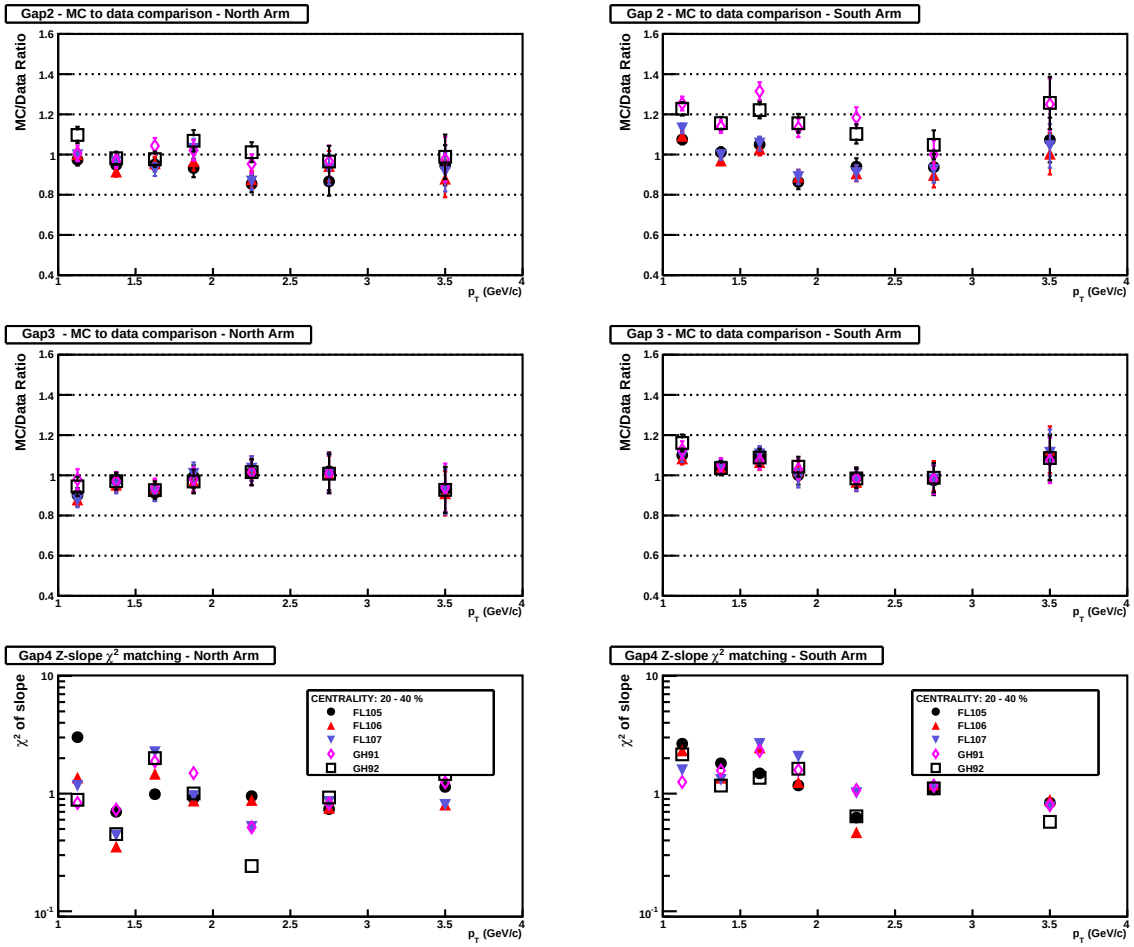

Figure 4.17: The illustration of matching in Gaps 2, 3 and 4 (from top to bottom) between the data and the different cocktail simulation yields drawn as a function of p_T, for North (left) and South (right) arms. The comparison in Gaps 2 and 3 is presented as the MC/data ratio of the stopped hadron fluxes. The comparison in Gap 4 is presented as χ^2/ndf formed from the z-vertez distributions.

dent estimate of the background in Gap 4. These independent estimates are then combined to form the final background prediction. It is important to note that the systematic uncertainty associated with the backround prediction of an individual package, $\sigma_{C,i}(p_T)$, is indeed composed of two parts:

$$\sigma^2_{C,i}(p_T) = \sigma^2_{unc,i}(p_T) + \sigma^2_{corr,i}(p_T) \tag{4.14}$$

where $\sigma^2_{unc,i}(p_T)$ is the package independent error. The $\sigma^2_{corr,i}(p_T)$ package-to-package correlated irreducible error has to be properly accounted for during the combination procedure. While the discussion of sources and numerical estimates for the systematic errors is deferred until the following sections, it is important to emphasize that for calculating the full background prediction only package independent errors are used.

The easiest option when combining several independent measurements, like $N_{C,1}$,..., $N_{C,N_{qual.}}$, is the case for which they can be treated as mutually *consistent* measurements. In this case, the combined value formed from these measurements can be calculated using the following standard formula:

$$N_C = \frac{\sum_{i=0}^{nqual} N_{C,i}/\sigma^2_{unc,i}}{\sum_{i=0}^{nqual} (1/\sigma^2_{unc,i})} \tag{4.15}$$

with the following corresponding systematic uncertainty:

$$\sigma_{comb,unc} = \frac{1}{\sum_{i=0}^{nqual} (1/\sigma^2_{unc,i})} \tag{4.16}$$

where $\sigma_{unc,i}$s represents the package uncorrelated systematic errors, with N_C as the combined weighted mean and $\sigma_{comb,unc}$ as total combined package uncorrelated error.

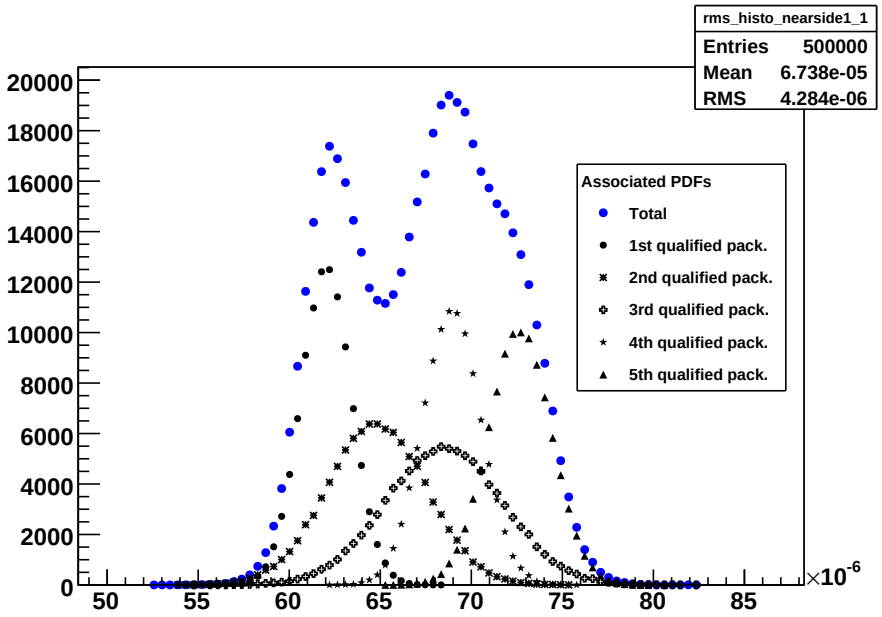

Figure 4.18: Illustration of the procedure for combining several Gaussian PDF's (black markers) into one "global" distribution (blue markers). Each Gaussian PDF is associated with an individial qualified package by selecting its mean and standard deviation as background prediction and its package uncorrelated error, respectively. The same normalization for each Gaussian has been used.

However, for a given p_T bin, the individual cocktail package predictions are not necessarily consistent. Therefore, Equations 4.15 and 4.16 cannot be used for calculating N_C or $\sigma_{comb,unc}$. Instead, an alternative procedure has been used.

For each p_T, a unique Gaussian probability density function, corresponding to each qualified package prediction, is constructed, for which $N_{C,i}$ and $\sigma_{unc,i}$ are set as its mean value and standard deviation. In addition, all gaussian PDF's are assumed to have the same normalization. Then, as illustated in Figure 4.18, for each p_T all Gaussian probability functions are summed up to form the "global" PDF for this p_T bin, $f(p_T) = f(N_{C,1} \pm \sigma_{unc,1}, ..., N_{C,npack} \pm \sigma_{npack})$.

The mean value of this global function is then selected as the central value of the

final full background prediction,

$$N_C(p_T) = \langle f(p_T) \rangle. \tag{4.17}$$

The RMS value of the same global distribution is assigned as the total package uncorrelated error:

$$\sigma_{comb,unc}(p_T) = f_{rms}(p_T), \tag{4.18}$$

which at the next step is combined with the package-to-package correlated uncertainty to form the total uncertainty,$\sigma_C(p_T)$, for the full background prediction, $N_C(p_T)$:

$$\sigma_C^2(p_T) = \sigma_{comb,unc}^2(p_T) + \sigma_{corr}^2(p_T). \tag{4.19}$$

4.4.6 Sources of systematic uncertainty for the background prediction

The full background prediction estimated by any given package consists of two components, decay muons and punchthrough hadrons. Thus for a given p_T the total error on full background prediction could be calculated via the following equation:

$$\sigma_{total}^2(p_T) = \sigma_{DM}^2(p_T) + \sigma_{PT}^2(p_T) \tag{4.20}$$

where σ_{DM} and σ_{PT} represent absolute uncertainty for the decay muon and punchthrough hadron components, respectively. Switching from absolute to fractional errors results in:

$$\delta_{total}^2(p_T) = \left(C_{DM}(p_T) \cdot \delta_{DM}(p_T)\right)^2 + \left(C_{PT}(p_T) \cdot \delta_{PT}(p_T)\right)^2 \tag{4.21}$$

with C_{DM} and C_{PT} being relative fractions of decay muon and punchthrough components within the full background prediction, respectively.

Table 4.3: List of sources of systematic unsertainties for background predictions for a given qualified simulated cocktail package, and whether they contribute to the full background components, package and p_T dependence.

Error sources		Background contribution	Pack. corr.	arm corr.
1.	Gap 3 matching hadronic cocktail to data	DM	no	no
2.	Combined Gaps 2 and 3 matching hadronic cocktail to data	PT	no	no
3.	Gap 3 statistical error on cocktail to data matching	both	yes	no
4.	Gap 3 to gap4 inefficiency	both	yes	no
5.	Hadron cocktail input, including K/π ratio uncertainty	both	yes	yes

The sources that directly contribute to the systematic uncertainties of the full background prediction are described in the Table 4.3.

Sources 1 and 2 specified in Table 4.3 originate from the difference between MC and data in Gaps 2 and 3 and contribute to the full package independent error calculated with Equation 4.21. Sources 3 and 4 contribute to the irreducable package-to-package correlated error. Although errors from source 5 are package to package correlated errors, there are also arm-to-arm correlated errors. These are taken into account only at the very last stage, when the results from the two arms combined.

4.5 Extraction of the single muon yield

For each arm the single muon yield is calculated using Equation 4.3

$$N_\mu(p_T) = \frac{1}{2\pi p_T}\frac{1}{dydp_T}\frac{N_{I,raw} - N_{C,raw}}{N_{MB}\cdot A\epsilon_\mu} = \frac{N_{\mu,raw}}{A\epsilon_\mu}. \tag{4.22}$$

In this analysis no significant systematic uncertainty is attributed to the total inclusive flux at gap 4, N_I. Therefore, the absolute systematic uncertainty of the subtracted raw muon yield, defined as $\sigma_{\mu,raw}(p_T)$, is equal to the absolute uncertainty on the background prediction, $\sigma_C(p_T)$.

The systematic uncertainty for the final acceptance and efficiency corrected single muon spectra for a given arm, $\sigma_\mu(p_T)$, can be calculated via the following:

$$\sigma_\mu \equiv \sigma\Big(\frac{N_{\mu,raw}}{A\epsilon_\mu}\Big) = \frac{N_{\mu,raw}}{A\epsilon_\mu}\sqrt{\left(\frac{\sigma_{\mu,raw}}{N_{\mu,raw}}\right)^2 + \left(\frac{\sigma_{A\epsilon_\mu}}{A\epsilon}\right)^2} \tag{4.23}$$

which is equivalent to

$$\sigma_\mu(p_T) = N_\mu(p_T)\sqrt{\delta^2_{\mu,raw}(p_T) + \delta^2_{A\epsilon}(p_T)} \tag{4.24}$$

where $N_\mu(p_T)$ represents final single muon yield, with $\delta_{\mu,raw}(p_T)$ and $\delta_{A\epsilon_\mu}(p_T)$ representing fractional errors on raw muon yield and the acceptance and efficiency correction, respectively.

The main source contributing to the uncertainty $\sigma_{A\epsilon_\mu}$ is the difference between the data and MC matching for hit density distributions of tracks and roads in the MuTR and MuID, respectively, discussed in Section 4.2.3. This was estimated to be about 5% contribution to the total fractional error.

The statistical and arm correlated uncertainties are also propagated through the above described steps.

4.5.1 Combining north and south arms

The single muon yields are separately measured for both muon arms. These separate measurements are self-consistent. Therefore, the standard procedure, mathematically equivalent to that introduced with Equations 4.15 and 4.16, can be used again. The final yield averaged between the arms is calculated with the following formula:

$$N^{\mu}_{arm,comb}(p_T) = \frac{\omega_S N^{\mu}_S + \omega_N N^{\mu}_N}{\omega_S + \omega_N} \tag{4.25}$$

where N^{μ}_S and N^{μ}_N represent the invariant single muon yields in the south and north arms, respectively. The quantities ω_S and ω_N are initialized for each p_T bin with the following:

$$\omega = \frac{1}{\sigma^2_{arm,uncorr}} \tag{4.26}$$

where $\sigma^2_{arm,uncorr}$ represents the total arm-to-arm uncorrelated uncertainty, which also includes the statitistical uncertainty.

The combined statistical and arm-to-arm uncorrelated systematic uncertainties can be separately calculated as

$$\begin{aligned} \sigma_{stat} &= \sqrt{\frac{(\omega_S \sigma^S_{stat})^2 + (\omega_N \sigma^N_{stat})^2}{(\omega_S + \omega_N)^2}} \\ \sigma_{tot,unc} &= \sqrt{\frac{(\omega_S \sigma^S_{tot,unc})^2 + (\omega_N \sigma^N_{tot,unc})^2}{(\omega_S + \omega_N)^2}}. \end{aligned} \tag{4.27}$$

As was discussed above, the final arm to arm correlated systematic uncertainty is the result of the initially assessed error on the input spectra, which is propagated through the entire analysis chain separately for each arm. These uncertainties are essentially irreducible when combining two arms, and since their absolute values are only slightly different between the two arms, the final arm to arm correlated

combined value, $\sigma_{arm,corr}$, is taken as their simple average.

Finally, the final total systematic uncertainty can be written as

$$\sigma^2_{sys} = \sigma^2_{tot,unc} + \sigma^2_{arm,corr}. \tag{4.28}$$

Single muon spectra, for both arms with corresponding arm uncorrelated and arm combined correlated systematic errors for the 20 - 40% centrality class data are shown in Figure 4.19 as an example.

4.6 Extracting the nuclear modification factor

The single muon spectra separately measured in all centrality classes of Cu+Cu collisions, are combined now with the previously measured single muon spectra for Run 5 p+p collisions [22] to form the nuclear modfication factor.

4.6.1 Calculation of the R_{AA} variable

The nuclear modification factor for a given centrality class of Cu+Cu collisions, R_{CuCu}, is calculated from the following equation:

$$R_{CuCu}(p_T) = \frac{\frac{1}{2\pi p_T}\frac{d^2N_\mu^{CuCu}}{d\eta dp_T}}{\langle N_{coll}\rangle \frac{1}{2\pi p_T}\frac{d^2N_\mu^{pp}}{d\eta dp_T}} \tag{4.29}$$

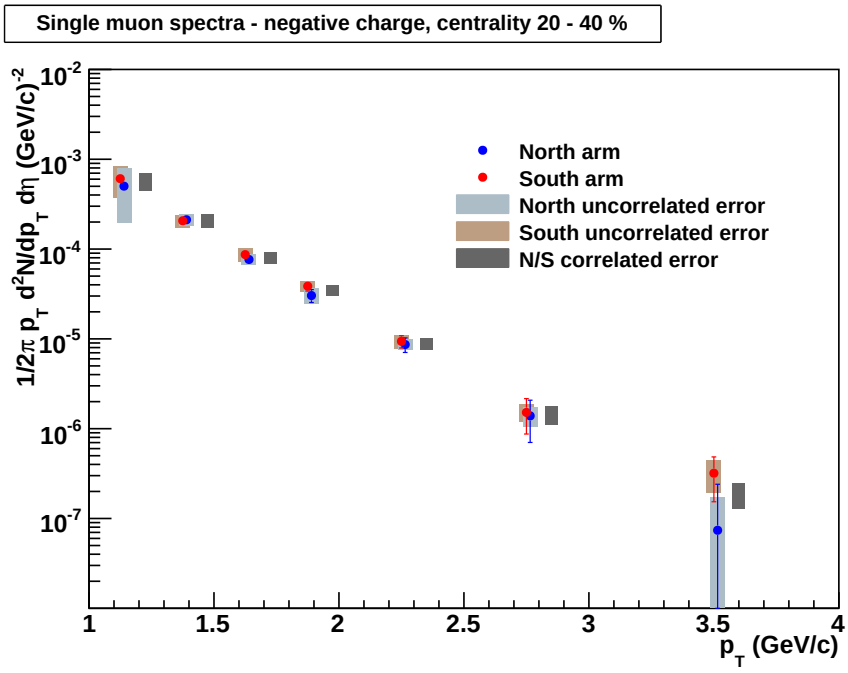

Figure 4.19: Single muon p_T spectra for 20 - 40% centrality Cu+Cu collsions separately measured for both arms drawn with arm to arm correlated and uncorrelated errors.

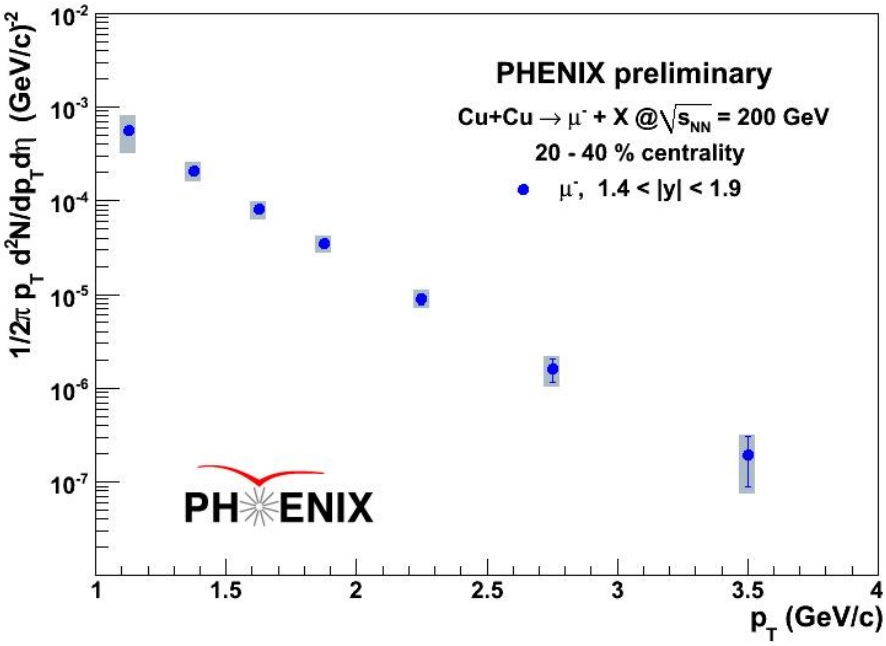

Figure 4.20: Arm combined single muon spectra for 20 - 40% centrality Cu+Cu collsions.

with $\langle N_{coll} \rangle$ representing the average number of binary collisions in the Cu+Cu collisions of the analyzed centrality class. The Equation 4.29 can be rewritten as:

$$R_{CuCu}(p_T) = \frac{\frac{1}{2\pi p_T}\frac{d^2 N_\mu^{CuCu}}{d\eta dp_T}}{\langle T_{CuCu} \rangle \frac{1}{2\pi p_T}\frac{d^2 \sigma_\mu^{pp}}{d\eta dp_T}} \tag{4.30}$$

where $\langle N_{coll} \rangle$ according to the Glauber model, described in Appendix B, was substituted using the following relation:

$$\langle N_{coll} \rangle = \langle T_{CuCu} \rangle \sigma_{p+p} \tag{4.31}$$

with $\langle T_{CuCu} \rangle$ representing the thickness function for the analyzed centrality class and σ_{p+p} the total inelastic cross section of p+p collisions.

Since the single muon spectra previously measured for Run 5 p+p collisions is available as an invariant cross section, Equation 4.30 is selected for calculating the $R_{CuCu}(p_T)$ observable for each p_T bin. However, the initial binning in p_T used for analyzing the p+p dataset is slightly different from the binning selection for the current one. Therefore, the single muon spectra measured in p+p collsions is first fit with a Kaplan-like function, as illustrated in Figure 4.21. The Kaplan fit is then used to extrapolate to the p_T point of interest. Finally, the extrapolated values are used in the denominator of Equation 4.30. The corresponding point to point systematic uncertainties are smoothly extrapolated to accomodate for the change in binning.

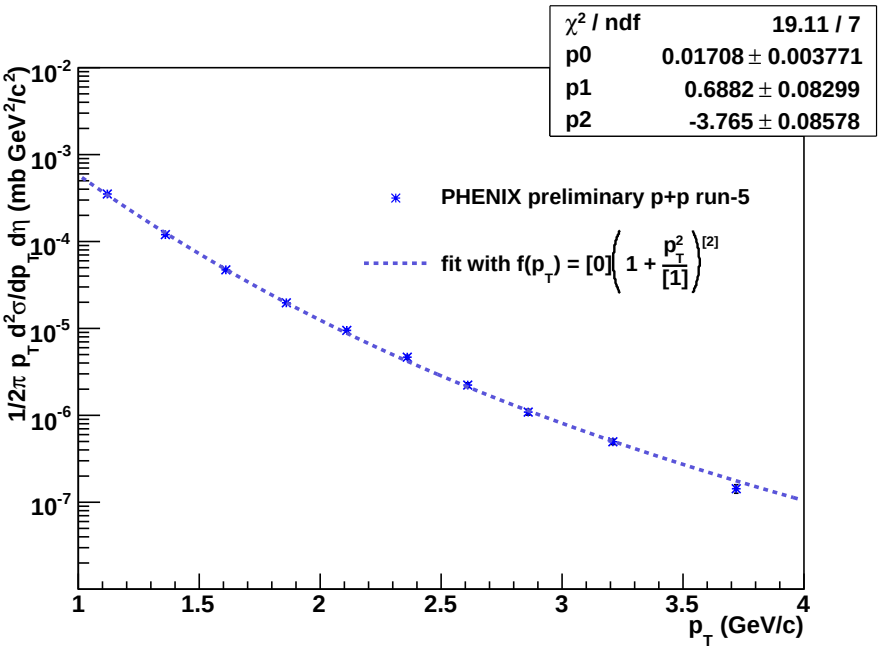

Figure 4.21: The single muon spectra measured in Run 5 p+p collisions is drawn only with the corresponding point to point uncorrelated uncertainties. The Kaplan functional form, $f(x) = p_0 \left(1 + \frac{x^2}{p_1}\right)^{p_2}$, is used in fitting this single muon spectra. The function resulting from the fitting is extrapolated afterwards to the central values of the p_T bins used in the current single muon analysis.

Chapter 5

Results and discussion

5.1 Single muon spectra and R_{AA} in Cu+Cu collisions

Based on the methodology described in the previous chapter, the single muon spectra have been calculated separately for each of the three selected centrality classes. Figures 4.20 and 5.1 show the PHENIX preliminary data of single muon invariant yield in Cu+Cu collisions at $\sqrt{s_{NN}} = 200$ GeV drawn as a function of p_T for every centrality class. As can be seen from these figures, the fractional systematic uncertainties are largest for the spectrum which corresponds to the most central collisions. This is due to expected relatively high hadron multiplicities which result in the relative increase of the background. Also due to a particularly high decay muon background fraction within the inclusive spectra and larger disagreement in background calculation for different packages the systematic uncertainty is much larger for the lowest p_T bin compared to those for the other bins.

The single muon spectra measured in Cu+Cu collisions are then compared to the

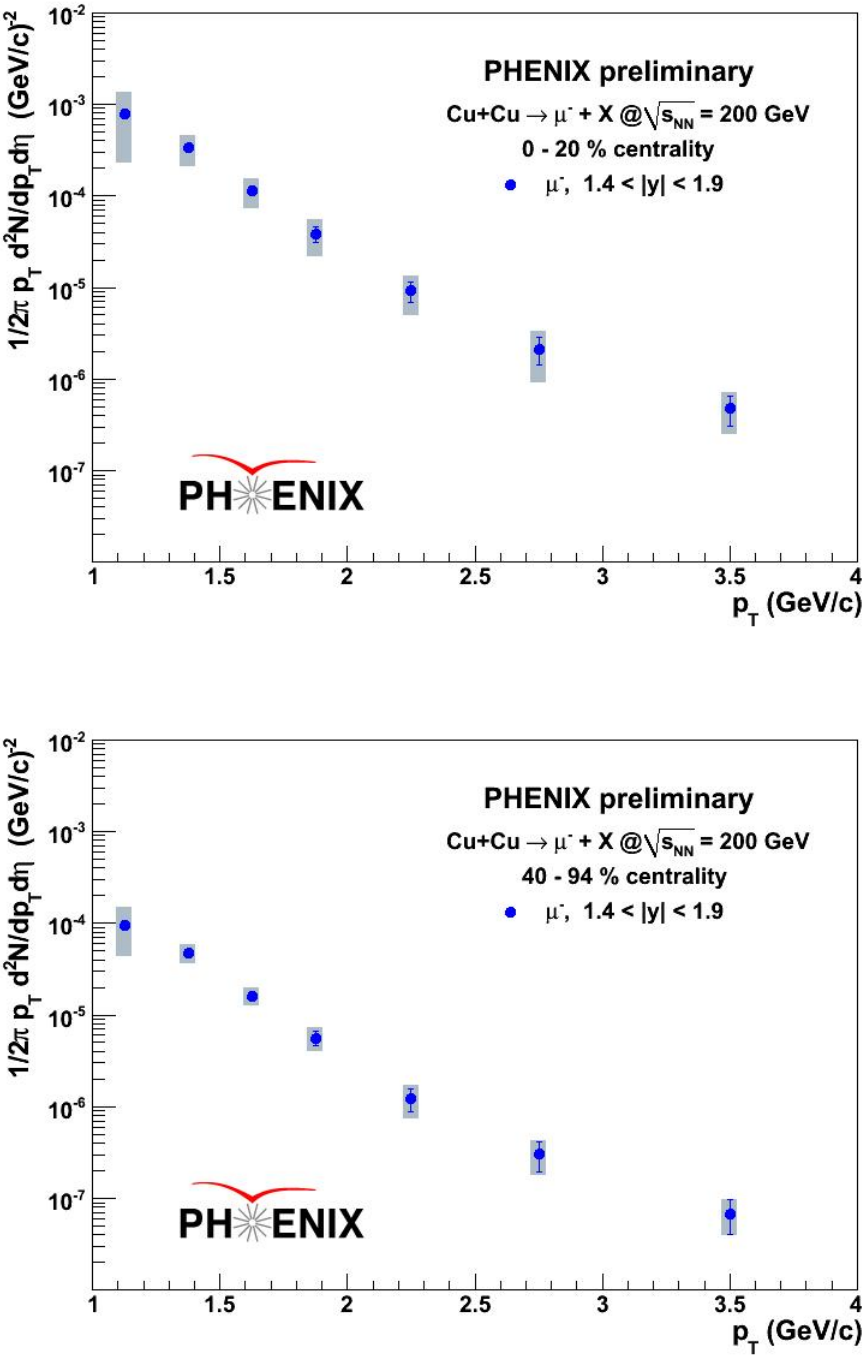

Figure 5.1: Final single muon spectra plotted separately for the analyzed three centrality classes: (upper) most central and (lower) peripheral.

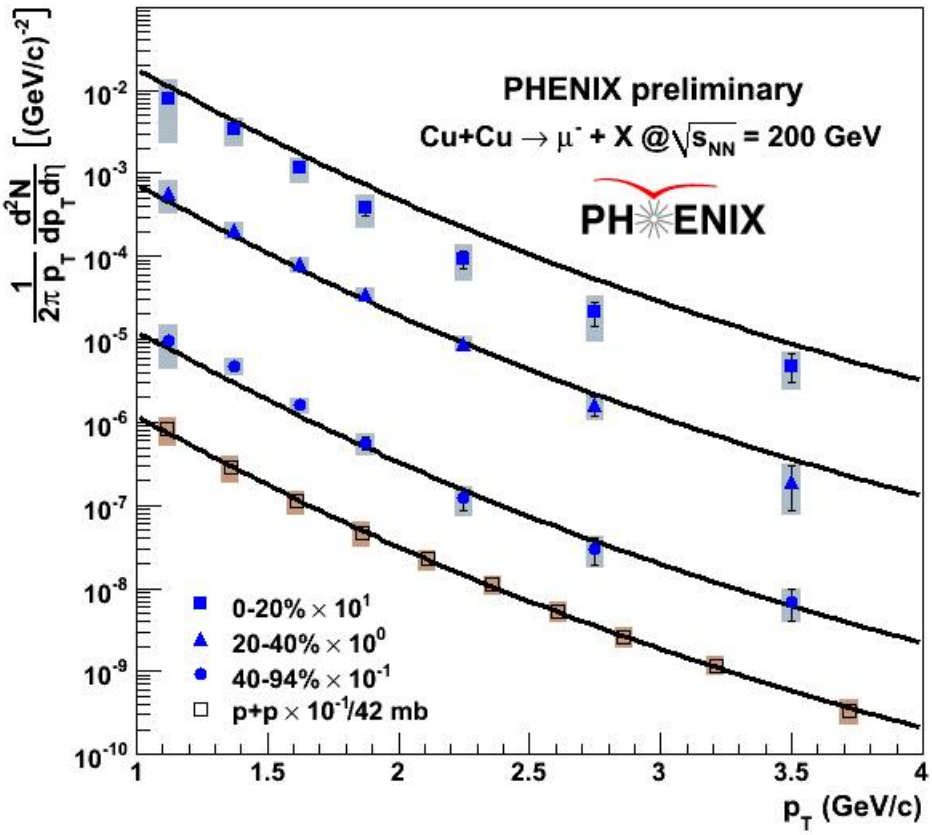

Figure 5.2: Invariant yields of muons from heavy flavor decays for different Cu+Cu centrality classes (0-20%, 20-40% & 40-94%) and for p+p collisions [40], scaled by powers of ten for clarity. The solid lines are the result of a Kaplan function ($f(x) = p_0\left(1+\frac{x^2}{p_1}\right)^{p_2}$) fit to the p+p data, scaled with $\langle T_{AA}\rangle$ for each Cu+Cu centrality class.

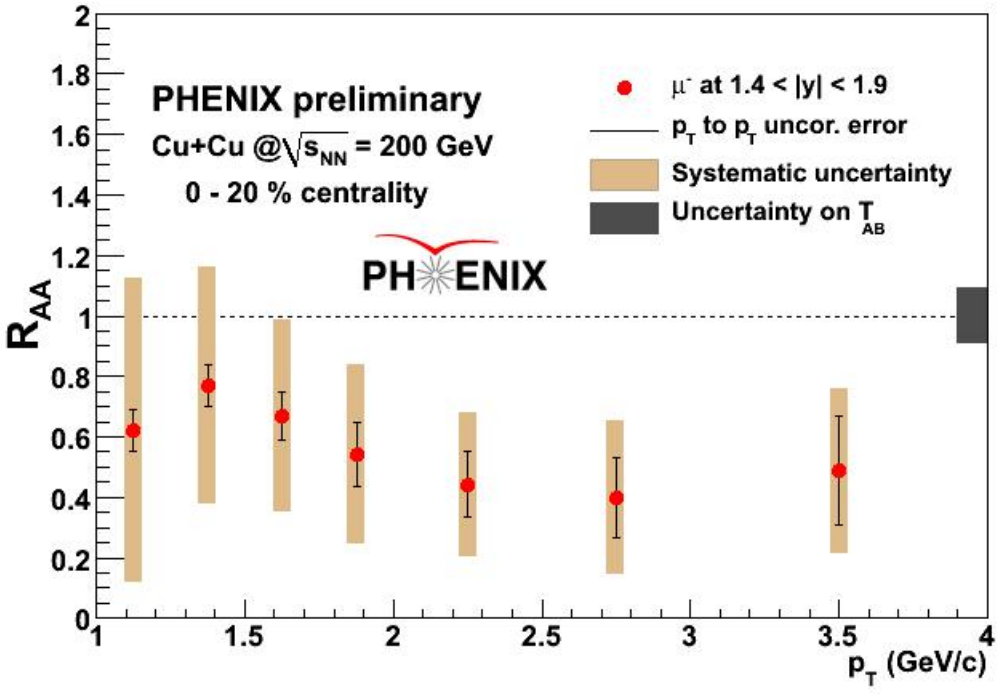

Figure 5.3: Nuclear modification factor as a function of p_T in 0-20% centrality Cu+Cu collisions.

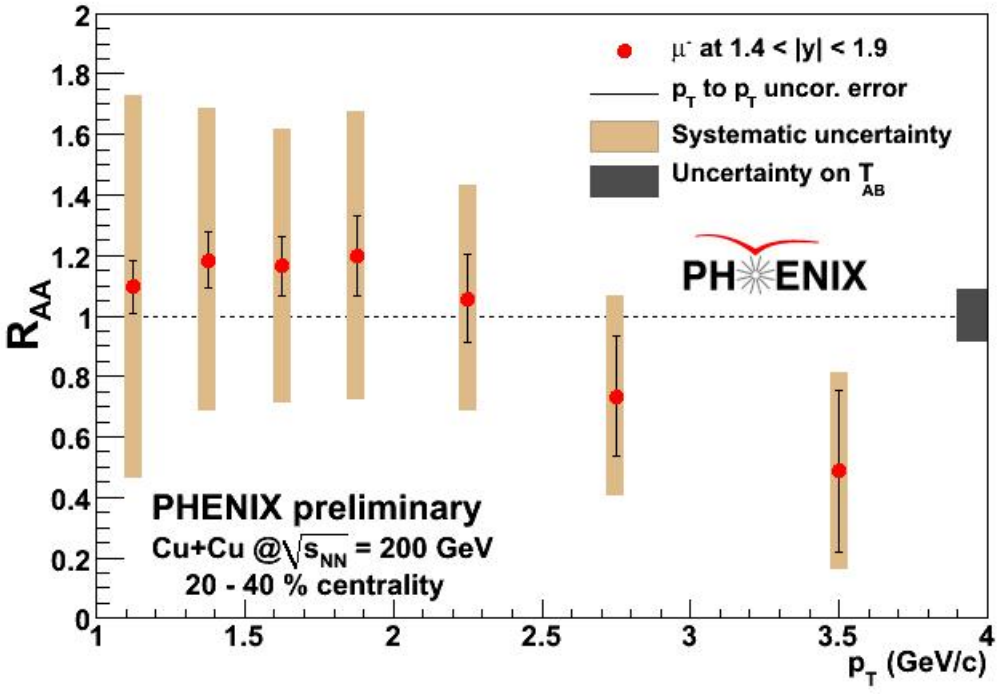

Figure 5.4: Nuclear modification factor as a function of p_T in 20-40% centrality Cu+Cu collisions.

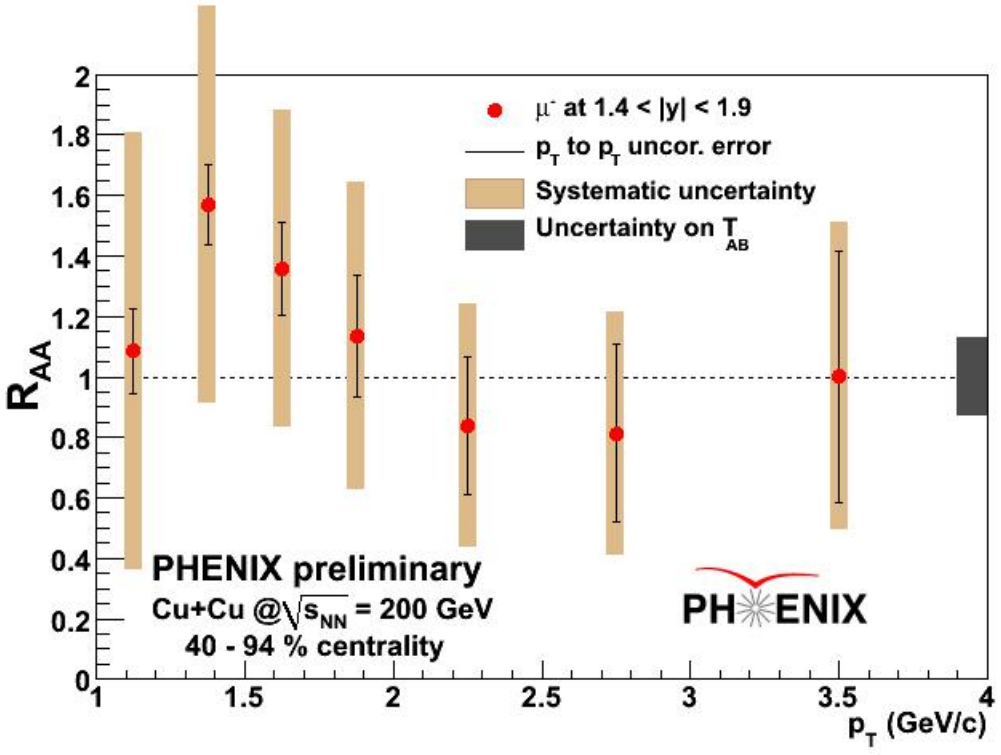

Figure 5.5: Nuclear modification factor as a function of p_T in 40-94% centrality Cu+Cu collisions.

single muon spectrum measured in p+p collisions. Figure 5.2 shows the invariant yield of heavy flavor muons for all Cu+Cu centrality classes and p+p collisions. The overlayed curves represent the Kaplan function fit to the invariant cross section of single muons in p+p collisions, described in Section 4.6.1, and scaled with the corresponding thickness function for each centrality class, $\langle T_{CuCu} \rangle$. As can be seen from this figure, the single muon spectra agree with the scaled p+p reference spectra in all Cu+Cu centralities classes except the most central class, where suppression with respect to the p+p reference is clearly observed.

This effect is more clearly quantified by calculating the nuclear modification factor, $R_{CuCu}(p_T)$. The nuclear modification factor is determined for each Cu+Cu centrality class using the procedure described in Section 4.6.1. Figures 5.3, 5.4 and 5.5 show the nuclear modification factor of heavy flavor muons calculated as a function of p_T for all the Cu+Cu centrality classes. As can be seen from the figures the nuclear modification factors for the perhipheral and mid-central classes are consistent with the unity across the entire p_T range. In contrast a significant suppression can be clearly observed for central collisions for heavy flavor muons produced in the kinematic region above $p_T = 2$ GeV/c, albeit with large overall systematic uncertainties.

5.2 Comparisons and discussion

For each Cu+Cu centrality class the measured transverse spectra of single muons can be further utilized to calculate the total production cross section for heavy flavor muons. This is usually done by extrapolating the existing measured spectrum to the $p_T = 0$ GeV/c. Unfortunately very large systematic uncertainties in the lowest available p_T bin of the single muon spectra do not allow to making a reasonable measurement.

On the other hand, the presented single muon spectra provide the ability to deter-

mine the production of heavy flavor at higher transverse momenta within reasonable systematic uncertainties. To quantify heavy flavor production at higher p_T in Cu+Cu collisions, the nuclear modification factor, R_{AA}, is determined by combining numerator and denominator, both integrated above $p_T = 2.0$ GeV/c. For each Cu+Cu centrality class the R_{AA} variable is defined as:

$$R_{AA} = \frac{\int \frac{1}{2\pi p_T} \frac{d^2 N_\mu^{CuCu}}{d\eta dp_T} dp_T}{\langle T_{CuCu} \rangle \int \frac{1}{2\pi p_T} \frac{d^2 \sigma_\mu^{pp}}{d\eta dp_T} dp_T} \tag{5.1}$$

where T_{CuCu} is thickness function for a given centrality.

Figure 5.6 shows measurements of the nuclear modification factor for open heavy flavor production at higher transverse momenta in Cu+Cu collisions at forward rapidity and in Au+Au collisions at mid-rapidity, both at $\sqrt{s_{NN}} = 200$ GeV, plotted as a function of the average number of participants, $\langle N_{part} \rangle$, for each corresponding centrality class. The red squares on this figure define the present measurement of the nuclear modification factor for single muons above $p_T = 2.0$ GeV/c, determined from Equation 5.1 for each Cu+Cu centrality class. The blue circles represent the PHENIX measurement of nuclear modification factor for non-photonic electrons above $p_T = 3.0$ GeV/c for each Au+Au centrality class [45]. As can be seen from Figure 5.6, R_{AA} for production of higher transverse momenta non-photonic $e^{\pm}$'s in Au+Au collisions decreases gradually with centrality (increasing number of participants), indicating a suppression of more than of a factor of 2 in the most central Au+Au class. On the other hand, the R_{AA} measurement for heavy flavor muons above $p_T = 2$ GeV/c also shows a significant heavy flavor suppression in the most central Cu+Cu collision.

It is needless to say that the comparison illustrated in Figure 5.6 is clearly not of an apples to apples type. The thing is that there is no open heavy flavor measurement

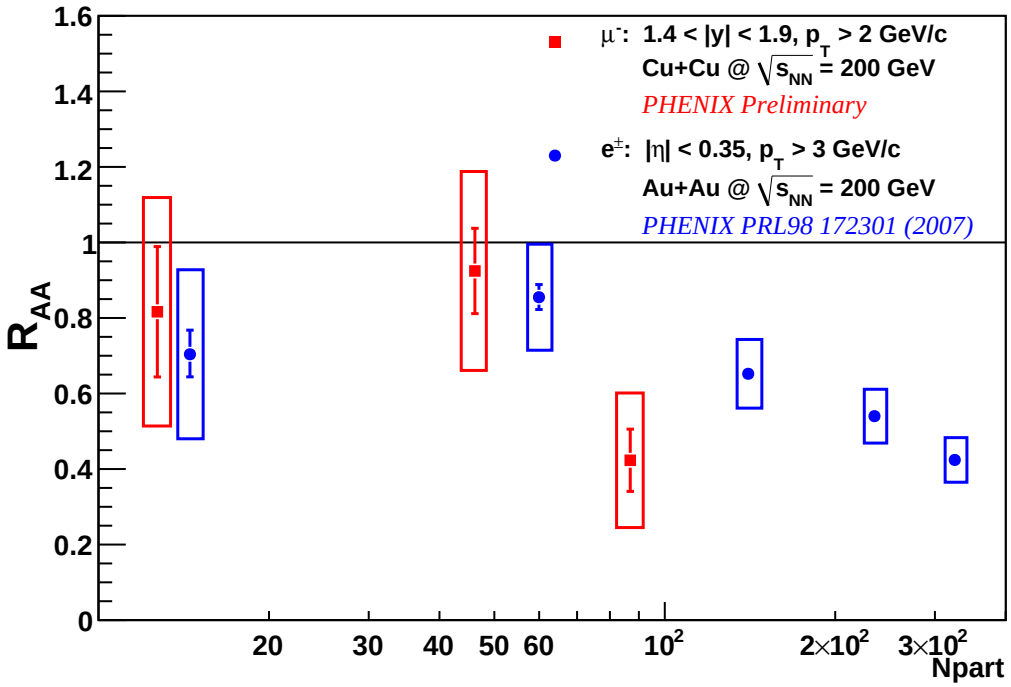

Figure 5.6: The comparison of the nuclear modification factor as a function of N_{part} between the single muons reconstructed above $p_T > 2$ GeV/c in Cu+Cu collisions (red squares) and non-photonic electrons reconstructed above $p_T > 3$ GeV/c in Au+Au collisions (blue circles).

at forward rapidity in Au+Au collisions at $\sqrt{s_{NN}} = 200$ GeV. As for the open heavy flavor measurement at mid-rapidity for Cu+Cu collisions at $\sqrt{s_{NN}} = 200$ GeV, STAR has a preliminary measurement of the nuclear modification factor for non-photonic $e^{\pm}$'s above $p_T = 3.0$ GeV/c [42], $R_{AA} = 0.62 \pm 0.10(stat.)^{+0.14}_{-0.16}(sys.)$, measured for the (0-54%) centrality range. While this measurement in principle agrees with the PHENIX measurements, the rather large centrality range it was made in, makes it difficult to make a qualitative comparison with the present measurement.

However, the comparison illustrated in Figure 5.6 is shaping up as a very interesting result for the following reasons:

1. A naive extrapolation to the $\langle N_{part} \rangle$, which corresponds to the most central (0-20%) Cu+Cu collisions, would place non-photonic electron R_{AA} above single muon R_{AA} indicating a smaller heavy flavor suppression at mid-rapidity compared to that at forward rapidity. However, based on Equation 1.2 and the rapidity evolution of measured particle multiplicities, illustrated in Figure 5.7, the Bjorken energy density of the medium created as the result of heavy ion collisions at $y = 1.65$ is expected to be 20-25 % lower compared to that at mid-rapidity. Thus, the effects induced by strongly interacting medium are expected to be smaller.

2. Heavy flavor suppression in most central Cu+Cu collisions at forward rapidity is perhaps, as large as that in the most central Au+Au collisions at mid-rapidity. If the present result for Cu+Cu collisions is verified with a smaller systematic uncertainties, it could be very significant, because even at a given rapidity the Bjorken energy density in the central Cu+Cu collsions, ϵ_{Bj}^{CuCu}, is expected to be by about a factor of 2 lower than the Bjorken energy density in the central Au+Au collsions, ϵ_{Bj}^{CuCu}. This assumption can be studied by considering the $\frac{\epsilon_{Bj}^{AuAu}}{\epsilon_{Bj}^{CuCu}}$ ratio determined by utilizing Equation 1.2:

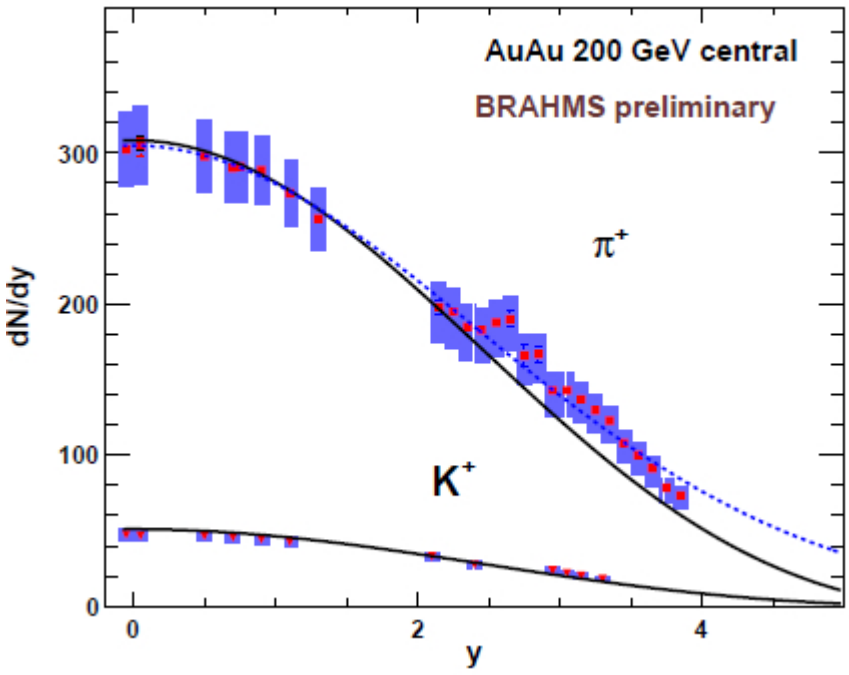

Figure 5.7: Rapidity dependence of positively charged pion and kaon production in 0-10% central Au+Au collisions at $\sqrt{s_{NN}} = 200$ GeV measured with the BRAHMS collaboration [73].

$$\frac{\epsilon_{Bj}^{AuAu}}{\epsilon_{Bj}^{CuCu}} = \frac{\left[\frac{\langle m_T \rangle}{\tau_0} \frac{dN}{A_T} \frac{dN}{dy}\right]_{AuAu}}{\left[\frac{\langle m_T \rangle}{\tau_0} \frac{dN}{A_T} \frac{dN}{dy}\right]_{CuCu}} \tag{5.2}$$

Assuming that $\langle m_T \rangle$ and τ_0 stays approximately unchanged between the Au+Au and Cu+Cu systems at a given $\sqrt{s_{NN}} = 200$ GeV, and the transverse overlap area of colliding nuclei, $A_T \sim A^{2/3}$, where A is the atomic number of the analyzed nuclei [74], Equation 5.2 can be rewritten as:

$$\frac{\epsilon_{Bj}^{AuAu}}{\epsilon_{Bj}^{CuCu}} = \frac{\left[\frac{dN}{dy}\right]_{AuAu}}{\left[\frac{dN}{dy}\right]_{CuCu}} \left(\frac{A_{Cu}}{A_{Au}}\right)^{2/3} \tag{5.3}$$

where $A_{Au} = 197$ and $A_{Cu} = 65$ are atomic numbers for gold and copper nuclei,

respectively. After a rough comparison of the measured particle multiplicities in the most central Au+Au and Cu+Cu collisions at $\sqrt{s_{NN}} = 200$ GeV [75], one gets $\frac{\epsilon_{Bj}^{AuAu}}{\epsilon_{Bj}^{CuCu}} \sim 1.8$.

The present heavy flavor measurement in Cu+Cu collisions at forward rapidity indicates the larger suppression, beyond what is expected based solely on the known energy loss mechanisms of strongly interacting matter expected to be created in the heavy ion collisions. This might also suggest that there are rather large nuclear matter effects affecting the production of heavy flavor at the initial stages of the collisions before the QGP is expected to form. It is also important to note that the PHENIX measurements of charmonium production in both Cu+Cu and Au+Au collisions [76] also indicate larger effects at forward rapidity compared to mid-rapidity.

Chapter 6

Conclusions

This thesis presents a first measurement of the nuclear modification in Cu+Cu collisions at $\sqrt{s_{NN}} = 200$ GeV for production of open heavy flavor at forward rapidity. The nuclear modification factor, R_{AA}, for production of single muons from heavy flavor decay at $\langle y \rangle = \pm 1.65$ has been measured in three different Cu+Cu centrality classes (0-20%, 20-40%, 40-94%), as shown in Figures 5.3, 5.4 and 5.5. For each Cu+Cu centrality, the $R_{AA}(p_T)$ observable has been determined by combining the transverse momentum spectra of the single muon invariant yield measured in Cu+Cu collisions for this centrality and the single muon invariant cross section measured in p+p collisions at $\sqrt{s} = 200$ GeV, illustrated in Figure 5.2.

This thesis presents a number of novel measurements and developments including:

- First measurement of nuclear modification factor (R_{AA}) for production of open heavy flavor in heavy ion collisions at forward rapidity.
- First measurement of transverse momentum spectra of invariant yields of production of heavy flavor in symmetric heavy ion collisions at forward rapidity.
- First measurements concerning production of open heavy flavor in Cu+Cu

collisions at any rapidity.

- First measurement indicating significant suppression of open heavy flavor production at higher transverse momenta at forward rapidity.
- First measurement indicating possible significant suppression of open heavy flavor production at higher transverse momenta at any rapidity for a heavy ion colliding system smaller than Au+Au.
- Indication of stronger suppression of open heavy flavor production at higher transverse momenta at forward rapidities in Cu+Cu collisions than at central rapidity in Au+Au collisions for an equivalent number of participants.
- Extension, including significant improvements and refinements, of new background subtraction framework to high-multiplicity (central Cu+Cu) regime.
- Exploration of method to further reduce systematic errors for nuclear modification factor (RAA) using enhanced framework for joint measurement of numerator and denominator.

The single muon spectra in Cu+Cu collisions presented here are the first measurement of transverse momentum spectra of invariant yields of production of open heavy flavor in symmetric heavy ion collisions at forward rapidity.

The measurements of the nuclear modification factor for single muon production as a function of p_T indicates significant suppression of open heavy flavor production for the transverse momenta above $p_T = 2$ GeV/c in most central (0-20%) Cu+Cu collisions, whereas the $R_{AA}(p_T)$ measurements for other Cu+Cu centrality classes are consistent with no suppression across the entire transverse momentum spectra.

Indeed, this is the first measurement indicating the suppression of open heavy flavor production has been observed at any rapidity for a heavy ion colliding at $\sqrt{s_{NN}} = 200$

GeV system smaller than Au+Au*. Furthermore, comparing the nuclear modification factor of heavy flavor production at higher p_T in central Cu+Cu collisions at $\sqrt{s_{NN}} =$ 200 GeV at forward rapidity to that in Au+Au collisions at $\sqrt{s_{NN}} = 200$ GeV for an equivalent number of participants at mid-rapidity indicates a stronger suppression of open heavy flavor production. This result is significant, since Cu+Cu collisions are expected to produce matter with a much smaller Bjorken energy density, ϵ_{Bj}, compared to that in Au+Au collisions. In addition, ϵ_{Bj} is expected to be smaller at forward rapidity compared to that at mid-rapidity due to a relatively smaller measured particle multiplicity. Therefore, one expects smaller effects for open heavy production in Cu+Cu collisions due to strongly interacting matter, quite different from what the presented data indicates.

At this point, the lack of both the measurement of the corresponding open heavy flavor production for different classes in Cu+Cu collisions at mid-rapidity and a theoretical prediction for the possible nuclear matter effects on heavy flavor production at forward rapidity makes a further qualitative comparison very difficult. On the other hand, further reducing systematic uncertainties for this measurement is of great importance.

The methodology of single muon signal extraction used in the presented work was pioneered by a former University of Tennessee student Donald Hornback for measuring single muon invariant cross section in p+p collisions at $\sqrt{s} = 200$ GeV [22]. The analysis framework, specifically the procedure for background estimation with hadron cocktail, has been significantly improved and modified for the presented measurement. Additionally, the background simulations were embedded into Cu+Cu data to account for the detector performance in the high-multiplicity environment, which is expected in central Cu+Cu collions.

*There are no other measurements of nuclear modification factor for open heavy flavor production in Cu+Cu collisions at $\sqrt{s_{NN}} = 200$ GeV

The results presented in this dissertation achieved PHENIX preliminary status in March 2009. They were presented for the first time at the Quark Matter 2009 conference held in Knoxville (March 29 - Arpril 4, 2009) and has been published in the conference proceedings [77].

There is a room for further improvements providing a straightforward path to the publication by PHENIX. The method for further reducing systematic uncertainties for nuclear modificarion factor, R_{AA}, which uses global enhanced fromawork for joint measurement of numerator and denominator, has been explored and underway. This approach allows cancellation of common sources of systematic errors between the numerator and denominator in the nuclear modification factor, not possible for the presented measurement since it is resulted from combining two independent measurements.

Finally, upcoming PHENIX detector upgrades, specifically the addition of the Forward Silicon Vertex Detector (FVTX) which will be installed by the Run-11 in 2011, will greatly improve heavy flavor measurements at forward rapidity. The approximately 100μm spatial resolution for track vertex reconstruction which the FVTX is expected to provide [78], will be instrumental in greatly reducing the decay muon background contamination in the inclusive yields of single muon candidates.

Bibliography

Bibliography

[1] Michael E. Peskin and Daniel V. Schroeder. *Quantum Field Theory.* Addison-Wesley, 1995.

[2] D. J. Gross and F. Wilczek. *Phys. Rev. Lett.*, **30**:1343–6, 1973.

[3] H. D. Politzer. *Phys. Rev. Lett.*, **30**:1346–9, 1973.

[4] Cheuk-Yin Wong. *Introduction to High-Energy Heavy-Ion Collisions.* World Scientific, 1994.

[5] E. V. Shuryak. *Phys. Rept.*, **61**, 1980.

[6] J. D. Bjorken. *Phys. Rev.*, **D27**:140, 1983.

[7] K. Adcox et al. *Nucl.Phys.*, **A757**:184–283, 2005.

[8] S. S. Adler et al. *Phys. Rev. Lett.*, **91**:172301, 2003.

[9] J. Adams et al. *Phys. Rev. Lett.*, **91**:172304, 2003.

[10] S. S. Adler et al. *Phys. Rev. Lett.*, **91**:182301, 2003.

[11] J. Adams et al. *Phys. Rev.*, **C72**:014904, 2005.

[12] P. Huovunen, P. F. Kolb, U. W. Heinz, P. V. Ruuskanen, and S. A. Voloshin. *Phys. Lett.*, **B503**:58, 2001.

[13] A. Adare et al. *Phys. Rev. Lett.*, **98**:162301, 2007.

[14] J. Adams et al. *Phys. Rev. Lett.*, **92**:052302, 2004.

[15] J. Adams et al. *Phys. Rev. Lett.*, **95**:122301, 2005.

[16] T. Matsui and H. Satz. *Phys. Lett.*, **B178**:416, 1986.

[17] E. Eichten, K. Gottfried, T. Kinoshita, K. D. Lane, and T. M. Yan. *Phys. Rev.*, **D21**:203, 1980.

[18] H. Satz. *Rep. Prog. Phys.*, **63**:1511–1574, 2000.

[19] M. C. Abreu et al. *Phys. Lett.*, **B477**:28–36, 2000.

[20] M. J. Leitch. *Eur. Phys. J.*, **A19**:129, 2003.

[21] D. Antreasyn et al. *Phys. Rev.*, **D19**:764, 1979.

[22] Donald Hornback. *A measurement of open charm using single muons at forward angles for p+p collisions at center of mass energy 200 GeV.* PhD thesis, 2008.

[23] J. C. Collins, D. E. Soper, and G. Sterman. *Nucl. Phys.*, **B263**:37–60, 1986.

[24] P. Nason, S. Dawson, and R. K. Ellis. *Nucl. Phys.*, **B303**:607–633, 1988.

[25] C. Peterson, D. Schlatter, I. Schmitt, and P. M. Zerwas. *Phys. Rev.*, **D27**:105, 1983.

[26] Bo Andersson, G. Gustafson, Ingelman G., and T. Sjostrand. *Phys. Rept.*, **97**:31, 1983.

[27] C. Lourenço and H. K. Wöhri. *Phys. Rep.*, **433**:127–180, 2006.

[28] D. Acosta et al. *Phys. Rev. Lett.*, **91**:241804, 2003.

[29] Frederic J. Gilman and Jr. Robert. L. Singleton. *Phys. Rev.*, **D41**:142, 1989.

[30] Jeffrey D. Richman and Patricia R. Burchat. *Rev. of Mod. Phys.*, **67**:893, 1995.

[31] J. Y. et al Ge. *Phys. Rev.*, **D79**:052010, 2009.

[32] M. Cacciari, P. Nason, and R. Vogt. *Phys. Rev. Lett.*, **98**:122001, 2005.

[33] M. Cacciari and M. Greco. *Nucl. Phys.*, **B421**:530–544, 1994.

[34] E. Braaten et al. *Phys. Rev.*, **D 51**:4119, 1995.

[35] V. Kartvelishvili et al. *Phys. Lett.*, **B 78**:615, 1978.

[36] B. Aubert et al. *Phys. Rev.*, **D 69**:111104, 2004.

[37] A.H. Mahmood et al. *Phys. Rev.*, **D 70**:032003, 2004.

[38] C. Amsler et al. Particle data group. *Phys. Lett.*, **B667**:1, 2008.

[39] A. Adare et al. *Phys. Rev. Lett.*, **97**:252002, 2006.

[40] D. Hornback [PHENIX collaboration]. *J. Phys.*, **G35**:104113, 2008.

[41] A. Adare et al. *Phys. Lett.*, **670**:313–320, 2009.

[42] A. Knospe [for the STAR collaboration]. *Eur. Phys. J.*, **C62**:223–226, 2009.

[43] B. I. Abelev et al. *Phys. Rev. Lett.*, **98**:192301, 2005.

[44] A. Adare et al. [arXiv:0903.4851].

[45] A. Adare et al. *Phys. Rev. Lett.*, **98**:172301, 2007.

[46] David d'Enterria. arXiv:0902.2011.

[47] L. D. Landau and I. J. Pomeranchuk. *Dokl. Akad. Nauk*, **92**:92, 1953.

[48] A. B. Migdal. *Phys. Rev.*, **103**:1811, 1956.

[49] M. J. Tannenbaum. *Rep. Prog. Phys.*, **69**:2005–2059, 2006.

[50] Y. L. Dokshitzer and D. E. Kharzeev. *Phys. Lett.*, **B519**:199, 2001.

[51] M. Djorjevic, M. Gyulassy, and S. Wicks. *Phys. Rev. Lett.*, **94**:112301, 2005.

[52] A. Adare et al. *Phys. Rev. Lett.*, **96**:202301, 2006.

[53] J. L. Nagle [PHENIX collaboration]. *Eur. Phys. J.*, **A29**:7–10, 2006.

[54] N. Armesto et al. *Phys. Rev.*, **D71**:054027, 2005.

[55] M. G. Mustafa. *Phys. Rev.*, **C72**:014905, 2005.

[56] G. D. Moore and D. Teaney. *Phys. Rev.*, **C71**:064904, 2005.

[57] H. van Hees and R. Rapp. *Phys. Rev.*, **C73**:034913, 2005.

[58] A. Adil and I. Vitev. *Phys. Lett.*, **B649**:139, 2007.

[59] Cheuk-Yin Wong. *Phys. Rev.*, **C72**:034906, 2005.

[60] K. Adcox et al. *Nucl. Instr. and Meth. A*, **499**:469–479, 2003.

[61] M. Allen et al. *Nucl. Instr. and Meth. A*, **499**:549–559, 2003.

[62] S. H. Aronson et al. *Nucl. Instr. and Meth. A*, **499**:593–602, 2003.

[63] Jason Newby. *J/ψ production in Au+Au collisions at $\sqrt{s_{NN}} = 200$ GeV*. PhD thesis, 2003.

[64] R. Brun and F. Rademakers. Root - an object oriented data analysis framework. *http://root.cern.ch/*.

[65] K. Adler et al. *Phys. Rev.*, **D76**:092002, 2005.

[66] Andrew Glenn. *Single muon production and implications for charm in $\sqrt{s_{NN}} =$ 200 GeV Au+Au collisions*. PhD thesis, 2004.

[67] R. Brun. Geant 3.21 detector description and simulation tool. *CERN Program Library Long Write-up W5013*, 1994.

[68] `https://www.phenix.bnl.gov/WWW/run/05/history/brief_summary.html`.

[69] A. Bickley et al. Preliminary measurement of forward rapidity $j/\psi \rightarrow \mu^+\mu_-$ production in Run-5 $\sqrt{s_{NN}} = 200$ GeV Cu+Cu collisions. *PHENIX internal note*, 2005.

[70] M. L. Miller, K. Reygens, Stephen J. Sanders, and P. Steinberg. *Ann.Rev.Nucl.Part.Sci.*, **57**:205–243, 2007.

[71] Vince Cianciolo. Estimating $\pi^{\pm}$ yields and charged k/π ratios at forward rapidity

in p+p and Cu+Cu collisions at $\sqrt{s_{NN}} = 200$ GeV. *PHENIX internal note*, 2007.

[72] V. Ryabov [for the PHENIX Collaboration]. *arXiv:nucl-ex/0702046*, 2007.

[73] F. Videbaek [for the BRAHMS Collaboration]. *arXiv:0907.4742*, 2009.

[74] Cheuk-Yin Wong. *Private communication.*

[75] A. Adare et al. *Phys. Rev.*, **C 78**:044902, 2008.

[76] A. Adare et al. *Phys. Rev. Lett.*, **101**:122301, 2008.

[77] I. Garishvili [PHENIX collaboration]. *Nucl. Phys.*, **A830**:625c–626c, 2009.

[78] D. Butsyk [PHENIX collaboration]. *Eur. Phys. J.*, **C62**:21–24, 2009.

Appendices

Appendix A

Kinematic variables

A.1 The basic variables

The collision vertex is usually selected as the origin of coordinate system, with z-axis running along the beam pipe. Every particle produced in a given p+p or heavy ion collision can be characterized through the set of kinematic variables as energy (E), momentum $\overrightarrow{p} = (p_x, p_y, p_z)$ and mass (m), assuming that particle production is azimuthally symmetric around the z-axis. The momentum vector can be broken up to into longitudinal, p_z and transverse, $p_T = \sqrt{p_x^2 + p_y^2}$, components.

The production angle of the particles relative to the beam axis is expressed with the pseudourapidity variable defined as

$$\eta = \frac{1}{2} \ln \left(\frac{p + p_z}{p - p_z} \right), \tag{A.1}$$

where $p \equiv |\overrightarrow{p}|$. Substituting $\frac{p_z}{p}$ with $\cos\theta$, where θ is the polar angle of emitted

particle with respect to the beam axis, results in the following:

$$\eta = -\ln\left[\tan\left(\frac{\theta}{2}\right)\right]. \tag{A.2}$$

.

In the relativistic limit, $E \approx p$, pseudorapidity is approximately equal to the rapidity, y, which is defined as

$$y = \frac{1}{2}\ln\left(\frac{E+p_z}{E-p_z}\right). \tag{A.3}$$

A rapidity difference, dy, is invariant under any Lorentz boost along the z-direction. Another invariant variable under such transformations is m_T, transverse mass, defined as $m_T = \sqrt{m^2 + p_T^2}$. Finally, E and p_z can be conveniently defined with the following:

$$\begin{aligned} E &= m_T \cosh y, \\ p_z &= m_T \sinh y. \end{aligned} \tag{A.4}$$

Differentiating p_z gives,

$$dp_z = m_T d(\sinh y) = m_T \cosh y \cdot dy. \tag{A.5}$$

Using the expression for energy from Equation A.4 one arrives at

$$\frac{dp_z}{E} = dy. \tag{A.6}$$

A.2 Invariant yield

The production of the particle(s) of the interest in a high energy collision can be quantified by the following expression:

$$\frac{d^3N}{dp^3} = \frac{d^3N}{dp_x dp_y dp_z} \tag{A.7}$$

which describes the number of particles produced per event, N, over a volume of momentum space, dp^3. It is important to note that $\frac{d^3N}{dp^3}$ is not a Lorentz-invariant quantity. Assuming an azimuthally symmetric particle production, $dp_x dp_y$ can be substitued by

$$dp_x dp_y = p_T dp_T d\phi = 2\pi p_T dp_T. \tag{A.8}$$

As a result, Equation A.7 can be rewritten as

$$\frac{d^3N}{dp^3} = \frac{d^3N}{2\pi p_T dp_T dp_z}. \tag{A.9}$$

Using Equation A.6 one arrives at

$$E\frac{d^3N}{dp^3} = \frac{d^3N}{2\pi p_T dp_T dy} \tag{A.10}$$

which is a Lorenz invariant quantity.

Appendix B

Glauber Model

B.1 Framework

Geometric quantities for heavy ion collision like b, N_{coll} and N_{part} are usually calculated via the Glauber model. It assumes that during the nucleus-nucleus collisions nucleons acts as an independent entities essentially not affected by the presense of other nucleons.

A Glauber Model simulation requires a couple of inputs known from experimental data [70]. The first input is the nuclear charge density which is parametrized as follows:

$$\rho(r) = \frac{\rho_0}{1 + e^{\frac{r-r_0}{c}}}, \tag{B.1}$$

where ρ_0 denotes the density of a nucleon in its center, r_0 and c correspond to nuclear radius and "surface thickness", respectively. The second input is the inelastic nucleon-nucleon cross section, σ_{inel}^{NN}, which at $\sqrt{s} = 200$ GeV is measured to be 42 mb.

Figure B.1 illustrates geometry of a system of colliding two nuclei, where "projectile"

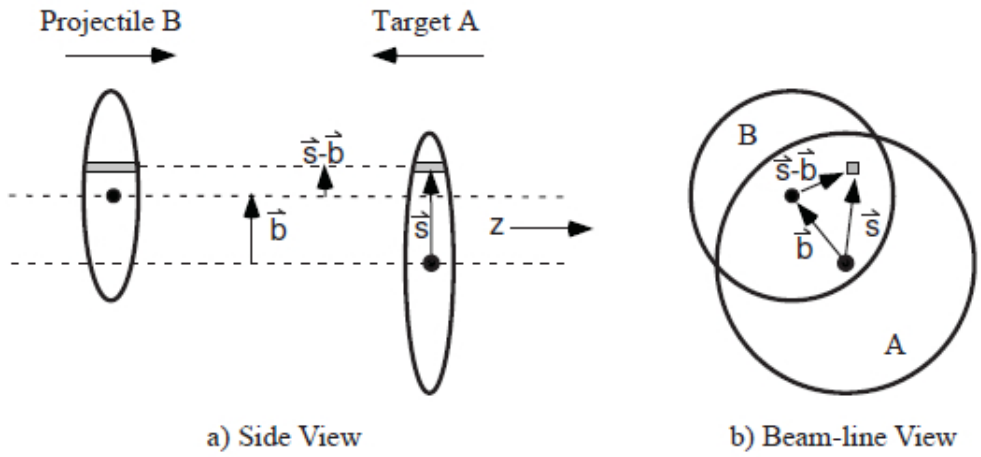

Figure B.1: Schematic view of the Glauber model geometry (a) along the beamline and (b) transverse view.

B (with B nucleons) collides with "target" A (with A nucleons) at impact parameter $\vec{b}$. The model considers two overlapping (during the collision) flux tubes that are located at distances $\vec{s}$ and $\vec{s}-\vec{b}$ from the centers of target and projectile nuclei, respectively. If one defines quantity $\rho_A(\vec{s}, z_A)$ as a probability per unit volume for finding nucleon at space point $(\vec{s}, z_A)$, the probability of a target nucleon to be found inside the target flux tube per unit transverse area is $T_A(\vec{s}) = \int \rho_A(\vec{s}, z_A)dz_A$. Likewise, quantity $T_B(\vec{s}-\vec{b}) = \int \rho_B(\vec{s}-\vec{b}, z_B)dz_B$ can be defined for the projectile nucleus. The effective overlap area for two given nucleons from target and projectile nuclei to interact called the *thickness function*, $T_{AB}(\vec{b})$, is then defined as

$$T_{AB}(b) = \int T_A(s)T_B(s-b)d^2s, \tag{B.2}$$

with d^2s denoting the differential area of overlaping flux tubes. Therefore, the probability of a specific nucleon from the target to interact with a given nucleon from the projectile is $T_{AB}(\vec{b})\sigma_{inel}^{NN}$. The probability of these N-N interactions to occur n times is

$$P(n,b) = \binom{A,B}{n} \left[T_{AB}(b)\sigma_{inel}^{NN}\right]^n \left[1 - T_{AB}(b)\sigma_{inel}^{NN}\right]^{AB-n}, \tag{B.3}$$

based on a binomial distribution.

The total number of binary (nucleon-nucleon) collisions for a given impact parameter, b, is given by:

$$N_{coll}(b) = \sum_{n=1}^{AB} nP(n,b) = ABT_{AB}(b)\sigma_{inel}^{NN}. \tag{B.4}$$

Correspondingly, the total number of participants or wounded nucleons is given by:

$$N_{part}(b) = 2A \int T_{AB}(s) \left(1 - (1 - \sigma_{inel}^{NN} T_{AB}(s-b))^{AB}\right) d^2s. \tag{B.5}$$

B.2 Centrality determination

Geometric quantities b, N_{coll} and N_{part} which characterize the *centrality* of heavy ion collisions cannot be directly measured. Instead, these variables are estimated from Glauber model simulations and then mapped to the distributions of experimentally measured observables, such as particle multiplicity, for instance. It is assumed that impact parameter, and therefore the quantities N_{coll} and N_{part}, are monotonically related to particle multiplicity. Figure B.2 from reference [70] is a cartoon illustration of a typical procedure that bins a given cumulative distribution of particle multiplicity into different collision centralities. The same procedure is performed both for a Glauber model simulation and the data. The average values of geometric quantities ($\langle b \rangle$, $\langle N_{coll}(b) \rangle$ and $\langle N_{part}(b) \rangle$) from Glauber model are then associated to each centrality bins.

Using Equation B.4 the average value of the thickness function for a given centrality class can be calculated from:

$$\langle T_{AB} \rangle = \langle N_{coll} \rangle \sigma_{inel}^{NN} \tag{B.6}$$

where $T_{AB}(b)$ was normalized as follows:

$$\int T_{AB}(b)d^2b = AB. \tag{B.7}$$

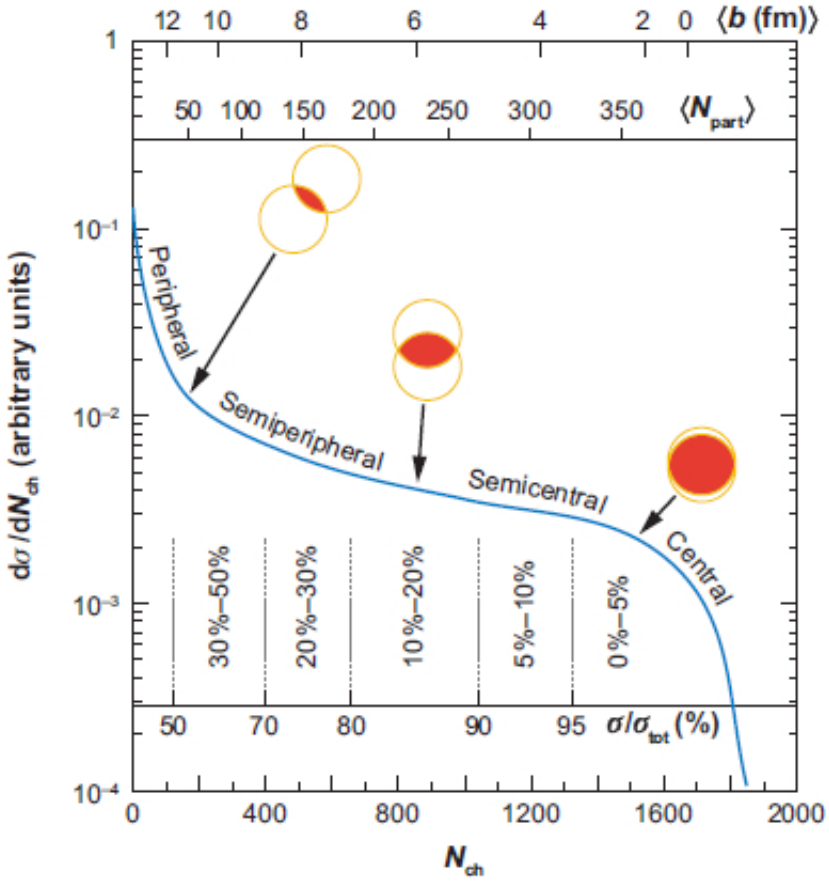

Figure B.2: Pictorial illustration of the procedure which correlates experimentally measured particle multiplicity, N_{ch}, with geometric observables extracted from Glauber model.

Appendix C

"Good" run list

Table C.1: Runs selected for the single muon analysis

150513, 151086, 151192, 151193, 151194, 151206, 151225, 151226, 151227, 151239, 151439, 151443, 151449, 151461, 151462, 151577, 151582, 151645, 151646, 151648, 151649, 151827, 151834, 151887, 151891, 151892, 151898, 151914, 151915, 151916, 152081, 152082, 152085, 152088, 152093, 152094, 152099, 152101, 152107, 152130, 152135, 152136, 152158, 152169, 152193, 152194, 152195, 152202, 152203, 152204, 152230, 153284, 153286, 153519, 153525, 153561, 153576, 153651, 153741, 153747, 153750, 153770, 153824, 153829, 153835, 153837, 154104, 154105, 154106, 154120, 154121, 154122, 154123, 154126, 154129, 154298, 154300, 154301, 154305, 154345, 154349, 154351, 154353, 154381, 154628, 154631, 154632, 154633, 154644, 154650, 154653, 154655, 154658, 154674, 154682, 154851, 154852, 154854, 154856, 154900, 154904, 154909, 154917, 154921, 154922.
155661, 155664, 155665, 155666, 155667, 155669, 155674, 155676, 155678, 155681, 155704, 156568, 156569, 156570, 156571, 156602, 156603, 156604, 156605, 156606, 156607, 156621, 156679, 156721, 156725, 156737, 156753, 156756, 156758, 156763, 156764, 156766, 156769, 156770, 156832, 156834, 156862, 156887, 156888, 156942, 156946, 156947, 156949, 156982, 156987, 156991, 157090, 157095, 157097, 157099, 157112, 157113, 157114, 157115, 157119, 157155, 157157, 157179, 157181, 157299, 157309, 157311, 157322, 157324, 157644, 157649, 157659, 157676, 157681, 157684, 157702, 158972, 158973, 158975, 158977, 158979, 158984, 158993, 158994, 159108, 159109, 159110, 159112, 159117, 159136, 159138, 159139, 159145, 159155, 159966, 160096, 160097, 160098, 160099, 160117, 160118, 160119, 160120, 160122, 160123, 160157, 160158, 160159, 160160, 160163, 160252, 160256, 160258, 160259, 160260, 160269, 160270, 160272, 160273, 160433, 160434, 160435, 160436, 160460, 160461.

Vita

Irakli Garishvili was born on August 3, 1979 in Tbilisi, Georgia (a former soviet republic). In 1996, after graduating from A. Razmadze Physical and Matematical Gymnasium #7 of Tbilisi, he enrolled in the Department of Physics of Tbilisi State University (TSU). He graduated in 2000 with a B.Sc. degree. In the same year he enrolled in the master's program at the Department of Physics of TSU, which he completed in September 2002 with an M.S. degree.

In August 2003 he moved to Knoxville, TN and enrolled in the Ph.D. program at the Department of Physics and Astronomy at the University of Tennessee. With Dr. Kenneth Read as his advisor he performed doctoral research in the field of high-enegry nuclear physics with the PHENIX experiment at Brookhaven National Laboratory. On August 27, 2009 he succesfully defended his dissertation. After formally completing his Ph.D. in December 2009, he is expected to begin his post-doctoral work at Lawrence Livermore National Laboratory.

Irakli has been happily married since July 2006.